Optical Studies of Monolayers at the Air/Water Interface

A thesis presented

by

Aryeh Feder

to

the Department of Physics

in partial fulfillment of the requirements

for the degree of

Doctor of Philosophy

in the subject of

Physics

Harvard University

Cambridge, Massachusetts

May, 1997

Abstract

Monolayers of amphiphilic molecules at the air/water interface, Langmuir monolayers, provide an experimentally accessible system for the study of physics in two dimensions. As a function of temperature and density, Langmuir monolayers display a series of phases and phase transitions; this thesis describes several optical experiments which clarify the macroscopic properties of some of these monolayer phases.

In one experiment a combination of two techniques, laser light scattering and Brewster angle microscopy, is used to study the effect of inhomogeneous monolayers on the damping of capillary waves. It is shown that the monolayer contributes to the capillary wave damping when the size of a typical monolayer domain is equal to or larger than the capillary wavelength.

Secondly, a new technique to measure the tilt angle of molecules from the surface normal is described. The validity of the technique is demonstrated by comparison to previously performed x-ray scattering experiments. The tilt angle of a monolayer of long-chain alcohol molecules is measured as a function of temperature and pressure near first- and second-order phase transitions from tilted to untilted monolayer phases.

Finally, depolarized Brewster angle microscopy is used to study orientational fluctuations in a two-dimensional smectic-*C* liquid crystal. The results are in excellent agreement with theoretical predictions. In addition, the first measurements of orientational elasticity and viscosity in a liquid crystal system with variable density are presented.

Table of Contents

List of Figures

Chapter 2

Chapter 3

Chapter 4

Chapter 5

Chapter 6

Acknowledgments

I am grateful to Professor Eric Mazur for the opportunity to work in his group. Eric encouraged me to set the direction of my own research and to pursue the questions which I found most interesting, while providing guidance along the way. He also has involved me in many of the non-laboratory aspects of scientific research, including writing articles and grant proposals and preparing presentations. Eric's clarity of presentation, both written and oral, will always serve as a goal to which I will aspire. I know that the skills that I have learned from him will serve me well in my post-graduate school career. Most importantly, I thank Eric for creating an especially friendly lab atmosphere.

Eric's gift for choosing graduate students who integrate well into the group's culture has provided me with a great set of coworkers. On the "liquids" project I have benefited from collaboration with Ka Yee Lee, Qingyu Wang, Yuka Tabe and Glenn Wong. Ka Yee's enthusiasm in the few months that we overlapped would have been enough to propel me through my entire graduate school career (and then some) if I had only found a way to bottle it. Her visits to our lab are still anticipated and always uplifting. Qingyu taught me by example that a talented scientist can quickly learn about a new field and produce valuable contributions. I am especially grateful to Yuka Tabe; without her work, the liquid crystal experiments would never have been possible. Her dedication to her work is inspiring. Glenn reminded me of the importance of pursuing one's interests and of maintaining a healthy life outside of the lab.

I have benefitted at least as much from my interactions with my groupmates on other projects. When I joined the group, barely knowing a laser from a light bulb, I received a tremendous amount of help from the senior group members, Shrenik Deliwala, Jay Goldman, Yakir Siegal, and Walter Mieher, as well as from my more advanced contemporary, Eli Glezer. Shrenik provided me with some of the most stimulating conversations I've ever had, on a variety of topics which I couldn't begin to list. The breadth of his knowledge continues to amaze me, and his advice helped me through many difficult spots. Jay consistently responded to my questions with five original ideas that I wouldn't have come up with in a week of thinking. Yakir was always ready with helpful advice (and I should have listened when he told me to avoid Lucifer), even if he disapproved of my choice of condiments. Walter entertained us with stories of life at Cornell, which only heightened my appreciation for the atmosphere I've experienced at Harvard. Eli's friendship has been the source of many thought-provoking conversations. In addition, if it weren't for his unfailingly practical experimental advice, I would doubtlessly still be mired in my first project.

I've enjoyed my many opportunities to bond with Rich Finlay, whether cleaning up the aftermath of a Lucifer upgrade, or our more enjoyable diversions with networked computers. I only regret that we abandoned our experiments on the interaction of liquid nitrogen with flavored dairy products. I am grateful for Li Huang's friendship, as well as her generosity with her Girl Scout cookies. I have also benefited from my friendship Tsing-Hua Her, whose sunny disposition could always cheer up my day. Claudia Wu adds a touch of class to the group, and her

piano playing enlivens our group outings. I've enjoyed many geopolitical conversations with Paul Callan, and I try not to hold against him his predilection for the likes of TEX and unix. Chris Schaffer may set a record of quickest sprint out of the starting block. I am sure that Albert Kim and Nan Shen will enjoy many fun filled hours on the third floor of McKay in the years to come.

I would like to thank the members of my committee, Professors Peter Pershan and David Nelson, for their many helpful conversations over the course of my graduate school career. In particular, the semi-regular BAM meetings with Professor Pershan and his group always provided a useful sounding board for my experimental ideas. I have enjoyed fruitful interactions with the monolayer portion of the Pershan group, including Bill Foster, Marco Bommarito, Ming Shih, Masa Fukuto and Ralf Heilmann. I am especially grateful to Bill, Marco and Ming for teaching me about Langmuir monolayers. My squash games with another non-Mazur group member, Phillip Fisher, have provided a welcome diversion from my work in the lab.

I would especially like to thank my family for their support over the years. We have grown closer through difficult times, and their love and understanding has helped me make it to this point. My parents have always supported my scientific endeavors, even when they stopped understanding what I was talking about, or I stopped wanting to talk about it. I am lucky to have siblings who are also friends; their only failing is that they've abandoned their job of making sure that things don't go to my head. My sister-in-law Sarah is my biggest fan — I only hope that she someday regains her perspective about me. I owe a special debt of gratitude to

my brother-in-law Jimmy for not divulging my Marathon and ice cream related activities to my committee.

Last, but certainly not least, I want to thank my best friend, my wife Rachel. Despite the distraction which she provided during my first year of graduate school, I can't imagine having made it to this point without her. The love and support which she provided during the difficult portions of my graduate school career are the only reason that I was able to make it through this long process. I only wish that I could return to her one tenth of the favor which she has given me.

Acknowledgment of financial support

I gratefully acknowledge the support of a Department of Defense National Defense Science and Engineering Graduate Fellowship.

To my parents,

without whom I never would

have made it to graduate school,

and to Rachel,

who helped me through it.

Chapter 1

Introduction

Many amphiphilic organic molecules form Langmuir monolayers — films one molecule thick at the air/water interface. These monolayers can be used as an experimentally accessible realization of a two-dimensional system. We have studied the behavior of Langmuir monolayers using several optical experimental techniques. This thesis describes the results of these experiments.

Chapter 2 provides a general introduction to Langmuir monolayers. First, we review the motivations for studying Langmuir monolayers, including the primary motivation of this thesis, the study of physics in two-dimensional systems. The properties of two-dimensional systems are discussed, including their lack of true long-range order. An overview is given of the types of quasi-long-range order that can occur in these systems. Finally, the standard experimental technique used to study Langmuir monolayers — the measurement of surface pressure versus molecular area isotherms — is introduced, and the experimental setup for measuring these isotherms is described in detail.

The experimental optical techniques used for the experiments in this thesis are described in Chapter 3. First, the use of laser light scattering to study the propagation and damping of capillary waves at the air/water interface is explained, and the experimental setup used to perform the experiments described in Chapter 4 is described. Then we discuss the use of Brewster angle microscopy to study the

morphology of Langmuir monolayers in two ways. Using *p*-polarized incident and reflected light we can study the coexistence of monolayer phases with different density. With *s*-polarized reflected light, we can study quasi-long-range orientational order of the tilt direction in monolayers. These techniques are instrumental to the experiments described in Chapters 4, 5, and 6.

Chapter 4 describes the use of two complementary techniques, laser light scattering and Brewster angle microscopy, to study the damping of capillary waves due to heterogeneous monolayers at the air/water interface. Laser light scattering measurements show that the capillary wave damping constant starts to rise from its value for a pure air/water interface in the gas/liquid expanded region of the monolayer phase diagram, and reaches its maximum value at the end of this coexistence region. The density at which the damping begins to rise depends on the frequency of the capillary wave. Brewster angle microscopy shows that the rise in the damping constant begins when the monolayer domain size is comparable to the capillary wavelength.

Chapter 5 describes a new technique that we have developed to measure the tilt angle of monolayer molecules from the surface normal using Brewster angle microscopy. Studies of a long-chain fatty acid, which has been well characterized using x-ray scattering, demonstrate the validity of the technique. In addition, we examine the behavior of the molecular tilt near a phase transition from a tilted to an untilted monolayer phase. The results indicate that an “untilted” phase can retain a small molecular tilt.

Chapter 6 describes an experiment that studies orientational fluctuations in a two-dimensional smectic-*C* liquid crystal using depolarized Brewster angle microscopy. First, a theoretical prediction for the behavior of these fluctuations is derived. The experimental measurements show excellent agreement with the predicted functional form. In addition, we measure the dependence of the orientational elasticity and viscosity on temperature and density. The orientational viscosity depends strongly on these parameters, changing by more than an order of magnitude with a 2.5 percent change in temperature or a 20 percent change in density. The orientational viscosity, within the experimental error, is nearly independent of temperature and density.

Chapter 2

Langmuir Monolayers

2.1 Introduction

It has long been recognized that certain substances spread at the air/water interface to form Langmuir monolayers — films one molecule thick.[1, 2] Some substances naturally spread into Langmuir monolayers, others form a drop on the water surface, as shown in Fig. 2.1. The contact angle θ is determined by the three surface tensions $\gamma_{w,a}$, $\gamma_{l,w}$, and $\gamma_{l,w}$, and by the condition that point p must remain fixed (*i.e.*, the net horizontal force at point p must vanish). This condition is satisfied when $\gamma_{w,a} = \gamma_{l,w} + \gamma_{l,a} \cos(\theta)$. However, if $\gamma_{w,a} > \gamma_{l,w} + \gamma_{l,a}$, the condition cannot be satisfied for any value of θ and the liquid spreads to cover the entire air/water interface (*i.e.*, it completely wets the interface). If the volume of the drop is smaller than the surface area of the water multiplied by a molecular thickness, the resulting film is only one molecule thick. Molecules that form Langmuir monolayers are amphiphilic — they have a hydrophilic head (a polar group such as an acid or

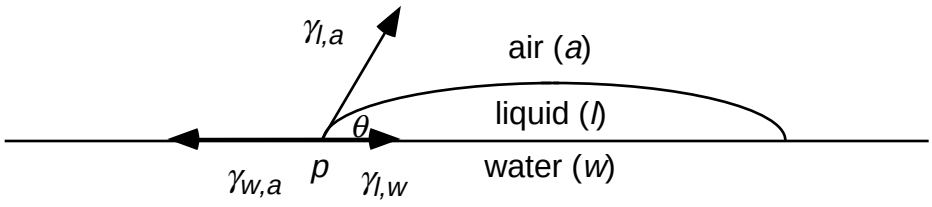

Figure 2.1. Diagram of a drop of a liquid on water. The contact angle θ is determined by the surface tensions of the three interfaces; the horizontal component of the sum of the three vectors must equal zero.

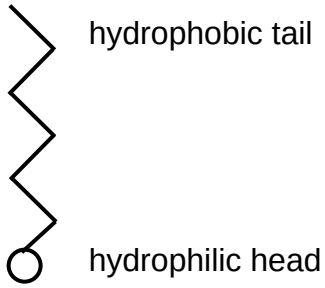

Figure 2.2. Schematic diagram of an amphiphilic molecule. The hydrophilic head contains a polar element such as an acid or alcohol group. The hydrophobic tail is often a hydrocarbon chain.

alcohol) and a long hydrophobic tail (often a hydrocarbon chain), shown schematically in Fig. 2.2. In order for the monolayer to be stable, the substance must have a low enough vapor pressure and solubility in water that it does not dissolve or evaporate.

The method mentioned above for preparing Langmuir monolayers is impractical in a laboratory setting; the volume of liquid necessary to form a monolayer on a 500 cm^2 surface is only approximately 10^{-4} cm^3, too small a volume to be conveniently handled. The most common method of preparing monolayers is to dissolve a small quantity of material in a volatile solvent such as chloroform, which completely wets water. When a drop of the solvent is placed on the water, it spreads over the surface of the water. As the solvent evaporates, it leaves behind the material distributed over the water surface. Using this technique, monolayers can be formed from many substances that do not spread into monolayers from their bulk phase. Classes of molecules that form Langmuir monolayers include long-chain fatty acids ($CH_3(CH_2)_{(n-2)}COOH$) and alcohols ($CH_3(CH_2)_{(n-2)}CH_2OH$).

2.2 Motivation

Recently, Langmuir monolayers have been the subject of a great deal of attention.[3, 4] This is partially due to their potential uses in a variety of industrial applications, as well as the insight that they offer into several biological problems. However, they are also of intrinsic physical interest as model two-dimensional systems. In this section we discuss some of the motivations for the study of Langmuir monolayers.

2.2.1 Biological applications

Most of the biological interest in monolayers is due to their similarity to the lipid bilayers which make up cell membranes.[5-7] A comparison between Langmuir monolayers and cell membranes is shown in Fig. 2.3. A cell membrane is made of a lipid bilayer with embedded proteins and forms a closed vesicle with water on the inside and on the outside. The bilayer can be treated as two weakly interacting

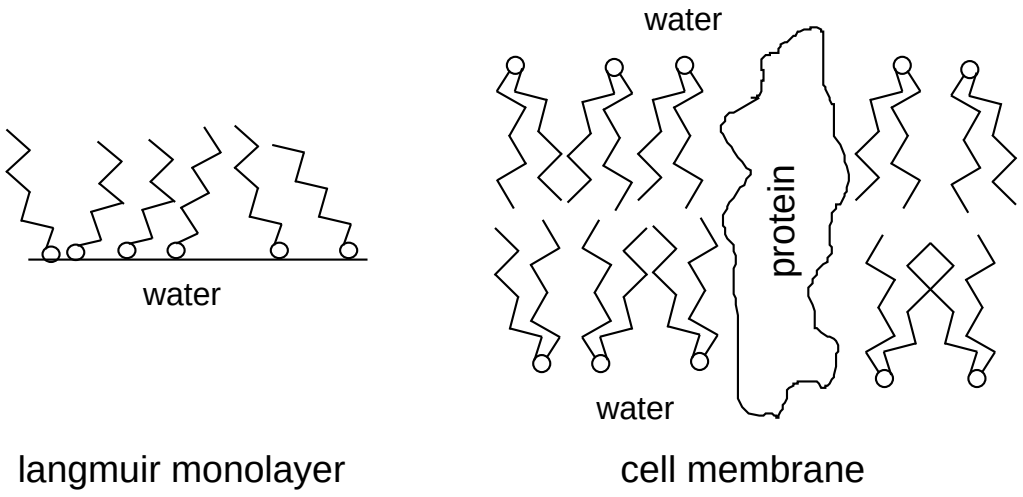

Figure 2.3. Comparison of a Langmuir monolayer to a cell membrane. The cell membrane can be treated as two weakly interacting monolayers.

monolayers. Research has shown that these lipid bilayers undergo many of the same phase transitions as Langmuir monolayers.

In addition to their use as models of cell membranes, some monolayer systems have direct biological relevance.[8, 9] Chief among these is pulmonary surfactant, a substance that reduces the surface tension in the lungs by a factor of almost 50. This reduction in surface tension eases the expansion and compression of the alveoli of the lung with each breath. Because premature infants often lack pulmonary surfactant, much research has gone into studying the properties of pulmonary surfactant, and trying to isolate its active components for therapeutic use.

2.2.2 Industrial applications

The technological interest in monolayers stems from the wide applications of organic thin films.[10] These applications include: thin film optics, sensors and transducers, protective layers, patternable materials such as photoresists, surface preparation and modification (wetting, adhesion), and chemically modified electrodes. Most of these applications involve multilayer (Langmuir-Blodgett) films, built up by successive deposition of Langmuir monolayers. Important parameters that affect the utility of these films are intermolecular ordering and defect structure. Knowledge of tilt ordering and defects in monolayers is therefore important for improving thin film technology.

2.3 Two-dimensional systems

Langmuir monolayers provide an ideal experimental system for the study of physics in two dimensions. As a function of density and temperature, monolayers undergo a variety of phase transitions.[3, 4, 11] In order to understand the nature of monolayer phases and phase transitions we first review the types of order that are possible in two-dimensional systems.

2.3.1 Lack of long range order

One of the most striking differences between two- and three-dimensional systems is that, while long-range order is common in three-dimensional crystals, fluctuations destroy long-range positional order in two-dimensional systems.[12] We demonstrate this following the method of Brock.[12]

Consider a two-dimensional crystal in which all of the molecules on the lattice occupy the vertices of a Bravais lattice, with lattice spacing a. At any finite temperature there are fluctuations of the molecules from these equilibrium positions. If the magnitude of these fluctuations become comparable to the lattice constant of the crystal, the long range order is destroyed. Let $\mathbf{u}(\mathbf{r})$ be the vector displacement of the molecule at position $\mathbf{r}$. A uniform change in $\mathbf{u}$, $\mathbf{u}(\mathbf{r})$ = constant, corresponds to a translation of the crystal, which does not change its free energy. Similarly, the free energy can not depend linearly on gradients in $\mathbf{u}$, because the Bravais lattice then would not represent the lowest energy configuration of the system. The lowest order terms in the change in free energy must be quadratic in gradients of $\mathbf{u}$, yielding to second order:

$$\delta F[\mathbf{u}(\mathbf{r})] = \frac{1}{2}\int \lambda_{ijkl}\frac{\partial u_i}{\partial x_j}\frac{\partial u_k}{\partial x_l}d^2r \tag{2.1}$$

where λ_{ijkl} is the elastic modulus tensor.

The long-range positional order is considered to be destroyed if the average magnitude of **u**(**r**) exceeds the lattice spacing *a*; we therefore want to calculate the thermal average of $|\mathbf{u}(\mathbf{r})|^2$. The thermal average of any quantity $\langle A\rangle$ is given by

$$\langle A\rangle = \frac{\sum_{\{\mathbf{u}(\mathbf{r})\}} A e^{-\delta F[\mathbf{u}]/k_B T}}{\sum_{\{\mathbf{u}(\mathbf{r})\}} e^{-\delta F[\mathbf{u}]/k_B T}} \tag{2.2}$$

where {**u**(**r**)} represents a sum over all possible displacements **u**(**r**).

The average of $|\mathbf{u}(\mathbf{r})|^2$ is most easily calculated using the Fourier transform of **u**,

$$\mathbf{u}(\mathbf{r}) = \sum_{\mathbf{q}} \mathbf{u}_{\mathbf{q}} e^{i(\mathbf{q}\cdot\mathbf{r})} \tag{2.3}$$

where the sum is taken over reciprocal lattice vectors **q**. Since **u**(**r**) is real, the coefficients $\mathbf{u}_{\mathbf{q}}$ are related by $\mathbf{u}_{-\mathbf{q}} = \mathbf{u}_{\mathbf{q}}^*$. If we substitute this into Eq. 2.1, all of the terms with $\mathbf{q}' \neq -\mathbf{q}$ disappear in the integration, and we are left with:

$$\delta F[\mathbf{u}(\mathbf{r})] = \frac{1}{2}\Omega\sum_{\mathbf{q}} \lambda_{ijkl} q_j q_l u_{i\mathbf{q}} u_{k\mathbf{q}}^* = \frac{1}{2}\Omega\sum_{\mathbf{q}} \beta_{ik}(\mathbf{q})\, u_{i\mathbf{q}} u_{k\mathbf{q}}^* \tag{2.4}$$

where Ω is the area of the system, and the elements of the tensor β_{ik} are real quadratic functions of **q**.

The probability distribution function (Eq. 2.2) is therefore gaussian in **q**, and the thermal average of the Fourier components of **u** are[13]

$$\langle u_{i\mathbf{q}} u_{k\mathbf{q}} \rangle = \frac{k_B T}{\Omega} \beta_{ik}^{-1}(\mathbf{q}) \tag{2.5}$$

where β_{ik}^{-1} are the elements of the inverse matrix of β_{ik}. To highlight that the elements of β_{ik}^{-1} are quadratic in q^{-1}, we rewrite β_{ik}^{-1} as $A_{ik}(\hat{\mathbf{n}})q^{-2}$, where the tensor A_{ik} depends only on $\hat{\mathbf{n}}$, a unit vector in the direction of **q**.

The mean-square displacement is given by summing Eq. 2.5 over all values of **q**. Switching from a sum to an integral we get

$$\langle |\mathbf{u}(\mathbf{r})|^2 \rangle = k_B T \int \frac{A_{ii}(\hat{\mathbf{n}})\, d^2 q}{(2\pi)^2 q^2} \propto \int_0^{1/a} \frac{1}{q} dq \tag{2.6}$$

The short wavelength (large q) cutoff of the integral is given by the reciprocal of the lattice spacing a. The long wavelength (small q) fluctuations cause the mean-square displacement to diverge if there is no small q cutoff (*i.e.*, for an infinite system). Because mean-square displacements larger than a^2 destroy the periodicity of the lattice, we see that no true long-range positional order can exist in an infinite two-dimensional system (assuming that the free energy is second-order in gradients of the displacements). For a finite system of size L, there is a small q cutoff at $1/L$, and the mean-square displacement is proportional to $\ln(L/a)$, (see Eq. 2.6). Because the mean-square displacement now diverges only logarithmically, we see that there can be long-range positional order in a two-dimensional system of finite size.

While true long-range positional order does not exist in infinite two-dimensional systems at finite temperatures, there are phases that exhibit quasi-long-range order. Whereas correlation lengths decay exponentially in systems with short-range order, they decay only algebraically (*i.e.*, as $r^{-\eta}$, where η is a system dependent constant) in systems with quasi-long-range order.[14] Two-dimensional systems with quasi-long-range positional order can have true long-range bond-orientational (hexatic) order, which is discussed below.[12]

2.3.2 Hexatic order

In three-dimensional systems, the transition from liquid to solid is always discontinuous, and there is no phase with positional order intermediate between that of a liquid and a solid. In two dimensions, however, there exists a type of order called bond-orientational order, or hexatic order.[15] The differences between a two-dimensional system with quasi-long-range positional order (2D solid), hexatic order, and liquid (isotropic) order is illustrated in Fig. 2.4. In each case the local order is hexagonal. The differences are apparent when we compare the local structure at point *B* to the structure represented by a hexagon at point *A* translated by an integral number of lattice spacings. In the 2D solid phase the molecules around point *B* are separated from the molecule at point *A* by an integral number of lattice vectors, provided we are within the range of the quasi-long-range order. In the hexatic phase, the molecules around point *B* are not separated from point *A* by an integral number of lattice spacings — *i.e.*, there is no long-range translational order. However, the hexagon defined by the molecules surrounding point *B* has the same orientation as the hexagon formed by the molecules surrounding point *A*.

This quasi-long-range bond-orientational order characterizes the hexatic phase. By contrast, in the liquid phase the molecules surrounding point *B* are not separated from point *A* by an integral number of lattice vectors, and their orientation is not the same as the orientation of the molecules around point *A*. The liquid phase is isotropic — both the translational and bond-orientational order are short range.

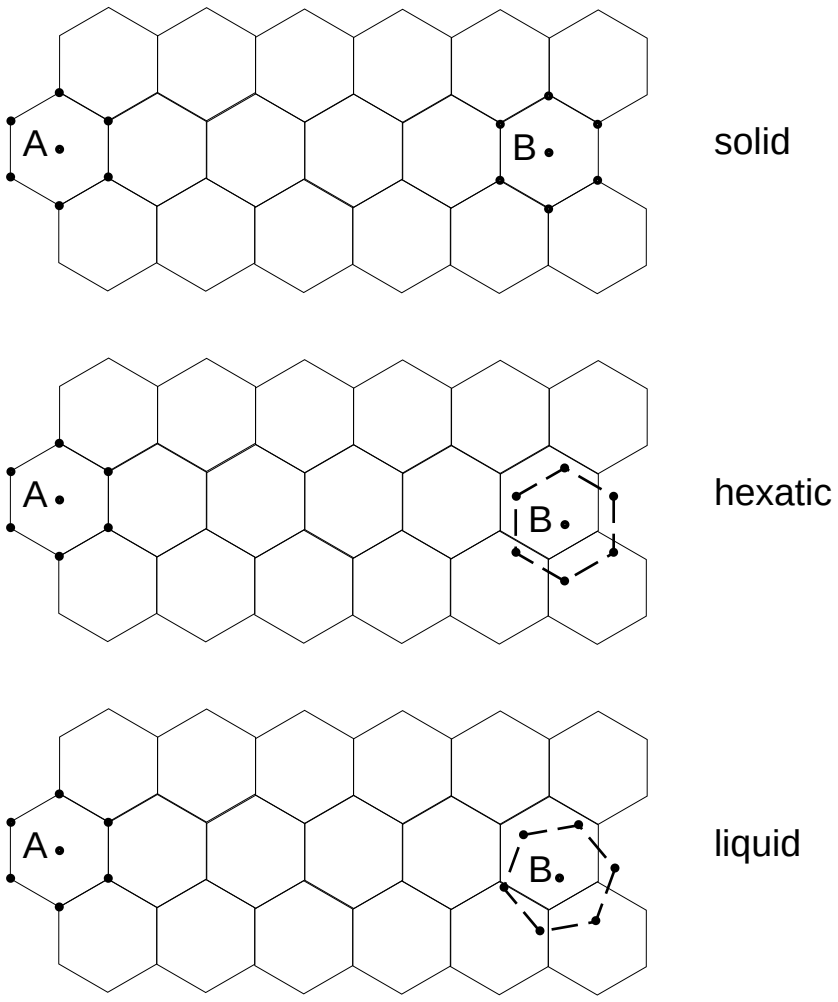

Figure 2.4. Comparison of solid, hexatic and liquid order in a two-dimensional system. The honeycomb lattice shows some of the points of a bravais lattice defined by the molecules around point *A*. The dashed hexagons are defined by the positions of the molecules surrounding point *B*.

The hexatic phase is characterized by the presence of free dislocations, which destroy long-range positional order while maintaining the bond-orientational order. A dislocation is created by adding an additional half row of molecules to an ideal lattice, as is illustrated in Fig. 2.5. The molecules labeled 7 and 5 have seven and five nearest neighbors, respectively; the half row of additional molecules are labeled x. Note that while the positional order is destroyed by the presence of a dislocation, the bond orientational order is not, as is indicated by the two hexagons on opposite sides of Fig. 2.5. Following the discussion of Brock,[16] we can explain the transition from solid to hexatic. In the solid phase, any dislocations exist as bound pairs, which do not affect the positional order far from the dislocations. The elastic strain energy associated with an unbound dislocation that occupies an area L^2 is $E = \pi k_B T K \ln(L/a)$, where K is a temperature dependent elastic constant and a is the lattice spacing. There are approximately L/a places to put the dislocation, yielding an entropy gain of $S \approx 2\ k_B \ln(L/a)$ when the dislocation unbinds.

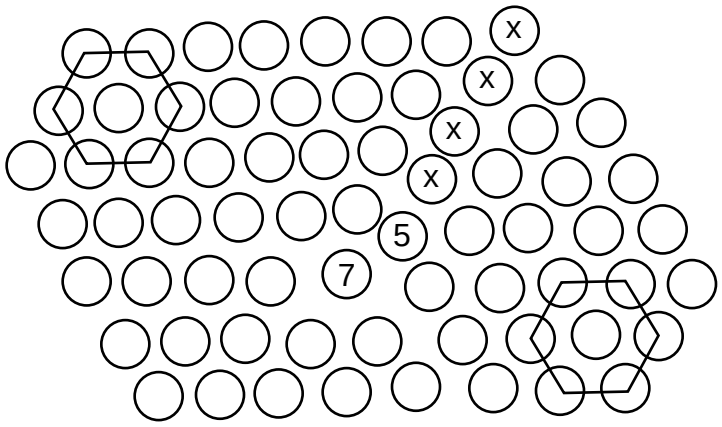

Figure 2.5. Dislocation in a hexagonal lattice. The dislocation is caused by the addition of an additional half row of molecules, labeled x. The molecules labeled 7 and 5 have seven and five nearest neighbors, respectively. That the dislocation does not destroy bond-orientational order, can be seen by the orientations of the two hexagons.

Therefore a phase transition occurs when the free energy for unbound dislocations $F = E - TS \approx k_B T \ln(L/a)\ (\pi K - 2)$ changes sign — *i.e.*, when $K \approx 2/\pi$.

In a similar fashion, the transition from hexatic to an isotropic liquid is caused by the unbinding of disclinations. A disclination is a point in the lattice with either five of seven nearest neighbors. A five-fold disclination is illustrated in Fig. 2.6. Comparison of local hexagons shows the destruction of the quasi-long-range bond-orientational order. Note that the dislocation in Fig. 2.5 is a bound pair of disclinations — one fivefold and one sevenfold. Just as for the solid/hexatic transition, an hexatic/isotropic transition occurs when the entropy for an unbound disclination becomes greater than the energy cost of that disclination.

2.3.3 Types of order in Langmuir monolayers

The molecules that make up Langmuir monolayers are often rodlike, with a long hydrophobic tail. At low surface densities the tails tend to lie flat on the water

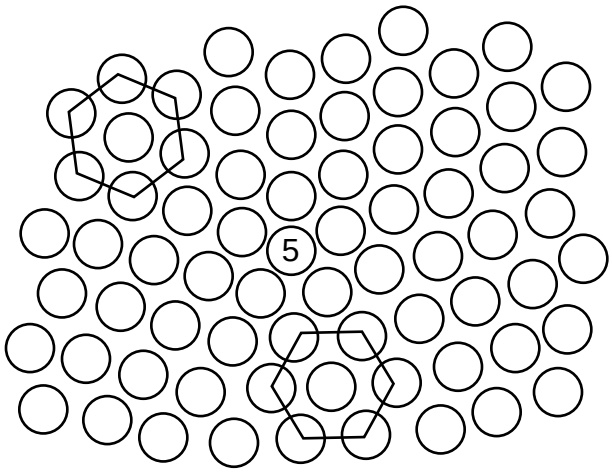

Figure 2.6. A fivefold disclination in a two-dimensional lattice. The molecule labeled 5 has five nearest neighbors. The hexagons defined by the positions of the molecules around two points have different orientations, illustrating the loss of bond-orientational order.

surface. However, as the density of the molecules is increased, the attractive interactions between the chains causes them to stand up at some angle from the surface. The orientation of each molecule can be defined by two angles, φ and θ, which define the angle with the surface normal and with an arbitrarily defined x-axis, respectively. If $\langle\varphi\rangle \neq 0$, then there are various types of orientational order that the monolayer can display. There can be short-range or quasi long-range orientational order, which correspond to exponential or algebraic decays in correlations in θ, $\langle\theta(\mathbf{r})\,\theta(0)\rangle - \langle\theta(\mathbf{r})\rangle\langle\theta(0)\rangle$, respectively. For quasi-long-range orientational order, different phases can be distinguished by their tilt direction; toward nearest neighbor, toward next nearest neighbor, or intermediate between the two, as is illustrated in Fig. 2.7. If $\langle\varphi\rangle = 0$ the phase is said to be untilted.

Monolayer phases are distinguished by their positional/bond-orientational order (2D solid, hexatic, liquid) and their orientational order. Each monolayer phase can be described by its type of order and the tilt angle φ of the molecules. Most combinations of these types of order (*e.g.* 2D solid with quasi-long-range orientational order, tilted toward nearest neighbor) are possible, though some are

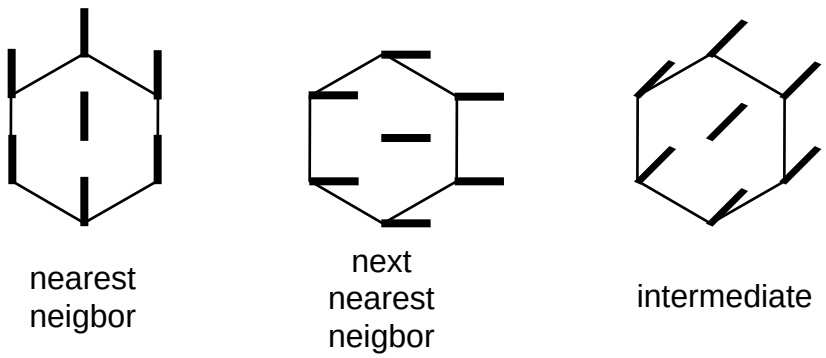

Figure 2.7. Top view of different types of tilt order in two-dimensional systems.

forbidden; for example, any phase with quasi-long range orientational order must also have quasi-long-range bond-orientational order (*i.e.*, it must be solid or hexatic).[17]

Unfortunately, different researchers use different naming conventions for the various monolayer phases. Whenever the microscopic structure of the monolayer is known, we will use the name of the bulk smectic phases whose order corresponds to the order in the monolayer phase. The types of order in several smectic phases are given in Table 2.1. The phase with short-range positional, bond-orientational and orientational order will be referred to as the liquid or liquid-expanded phase. However, for substances for which the microscopic structure is not known, an appropriate "local" naming convention will be used. For example, monolayers of pentadecanoic acid have a low density liquid phase (the liquid expanded phase) and a higher density phase which lacks long-range positional order, but whose microscopic orientational order is not known.[18] In keeping with the convention in the literature, we will refer to this phase as the liquid condensed phase.

Smectic Phase	Positional/Bond orientational order	Tilt Order
smectic-*A*	liquid	untilted
smectic-*I*	hexatic	NN
smectic-*F*	hexatic	NNN
smectic-*L*	hexatic	intermediate
hexatic-*B*	hexatic	untilted
crystalline-*B*	solid	untilted

Table 2.1. Types of order in selected smectic phases. NN — tilted toward its nearest neighbor. NNN — tilted toward its next-nearest neighbor.

2.4 Mechanical experimental techniques

In this section we will discuss some of the basic experimental techniques that are used to characterize Langmuir monolayers and the experimental setups used for the experiments in this thesis.

2.4.1 Surface pressure

An interface between two substances has an energy per unit area, γ, which is also called the surface tension, σ. Because the molecules of each substance usually have a stronger attraction to each other than they do to molecules of the other substance, this energy per unit area is generally positive. In these cases it is energetically favorable for a molecule of substance *A* to be in the bulk of substance *A*, rather than at the interface — *i.e.*, there is an excess energy associated with the interface. In order to minimize its energy, the system will try to minimize its surface area (subject to other constraints, such as gravitational energy). Therefore, surface tension manifests itself as a force per unit length. If the surface tension between two fluids is negative it is energetically favorable to maximize the surface area between the two fluids. In that circumstance the interface will develop progressively finer folds until the two fluids are completely mixed — *i.e.*, negative surface tension implies that the two fluids are miscible.

Due to the strong hydrogen bonding between water molecules, water has a very high surface tension of about 72 mN/m at room temperature. When a Langmuir monolayer is spread at the air/water interface, the interaction of the water molecules with the hydrophilic head groups lowers the energy cost for a water

molecule to be at the surface — *i.e.*, it lowers the surface tension. In addition, if the monolayer molecules are closely packed with one another, the steric interactions between the molecules (*i.e.*, the fact that you cannot put two molecules in the same place at the same time) produces a force that opposes the tendency of the water surface to contract, thereby further lowering the surface tension σ. This change in the surface tension defines the surface pressure π:

$$\pi = \sigma_0 - \sigma \tag{2.7}$$

where σ_0 is the surface tension of a bare air/water interface.

There are a variety of methods for measuring surface pressure. In all of the experiments described in this thesis the surface pressure was measured with a Wilhelmy plate,[19] shown in Fig. 2.8. If the contact angle of the water with the plate is θ, then the force exerted on the plate by the water is $F = \sigma L \cos(\theta)$, where L is the perimeter of the cross section of the plate. The Wilhelmy plates used for all of the experiments in this thesis were made of filter paper, for which the contact angle

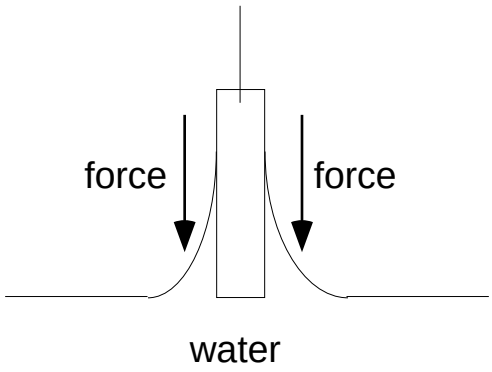

Figure 2.8. Schematic diagram of a filter paper Wilhelmy plate. The water makes contact with the paper with contact angle = 0. The water exerts a force on the plate equal to σL, where σ is the surface tension and L is the length of the contact line of the water with paper.

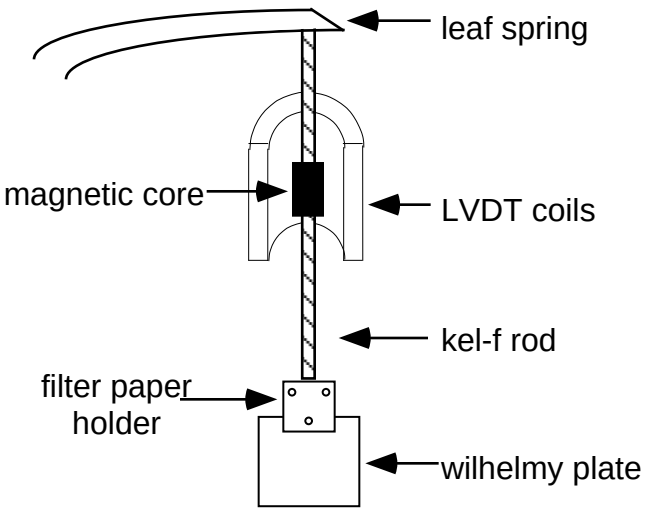

Figure 2.9. Surface pressure measurement apparatus. The force exerted on the Wilhelmy plate causes a linear displacement of the magnetic core. This displacement is measured with a linear variable differential transformer (LVDT).

is zero, leaving $F = \sigma L$. The Wilhelmy plate is suspended from a teflon-coated leaf spring. The force on the plate causes a displacement which is linear in the applied force, and which is measured by the movement of a magnetic core in a linear variable differential transformer (LVDT), as shown in Fig. 2.9.

2.4.2 Langmuir trough

The monolayer sample and water subphase are held in a chemically inert Langmuir trough; the density of the monolayer is controlled with a moveable barrier, which blocks off the surface of the water while allowing the bulk water to pass underneath it. Moving the barrier therefore causes any monolayer at the surface to be expanded or compressed, without causing the height of the water subphase to change.

The experiments described in this thesis were performed on two Langmuir troughs of slightly different construction. One trough, which will be referred to as

the light-scattering trough, was used for the laser-light-scattering and the orientational correlation measurements. The second trough, which will be referred to as the BAM trough, was used for Brewster angle microscopy.[20, 21] In each trough all of the components which are in contact with the water are made of chemically inert substances such as teflon and delrin.

A cross-sectional diagram of the light-scattering trough is shown in Fig. 2.10. The trough is milled from a single piece of stainless steel. The recess which holds the water has dimensions 30.48 cm × 7.62 cm × 0.48 cm. The trough is coated with black teflon to keep metal ions from leaching into the pure water subphase. Black teflon in used to minimize the scatter of light from the bottom of the trough. The trough is machined with water passages to enable effective temperature control. The temperature of the trough can be varied from approximately 10 °C to 45 °C,

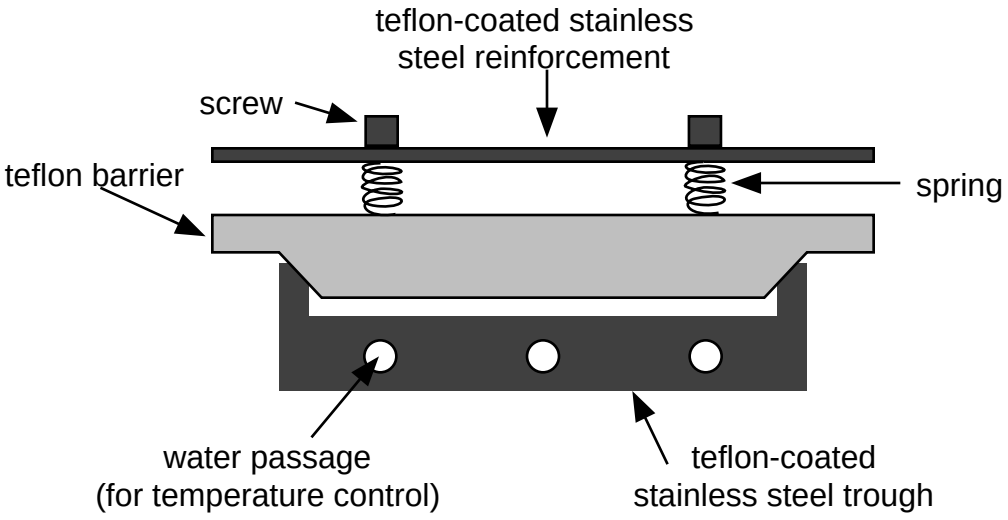

Figure 2.10. Cross section of the light scattering trough. The barrier and trough are cut at a 45° angle to improve the seal between them. Because they are made from materials with different coefficients of thermal expansion, the seal degrades at high temperature.

with a stability of 0.1 °C. The temperature is measured with a thermistor that is screwed into the trough.

The steel trough and the teflon barrier are each cut at a 45° angle. A piece of stainless steel is used to reinforce the barrier to keep it from warping. The screws attach the barrier to the steel reinforcement in such a way that the springs exert a downward force on the barrier, which helps maintain the seal between barrier and trough. However, because the coefficients of thermal expansion are different for teflon and steel, the seal tends to degrade as the temperature is raised.

The entire trough is contained inside an anodized aluminum enclosure to allow temperature control and to avoid sample contamination. The enclosure can be sealed and filled with an atmosphere of pure nitrogen. This is particularly important when studying monolayers at low density, where the monolayer does not completely cover the water surface; impurities in the environment can then attach to the bare water surface and contaminate the monolayer. The temperature of the enclosure is controlled with a separate water circulator from the one that regulates the temperature of the trough. An approximately +3 °C temperature difference is maintained between the trough and the enclosure to minimize the condensation of water on the inner walls of the enclosure. The enclosure has several windows to allow the input and output of optical beams — these windows are wrapped with heating tape to prevent condensation of water.

A cross-sectional diagram of the BAM trough is shown in Fig. 2.11. The trough itself is made of black teflon to minimize the leaching of impurities into the water subphase. The trough is attached to a copper mounting plate with stainless

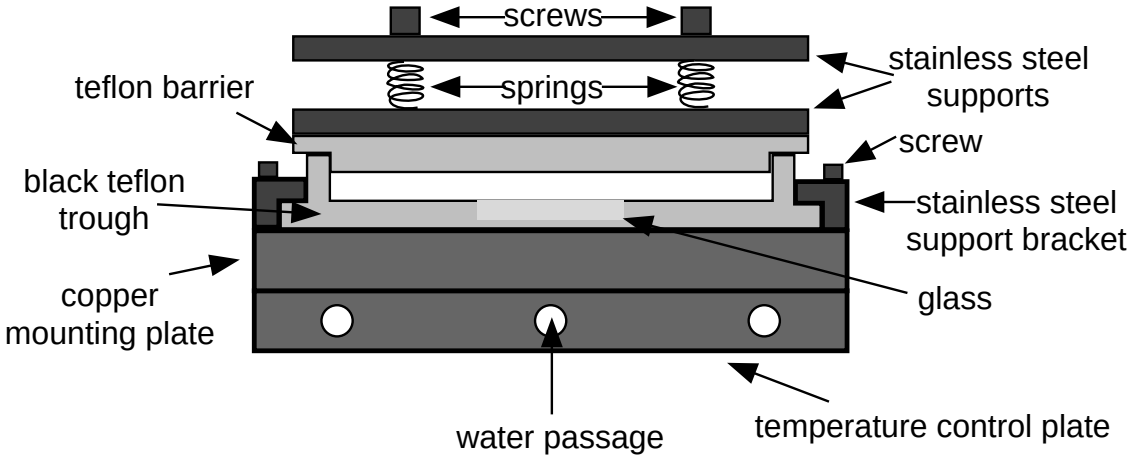

Figure 2.11. Cross section of the BAM trough. The stainless steel supports ensure that the teflon trough keeps the correct shape when it is mounted.

steel support brackets to ensure that when mounted the trough maintains its shape. The mounting plate, in turn, is attached to a temperature control plate. The barrier is made of teflon, and stainless steel supports are used to ensure that it maintains its shape. As in the light scattering trough, a pair of springs is used to press the barrier and the trough together, increasing the quality of the seal. Because both the trough and the barrier are made of teflon, the quality of the seal between them remains good at temperatures as high as 40 °C.

When laser light is used to study the monolayer at the interface, the light is absorbed at the bottom of the trough, causing local heating. In the case of the light scattering trough, that heat is quickly carried away by the stainless steel trough. Because teflon is a poor conductor of heat, however, in the BAM trough the local heating significantly affects the local temperature of the water. To alleviate this problem, a well is made where the laser hits the bottom of trough, and a glass window is inserted into the well. This helps in two ways. The thinner layer of teflon where the light is absorbed leads to more rapid heat transfer to the temperature

control plate. In addition, the glass serves to insulate the spot where the light is absorbed, reducing the heat transfer to the water.

The BAM trough is contained in a double enclosure for enhanced temperature control. The temperature of the temperature control plate is controlled with the water from one water circulator, while the inner and outer enclosures are controlled with water from a second circulator. The enclosures are kept at a temperature approximately 5 °C above the temperature of the temperature control plate. Because teflon is a poor conductor of heat, the water temperature is intermediate between the temperature of the temperature control plate and the enclosure. The temperature of the water is measured with a teflon coated thermistor inserted directly into the water. The temperature of the BAM trough can be varied from 2 to 40 °C with a stability of 0.2 °C.

2.4.3 Surface pressure/area isotherms

As a function of temperature and surface pressure, monolayers undergo phase transitions that are similar to the transitions in three-dimensional systems. Measuring the surface pressure as a function of area per molecule at constant temperature using a Langmuir trough and Wilhelmy plate as described above yields an isotherm equivalent to a pressure/volume isotherm. Such isotherms can be used to elucidate the phase behavior of the monolayer.[11, 22] For example, plateaus in the isotherm indicate first-order phase transitions, while kinks in the isotherm represent second-order phase transitions.

The difference between a first- and a second-order transition between two monolayer phases is as follows; in a first-order phase transition the densities of the

two phases at the pressure that the transition takes place, π_t, are different from one another. When the density of the system is intermediate between the densities of the two phases, the system displays phase coexistence. In a second-order phase transition, the transition between the two phases is continuous; at π_t the densities of the two phases are the same.

For example, Fig. 2.12 illustrates the difference between a first- and a second- order phase transition between a low-density tilted monolayer phase and a higher density untilted phase. In both cases the monolayer is in a uniform tilted phase when it is at low density. In the case of a first-order phase transition, when the average density of the monolayer is intermediate between the maximum density of the tilted phase and the minimum density of the untilted phase, the monolayer is no longer uniform. Rather, the monolayer nucleates domains of the higher-density untilted phase and displays phase coexistence between the tilted and untilted phases. As the monolayer is compressed further, the fraction of the monolayer in the untilted phase increases, while the fraction in the tilted phase decreases. During this period there is no increase in surface pressure — the isotherm displays a plateau. Finally, when the average density of the monolayer equals the density of the untilted phase, the phase transition is complete, and the entire monolayer is in the high-density, untilted phase. Further compression yields an increase in surface pressure.

In contrast to first-order transitions, second-order transitions never exhibit a coexistence between two phases. Instead, as the density of the system is increased, the tilt angle of the molecules becomes increasingly smaller, going smoothly to

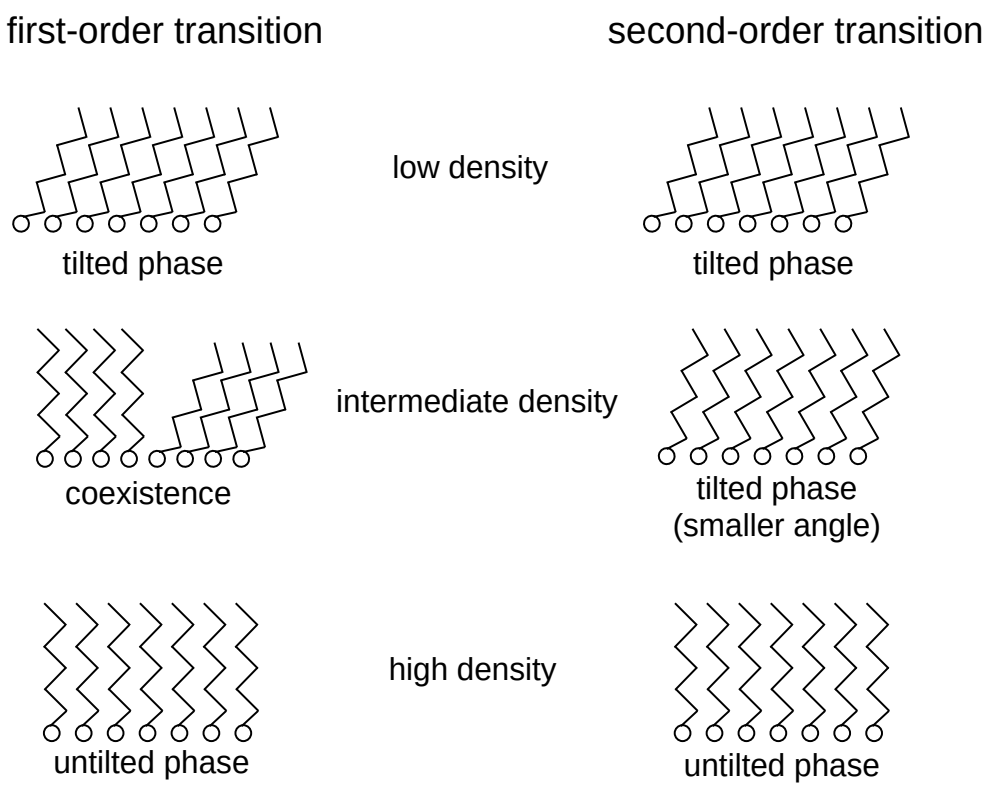

Figure 2.12. Comparison of first- and second-order phase transitions between a low-density tilted phase and a higher-density untilted phase. For the first-order transition there is a region where the two phases coexist. For the second-order transition the tilted phase changes continuously into the untilted phase.

zero. The isotherm displays a kink at the density at which the tilt angle becomes zero, indicating a second order transition.

2.4.4 Limitations of surface pressure/area isotherms

Surface pressure/area isotherms are helpful for characterizing phases and phase transitions in Langmuir monolayers. However, isotherm studies are often ambiguous, and lead to the creation of controversy that can only be resolved with more sophisticated techniques. For example, Fig. 2.13 shows an isotherm we measured for pentadecanoic acid, PDA ($C_{15}H_{30}O_2$). At very large area/molecule (not shown in this plot), PDA is in a two-dimensional gas phase, with the

molecules are far apart from one another and essentially non-interacting. The surface pressure in the gas phase is too small to be measured with our Wilhelmy plate, but other groups have measured the isotherm in this regime using more sensitive techniques. In the gas phase, the pressure increases with decreasing area. When the surface pressure reaches approximately 0.1 mN/m at an area per molecule of around 10 nm^2 there is a plateau, indicating a first-order transition from the gas phase to the liquid expanded (LE) phase. This phase transition continues until the area/molecule reaches approximately 0.45 nm^2, at which point the monolayer is in the pure LE phase. As the area is reduced within the LE phase the pressure rises, until the monolayer undergoes another phase transition, to the liquid condensed (LC) phase, at approximately 0.35 nm^2/molecule.

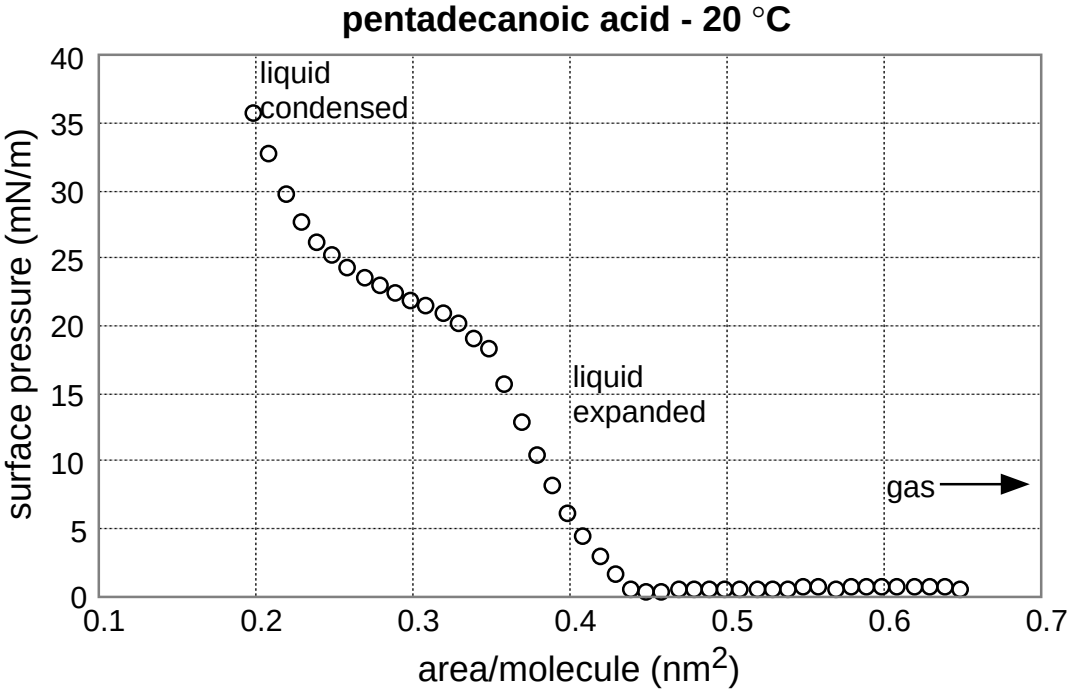

Figure 2.13. Surface pressure vs. area/molecule isotherm for pentadecanoic acid. At large area/molecule the monolayer undergoes a first order transition from the gas phase to the liquid expanded phase. At approximately 0.34 nm^2/molecule there is another phase transition, to the liquid condensed phase.

The nature of the LE/LC phase transition was a matter of dispute for several years.[3] In Fig. 2.13 there is only a kink in the isotherm, not a plateau, which seems to indicate a second-order, rather than a first-order, transition. Some researchers argued, however, that the transition is first-order, and that, if one was careful to exclude impurities, the isotherm would show the required plateau. Isotherm measurements alone were not sufficient to resolve this question; microscopy studies, however, clearly show phase coexistence in this region, indicating that the transition is first-order.

Similarly, several groups performed careful isotherms measurements of PDA around the gas/LE transition to see if this transition ended in a critical point at higher temperature. In an early study, Harkins and Boyd[11] measured isotherms of PDA at temperatures up to 35.2 °C. While the width of the plateau in the isotherm decreases with increasing temperature, they observed a plateau even at 35.2 °C, and therefore concluded that the critical temperature was higher, T_C > 35.2 °C. Later studies by Hawkins and Benedek[23] and by Kim and Cannell,[24] however, concluded that the gas/LE phase transition ends in a critical point, and they determined the critical temperature to be 26.9 ± 0.2 °C and 26.27 °C, respectively. Pallas and Pethica,[25] on the other hand, report the existence of a plateau at still higher temperatures, and therefore conclude that T_C > 40 °C. What is most striking about the groups' conflicting conclusions is that their raw data appears consistent with one another — the disagreements result from interpretation of the data.

These examples highlight the need for more sophisticated experimental methods to study Langmuir monolayers. Over the past twenty years a number of

techniques have been developed that shed light on various aspects of monolayer behavior. These include x-ray scattering,[26-28] which yields information about microscopic structure of monolayers, fluorescence[4, 29] and Brewster angle[20, 21] microscopy, which are used to study the macroscopic morphology of monolayers and their long-range orientational order, light scattering,[18, 30-32] which measures their viscoelastic properties, and non-linear optical techniques,[33, 34] which measure the molecular tilt and conformation. In the remainder of this thesis we discuss several linear optical techniques, and describe several experiments that help elucidate the behavior of two-dimensional systems.

References

1 I. Langmuir, J. Am. Chem. Soc. **39**, 1848 (1917).

2 L. Rayleigh, Proc. Roy. Soc. (London) **47**, 364 (1890).

3 C. M. Knobler, Adv. Chem. Phys. **72**, 397 (1990).

4 H. M. McConnell, Annu. Rev. Phys. Chem. **42**, 171 (1991).

5 S. W. Hui and Y. Hao, Biophys. J. **64**, 150 (1993).

6 R. Grimard, P. Tancrède, and C. Gicquaud, Biochemical and Biophysical Research Communications **190**, 1017 (1993).

7 J. P. Slotte, A. Östman, E. Kumar, *et al.*, Biochem. **32**, 7886 (1993).

8 K. Nag and K. M. W. Keough, Biophys. J. **1019**, 1019 (1993).

9 F. R. Rana, A. J. Mautone, and R. A. Dluhy, Biochem. **32**, 3169 (1993).

10 J. D. Swalen, D. L. Allara, J. D. Andrade, *et al.*, Langmuir **3**, 932 (1986).

11 W. D. Harkins and E. Boyd, J. Phys. Chem. **45**, 20 (1941).

12 J. D. Brock, in *Bond-Orientational Order in Condensed Matter Systems*, edited by K. J. Strandburg (Springer-Verlag, New York, 1992), p. 1.

13 L. D. Landau and E. M. Lifshitz, *Statistical Physics* (Pergamon Press, Oxford, 1980).

14 C. C. Huang, in *Bond-Orientational Order in Condensed Matter Systems*, edited by K. J. Strandburg (Springer-Verlag, New York, 1992), p. 78.

15 B. I. Halperin and D. R. Nelson, Phys. Rev. Lett. **41**, 121 (1978).

16 J. D. Brock, A. Aharony, R. J. Birgeneau, *et al.*, Phys. Rev. Lett. **57**, 98 (1986).

17 D. R. Nelson and B. I. Halperin, Phys. Rev. B **21**, 5312 (1980).

18 K. Y. Lee, T. Chou, D. S. Chung, *et al.*, J. Phys. Chem. **97**, 12876 (1993).

[19] G. L. Gaines, J. Coll. Int. Sci. **62**, 191 (1977).

[20] S. Henon and J. Meunier, Rev. Sci. Instrum. **62**, 936 (1991).

[21] D. Honig and D. Mobius, J. Phys. Chem. **95**, 4590 (1991).

[22] G. L. Gaines Jr., *Insoluble monolayers at liquid-gas interfaces* (John Wiley & Sons, Inc., 1966).

[23] G. A. Hawkins and G. B. Benedek, Phys. Rev. Lett. **32**, 524 (1974).

[24] M. W. Kim and D. Cannell, Phys. Rev. A **13**, 411 (1976).

[25] N. R. Pallas and B. A. Pethica, J. Chem. Soc., Fara. Trans. 1 **83**, 585 (1987).

[26] P. Dutta, J. B. Peng, B. Lin, *et al.*, Phys. Rev. Lett. **58**, 2228 (1987).

[27] K. Kjaer, J. Als-Nielsen, C. A. Helm, *et al.*, J. Phys. Chem. **93**, 3200 (1989).

[28] D. K. Schwartz, M. L. Schlossman, and P. S. Pershan, J. Chem. Phys. **96**, 2356 (1992).

[29] C. M. Knobler, Science **249**, 870 (1990).

[30] S. Hård and R. D. Neuman, J. Coll. Inter. Sci. **83**, 315 (1981).

[31] J. C. Earnshaw, R. C. McGivern, and P. J. Winch, J. Phys. France **49**, 1271 (1988).

[32] D. Langevin, J. Coll. Inter. Sci. **80**, 412 (1981).

[33] A. Castro, E. V. Sitzmann, D. Zhang, *et al.*, J. Phys. Chem. **95**, 6752 (1991).

[34] T. Rasing, Y. R. Shen, M. W. Kim, *et al.*, Phys. Rev. Lett. **55**, 2903 (1985).

Chapter 3

Optical Techniques

In Chapter 2 we discussed some of the general properties of Langmuir monolayers. This chapter describes two optical techniques, surface light scattering and Brewster angle microscopy, that are used to study the behavior of monolayers at the air/water interface. Surface light scattering yields information about the propagation and damping of surface waves, while Brewster angle microscopy is used to study the macroscopic morphology and molecular tilt of Langmuir monolayers.

3.1 Surface light scattering

Laser light scattering provides a powerful tool for studying dynamics at liquid interfaces. Light scattered by waves at an interface is shifted in wavevector and frequency relative to the incident light. Measuring these shifts yields information about the propagation and damping of the surface waves.

In this section we will discuss the details of using surface light scattering to study the behavior of capillary waves (waves whose restoring force comes from surface tension) at the air/water interface.

3.1.1 Theoretical framework

When light of frequency ω_L and wavevector $\mathbf{k}$ is incident on a perfectly smooth interface between two media, it splits into a refracted beam, which is

transmitted through the second medium, and a specularly reflected beam with frequency ω and wavevector $\mathbf{k}'$ which satisfies

$$k_x' = k_x,\ k_y' = k_y,\ k_z' = -k_z \tag{3.1}$$

where we have chosen the $\hat{\mathbf{z}}$-direction to be normal to the interface. Note that momentum is conserved in the plane of the interface, but not normal to the plane of the interface. The presence of the interface breaks the symmetry of the system along the $\hat{\mathbf{z}}$ axis; we therefore do not require that the momentum *of the light* be conserved in the $\hat{\mathbf{z}}$ direction. The total momentum is, of course, conserved — the excess momentum is transferred to the bulk of the second medium.

If the interface has a static "corrugation", *i.e.*, if there is a periodic change in the optical properties of the surface with wavevector $\mathbf{q}$ (where $\mathbf{q}$ lies in the *xy*-plane), then, in addition to the specularly reflected light, there is scattered light with frequency $\omega^s = \omega_L$ and wavevector $\mathbf{k}^s$, where

$$k_x^s = k_x \pm q_x,\ k_y^s = k_y \pm q_y. \tag{3.2}$$

and

$$k_z^s = \sqrt{|\mathbf{k}|^2 - (k_x^{s\,2} + k_y^{s\,2})} \tag{3.3}$$

Note that k_z^s is not equal to $-k_z$. Rather, k_z^s is determined by a combination of conservation of momentum in the plane of the interface (*i.e.*, Eq. 3.2) and energy conservation, which requires that $|\mathbf{k}^s| = |\mathbf{k}|$ since $\omega_L = c|\mathbf{k}| = \omega^s = c|\mathbf{k}^s|$, where c is the speed of light.

If the corrugation oscillates in time, (*e.g.*, there is a surface fluctuation), with angular frequency ω_c, then the scattered light will be shifted in frequency,

$$\omega_s = \omega_L \pm \omega_c , \tag{3.4}$$

where the + sign corresponds to the light absorbing a surface phonon, and the – sign corresponds to the emission of a phonon. The *x* and *y* components of $\mathbf{k}^s$ obey Eq. 3.2, and the *z*-component of $\mathbf{k}^s$ is determined by the condition $|\mathbf{k}^s| = \omega_s / c$. The fluctuations studied in this thesis fulfill the condition $\omega_c \ll \omega_L$, and therefore $|\mathbf{k}^s| \approx |\mathbf{k}|$. The scattering angle, θ_s, can be found from the dot product of $\mathbf{k}$ and $\mathbf{k}^s$:

$$\mathbf{k} \cdot \mathbf{k}^s \approx k^2 \cos(\theta_s) = k_x (k_x + q_x) + k_z \left(\sqrt{k_z^2 - [2k_x q_x + q_x^2 + q_y^2]} \right) \tag{3.5}$$

To lowest order in θ_s and q/k this yields

$$\theta_s \approx \frac{q_x}{k \cos(\theta_0)} + \frac{q_y}{k} \tag{3.6}$$

where θ_0 is the incident angle of the laser. If $q_y = 0$ the scattered light will lie in the plane of incidence of the unscattered light; otherwise $\mathbf{k}^s$ has a component perpendicular to the plane of incidence equal to q_y. If there are surface fluctuations at all wavevectors, only fluctuations with a specific wavevector (given by Eq. 3.6) scatters light in any given direction, and so measuring the light scattered at a specific angle determines the wavevector of the fluctuation studied.

3.1.2 Capillary waves

Chapter 4 discusses experiments that use laser light scattering to measure the damping of capillary waves at the air/water interface. The surface of a pure

liquid/vapor interface is never perfectly flat — thermal fluctuations give rise to small amplitude waves with all wavevectors.[1] These waves propagate in space and time according to the relation

$$h(\mathbf{r}, t) = h(\mathbf{r}, 0)\, e^{i(\mathbf{q}\cdot\mathbf{r} - \omega t)} \tag{3.7}$$

where h is the height of the interface, ω is the angular frequency of the waves, and q is their wavevector. These waves obey the dispersion relation[2]

$$\omega^2 = gq + \frac{\sigma}{\rho} q^3 \tag{3.8}$$

where g is the acceleration due to gravity, σ is the surface tension of the interface, and ρ is the density of the liquid. For waves with $\frac{\sigma q^2}{\rho g} \gg 1$, the first term in Eq. 3.8 is negligible relative to the second term; these waves, whose restoring force comes from surface tension, are called capillary waves, and their dispersion relation is given by

$$\omega_c^2 = \frac{\sigma}{\rho} q^3 \tag{3.9}$$

For the (theoretical) case of an undamped capillary wave, both $\mathbf{q}$ and ω_c are real, and the frequency spectrum of a capillary wave with wavevector $\mathbf{q}$ consists of delta function peaks at $\pm\omega_c$ — *i.e.*, light scattered by this wave would have its frequency shifted by exactly ω_c (see Fig. 3.1). In any real system, however, individual waves damp out with time. A wave with wavevector $\mathbf{q}$ will propogate as:

$$h(\mathbf{r}, t) = h(\mathbf{r}, 0)\, e^{i(\mathbf{q}\cdot\mathbf{r} - \omega t)}\, e^{-\Gamma t} \tag{3.10}$$

(though the surface will not become smoother with time, because thermal fluctuations continue to excite more waves). In this case the frequency of the capillary waves has a real and an imaginary part:

$$\omega = \omega_c + i\Gamma \tag{3.11}$$

where the real part of the frequency is given by Eq. 3.9, and the constant Γ describes the damping of the wave in time. The frequency spectrum of this wave is a Lorentzian with center frequency ω_c and full width at half maximum of 2Γ. The spectrum of the scattered light therefore shows Lorentzian peaks with full width at half maximum of 2Γ centered at ω_c (see Fig. 3.1).

The capillary wave frequency (of order 10^3 s^{-1}) is much smaller than the frequency of the incident laser light (of order 10^{15} s^{-1}), and is even much smaller than the bandwidth of the laser (of order 10^9 s^{-1}). This small frequency shift can be

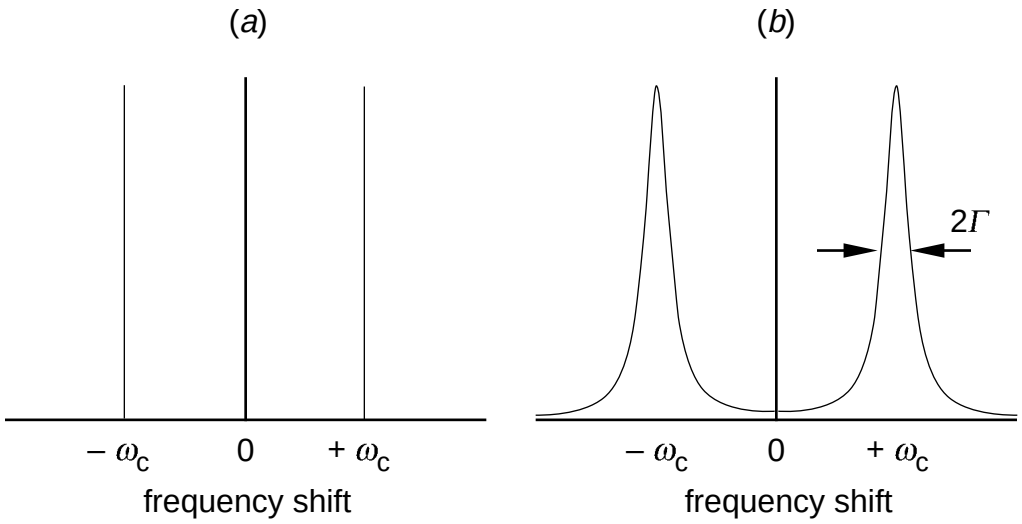

Figure 3.1. Frequency shift of scattered light for undamped (*a*) and damped (*b*) capillary waves. The undamped waves shift the frequency by exactly $\pm\omega_c$. The damped waves have a Lorentzian spectrum whose width is determined by the temporal damping constant Γ of the waves.

measured with a heterodyne technique;[3] the scattered light is combined with a local oscillator, a beam whose frequency has been shifted by an amount ω_{LO} from the frequency of the incident beam. If the scattered light is shifted by ω_c, then the amplitude of the electric field at the detector is

$$E(t) = \left[\frac{1}{2}A\left(e^{-i(\omega_L+\omega_c)t} + e^{i(\omega_L+\omega_c)t}\right) + \frac{1}{2}B\left(e^{-i(\omega_L+\omega_{LO})t} + e^{i(\omega_L+\omega_{LO})t}\right)\right], \quad (3.12)$$

where A is the amplitude of the scattered light, and B is the amplitude of the local oscillator. The intensity of the detected light is therefore

$$\begin{aligned} I(t) = E^*E = A^2[\cos(\omega_L+\omega_c)]^2 + B^2[\cos(\omega_L+\omega_{LO})]^2 \\ + AB[\cos(\omega_{LO}-\omega_c) + \cos(2\omega_L+\omega_{LO}+\omega_c)] \end{aligned} \quad (3.13)$$

i.e., the Fourier transform of the detected light has frequency components at the frequencies of the scattered light ($\omega_L + \omega_c$) and of the local oscillator beam ($\omega_L + \omega_{LO}$), as well as at the beat frequency, ($\omega_{LO} - \omega_c$). Because the response time of the detector is on the order of 10^{-9} s, the detector averages over many periods of the optical frequencies. The signals at optical frequencies are therefore measured as being DC. The beat frequency, which is on the order of kHz, is low enough to be measured by the detector; the beat frequency can be determined by Fourier transforming the detected signal. The beat frequency can be measured even if it is much smaller than the bandwith of the laser. The bandwidth is determined by fluctuations in the phase of the laser light. As long as the path difference between the scattered beam and the LO beam is less than the coherence length of the laser the two beams are in phase, and the phase fluctuations do not affect the measurement.

3.1.3 Experimental setup

The experimental setup for the light scattering experiment is illustrated in Fig. 3.2. Light from an Argon-ion laser (488 nm) is split into two beams, a main beam (M) and a much weaker local-oscillator beam (LO). The frequency of the LO beam is shifted with a pair of acousto-optic modulators (AO). Two acousto-optic modulators are necessary because it is impractical to shift the frequency of the LO beam by less than 20 MHz with a single acousto-optic modulator. Instead, the first acousto-optic modulator shifts the frequency of the LO beam up by 40 MHz; the second shifts the frequency down by (40 MHz + ω_{LO}), where ω_{LO} is between 5 and 100 kHz, depending on the frequency of the capillary wave being studied. The LO beam is therefore shifted in frequency by $-\omega_{LO}$ relative to the main beam. The main

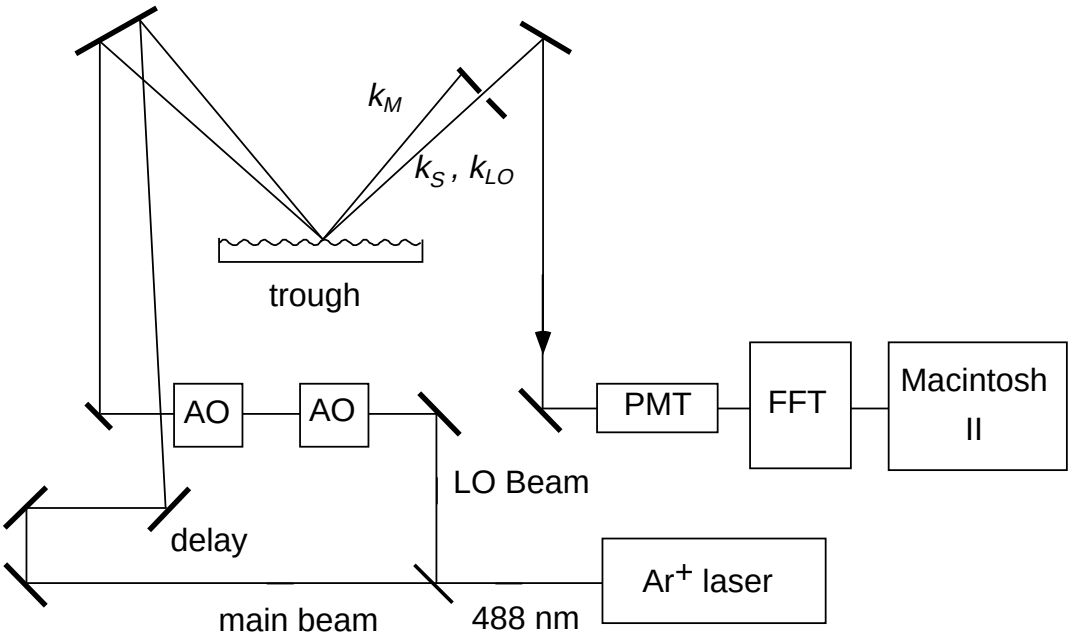

Figure 3.2. Experimental setup for surface light scattering; AO, acousto-optic modulator; PMT, photomultiplier tube; FFT, fast Fourier transform; LO, local oscillator. The pinhole separates the main beam from the scattered beam and the LO beam.

beam is sent through a variable delay to compensate for the extra optical path length that the LO beam encounters in the acousto-optic modulators; the difference in optical path between the main beam and the LO beam must be shorter than the coherence length of the laser.

The two beams are incident on the air/water interface in the same plane of incidence, but with slightly different angles of incidence. A pinhole blocks the reflected main beam, while allowing through the LO beam, as well as any scattered light that is colinear with the LO beam. The difference in angle between the main beam and the LO beam, $\Delta\theta$, therefore determines θ_s, the scattering angle of the light being studied. Since the plane of incidence is the same for the two beams, $q_y = 0$ for the capillary wave that scatters the light colinear to the LO beam. The wavevector of the capillary wave being studied can be determined from Eq. 3.6.

The light transmitted through the pinhole is detected with a photomultiplier tube. The signal is digitized and Fourier transformed to measure the beat frequency of the scattered light with the LO beam; a sample spectrum is shown in Fig. 3.3. The resulting data is fit with a Voigt function, the convolution of a Lorentzian with a Gaussian; this takes into account both the Lorentzian line shape of the scattered light and the Gaussian instrumental broadening, which will be discussed further in Chapter 4. The width of the Lorentzian contribution to the fit yields the capillary wave damping constant, Γ.

3.2 Brewster angle microscopy

Many questions about Langmuir monolayers can easily be addressed if the macroscopic morphology of the system can be directly imaged, *i.e.*, with

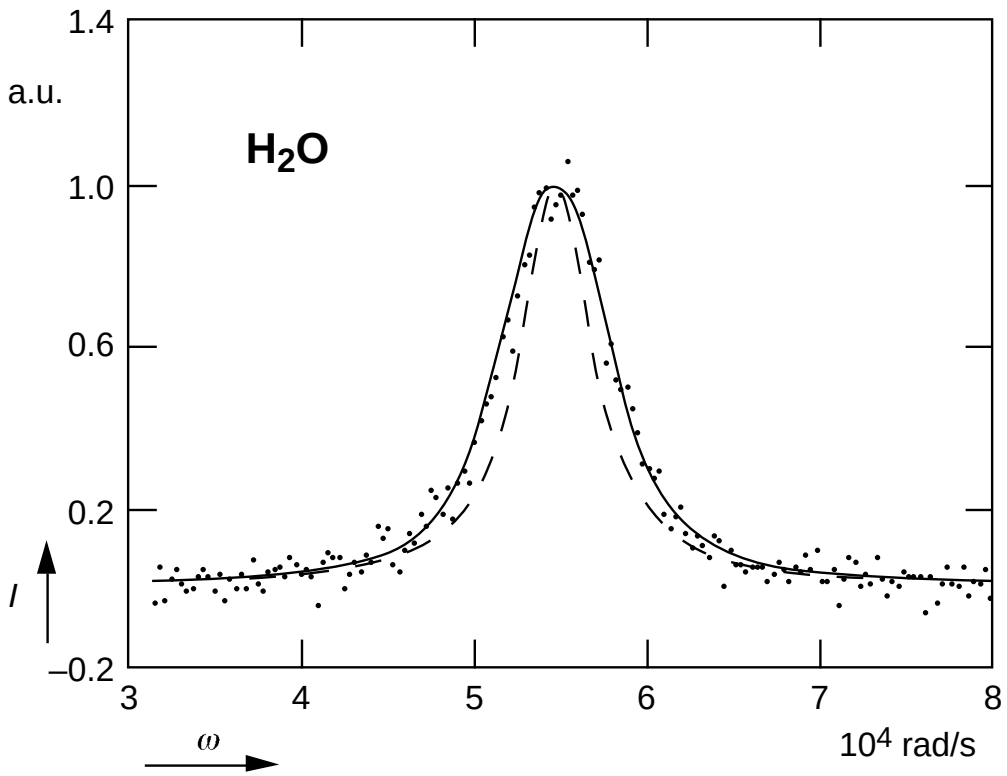

Figure 3.3. Sample spectrum measured with the heterodyne light scattering technique. The data are fit with a Voigt function to account for the instrumental broadening. The dashed line shows the Lorentzian contribution to the fit.

microscopy. For example, if a microscope image shows phase coexistence, it is clear that the phase transition being studied is first-order. One method that yields images of monolayer morphology is fluorescence microscopy,[4, 5] which involves the addition of an amphiphilic dye molecule to the monolayer. If the monolayer is in a coexistence region and the dye is preferentially soluble in one of the monolayer phases, imaging the fluorescence of the dye yields images of the monolayer morphology. However, this technique has the disadvantage that it requires the addition of a fluorescent dye, which may effect the monolayer phase behavior, to the monolayer.

3.2.1 Brewster angle microscopy — concept

In order to avoid using fluorescent dyes, it is preferable to use a microscopy technique that images light reflected by the monolayer. However, since Langmuir monolayers are much thinner than an optical wavelength, they reflect only a small amount of light. The reflectivity of the monolayer can be estimated by considering the reflectivity from a three layer system; a semi-infinite layer of air with refractive index $n_1 = 1$, a monolayer with refractive index n_2 and thickness $t \approx 1$ nm, and a semi-infinite layer of water, with refractive index $n_3 = 1.34$. The reflectivity for *p*-polarized light incident on such a three layer system is given by[6]

$$R = \frac{r_{12}^2 + r_{23}^2 + 2r_{12}r_{23}\cos\beta}{1 + r_{12}^2 r_{23}^2 + 2r_{12}r_{23}\cos\beta} \tag{3.14}$$

where

$$\beta = \frac{4\pi}{\lambda} n_2 t \tag{3.15}$$

and λ is the wavelength of the incident light, and where

$$r_{ab} = \frac{n_b \cos(\theta_a) - n_a \cos(\theta_b)}{n_b \cos(\theta_a) + n_a \cos(\theta_b)} \tag{3.16}$$

is the ratio of the reflected electric field to the incident electric field at the interface between two semi-infinite media, *a* and *b*, and θ_a is the angle that the light makes with the surface normal in medium *a*.

The difference in reflectivity (for $\lambda = 633$ nm) between a monolayer covered interface ($n_2 = 1.5$) and a pure air/water interface is shown in Fig. 3.4*a*. The largest

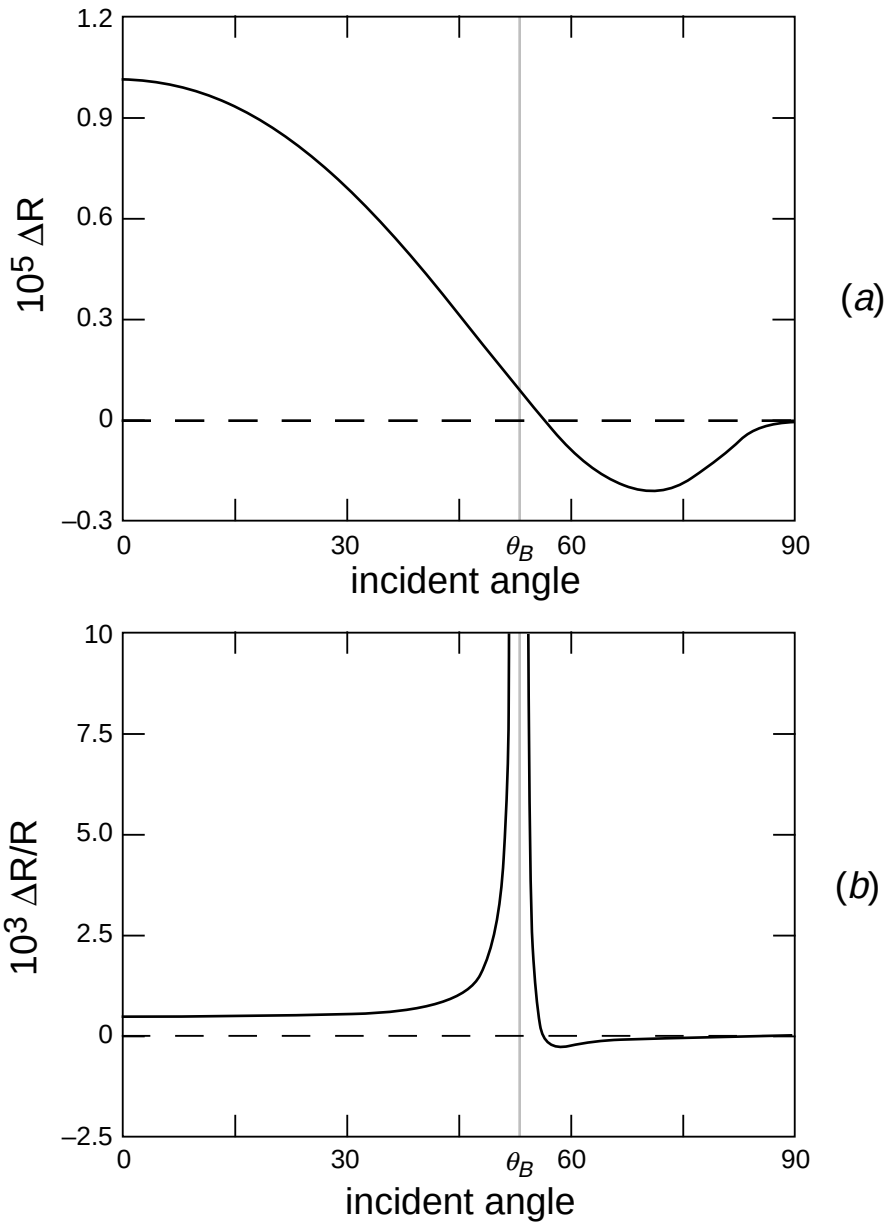

Figure 3.4. (*a*) Change in reflectivity and (*b*) relative change in reflectivity due to a monolayer. While the maximum change in reflectivity due to the monolayer is at an incident angle of 0°, the maximum relative change in the reflectivity (which gives the best signal to noise ratio) is at the Brewster angle of water, θ_B.

change in reflectivity, of order 10^{-5}, occurs at normal incidence. However, at normal incidence the reflectivity from the bulk water is approximately 0.02, and distinguishing between the monolayer and the bulk water would require a signal to

noise ratio better than 1 part in 10^3. Figure 3.4*b* shows the relative reflectivity — the change in reflectivity due to the monolayer divided by the reflectivity of the pure air/water interface — as a function of incidence angle. As the figure shows, the largest change in relative reflectivity occurs at the Brewster angle for water (θ_B = $\tan^{-1}(1.34) \approx 53°$), when the reflectivity of the air/monolayer/water system is approximately 10^{-6}.

3.2.2 Experimental setup

The experimental setup for the Brewster angle microscope[7, 8] is shown in Fig. 3.5. Light from a HeNe or Argon ion laser is *p*-polarized with a Glan-Thompson polarizer and is incident on the air/water interface at the Brewster angle of water. If the interface is covered with a Langmuir monolayer, there is a finite reflectivity; the reflected light is imaged onto a CCD camera with a single lens. If the monolayer is

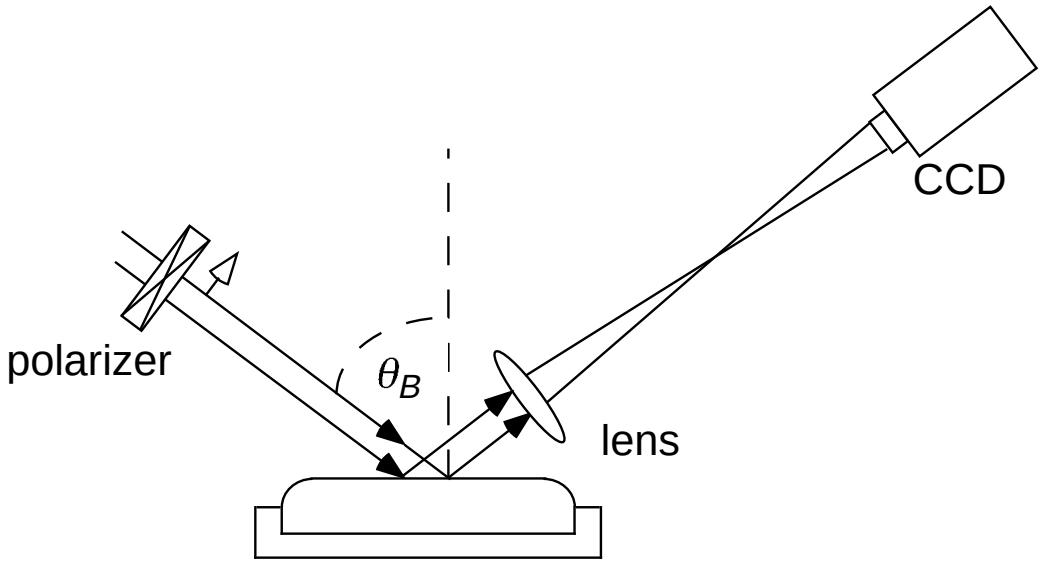

Figure 3.5. Experimental setup for Brewster angle microscopy. *p*-polarized light is incident on the air/water interface at the Brewster angle of water. Light reflected by the monolayer is imaged onto a CCD camera using a single lens.

in a coexistence region between two phases, the phases have different reflectivities. As can be shown from Eq. 3.14, for $\beta \approx 0$ the change in reflectivity due to the monolayer is proportional to β^2. The reflectivity is therefore proportional to the square of the thickness and the square of the index of refraction of the monolayer (see Eq. 3.15).

3.2.3 Sample images

Figure 3.6*a* shows a Brewster angle microscope image of a pentadecanoic acid monolayer in the gas/liquid expanded coexistence region. The bright regions in the picture correspond to the denser liquid expanded (LE) phase; the dark regions are the less dense gas phase. Due to inhomogeneity in the monolayer, the fraction of the image in the LE phase is not indicative to the average fraction of the monolayer in the LE phase. Brewster angle microscopy studies have shown similar phase coexistence up to temperatures as high as 40 °C. These experiments clearly show that contrary to the claims of Kim and Cannell[9] and Hawkins and Benedek,[10] the gas/LE phase transition does not end in a critical point below 40 °C.

Figure 3.6*b* shows the monolayer after it has completed the transition to the LE phase. There is no phase coexistence, and the monolayer has uniform density, as is evident from the image. Figure 3.6*c* is taken just past the start of the liquid expanded/liquid condensed (LC) coexistence region. As was mentioned in the previous chapter, isotherm studies were ambiguous as to the order of this transition. As the phase coexistence clearly shows, the transition is first-order. The bright regions correspond to the denser LC phase, and the darker background corresponds to the less dense LE phase. As the monolayer is compressed further,

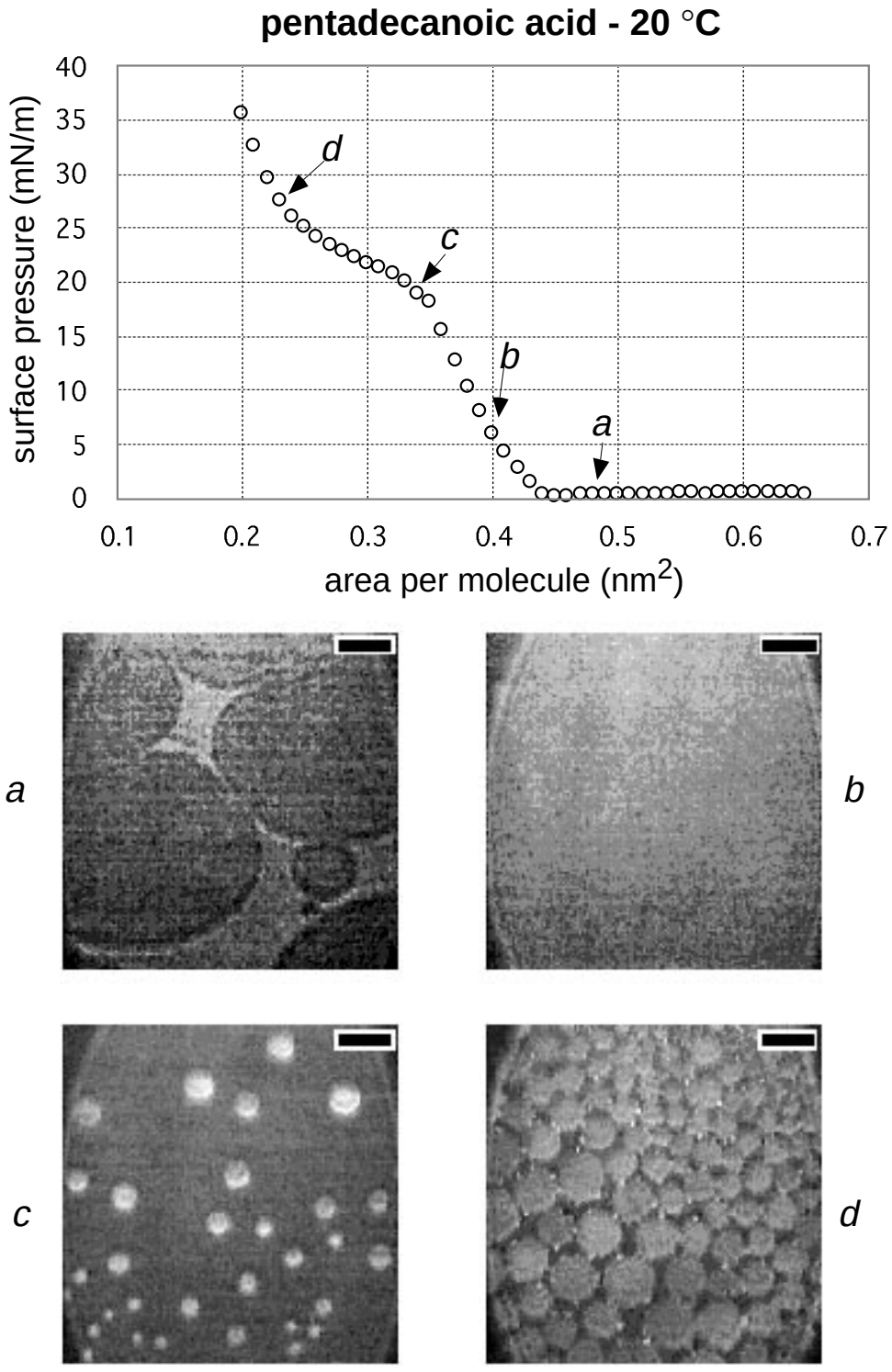

Figure 3.6. Isotherm and Brewster angle microscope images of a pentadecanoic acid monolayer on water with pH = 2. (*a*) is in the gas/liquid expanded coexistence region; (*b*) is in the liquid expanded phase; and (*c*) and (*d*) are in the liquid expanded/liquid condensed coexistence region. The length of the white bar in each image is 200 μm.

the pressure rises steeply. As is evident in Fig. 3.6*d*, the monolayer at this point is still in the LE/LC coexistence region. However, there are also many small bright points, corresponding to regions where the monolayer has collapsed into three-dimensional crystallites.

3.2.4 Experimental limitations

The main limitation of Brewster angle microscopy is evident in Fig. 3.5 — the monolayer is tilted at an angle of 53° relative to the optical axis of the lens. Therefore, if the center of the image is in focus, the top and bottom are behind and in front of the object plane of the lens, respectively, leaving only a narrow strip focussed, as shown in Fig. 3.7. The amount of the defocusing depends on the spatial resolution of the lens; two methods, discussed below, have been developed to address this problem.

The two methods use different tradeoffs between the spatial resolution and the depth of focus of the microscope. The theoretical spatial resolution and depth of focus of an imaging lens are dependent on its numerical aperture, which is equal to one half the ratio of the diameter D of the lens to its focal length, f. Specifically, the size of the smallest spatial feature that can be resolved, a, is inversely proportional to the numerical aperture,[11]

$$a = \frac{1.2\lambda f}{D} \tag{3.17}$$

while the depth of focus, d, is inversely proportional to the square of the numerical aperture,[12]

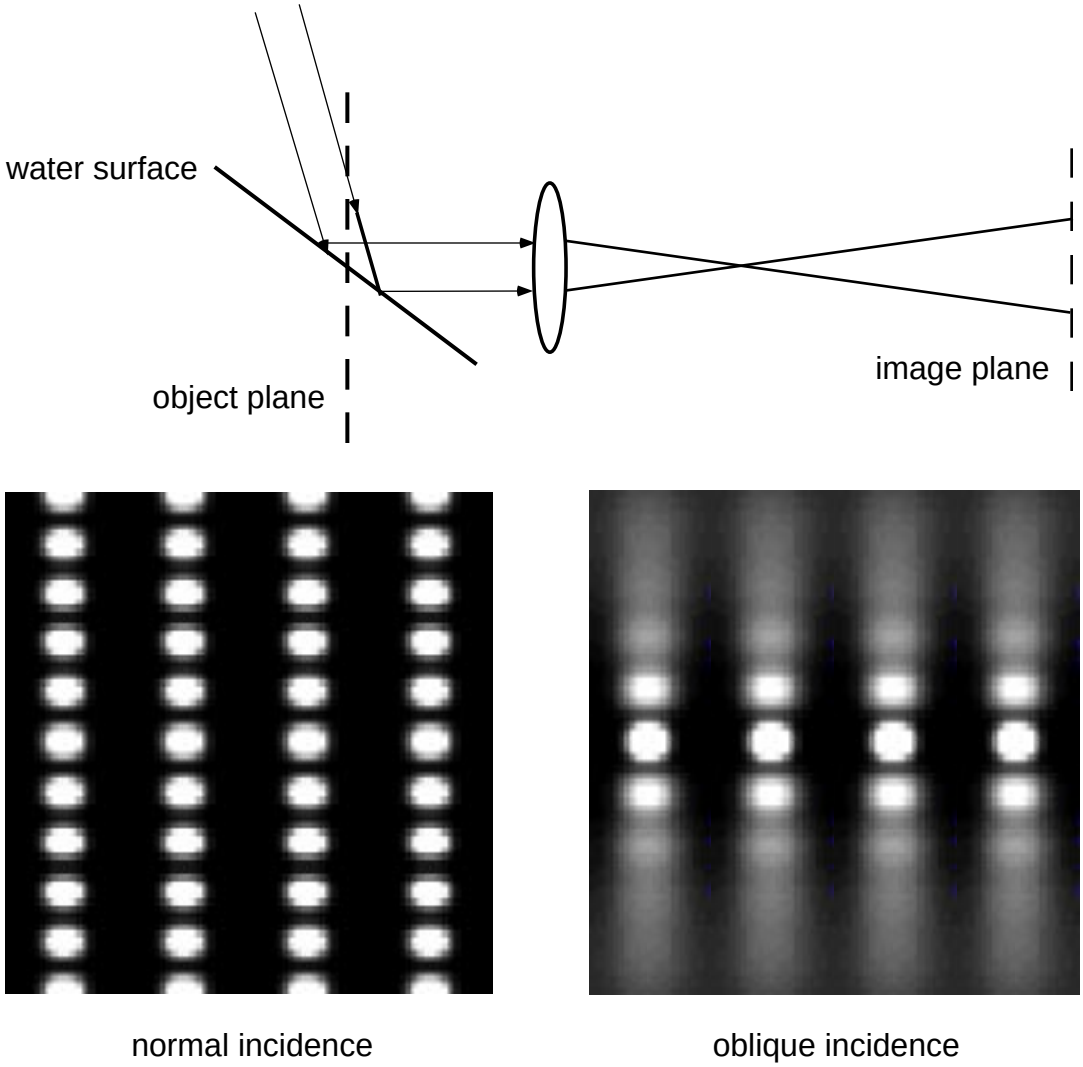

Figure 3.7. Defocusing of an array of points due to the tilt of the surface relative to the imaging system. In the case of a tilted surface, only a narrow strip of the image is in focus.

$$d = \pi\lambda\left(\frac{f}{D}\right)^2 \tag{3.18}$$

where λ is the wavelength of the laser light. One type of Brewster angle microscope[7] uses a lens with a large numerical aperture, and therefore high spatial resolution and small depth of focus. The image is in focus only for a narrow strip of the surface. High-resolution images are obtained by translating the imaging lens

and combining the strips that are in focus for each position of the lens to obtain a complete picture. The disadvantage of this technique is that it relies on the monolayer remaining stable during the time needed to acquire the images, which is on the order of several seconds. Therefore, this method cannot be used to study dynamic processes which occur on time scales of less than several seconds, or if there is significant drift of the monolayer.

A second approach[8] is to choose a lens with a numerical aperture that yields an acceptable resolution and enough depth of focus so that a large portion of the image is in focus. The advantage of this compromise is illustrated in Fig. 3.8, which shows the size of the smallest possible spot formed on the image plane as a function of the defocusing of the image (*i.e.*, the distance of the imaged spot from the image plane) for two different microscope resolutions. While the 1-μm

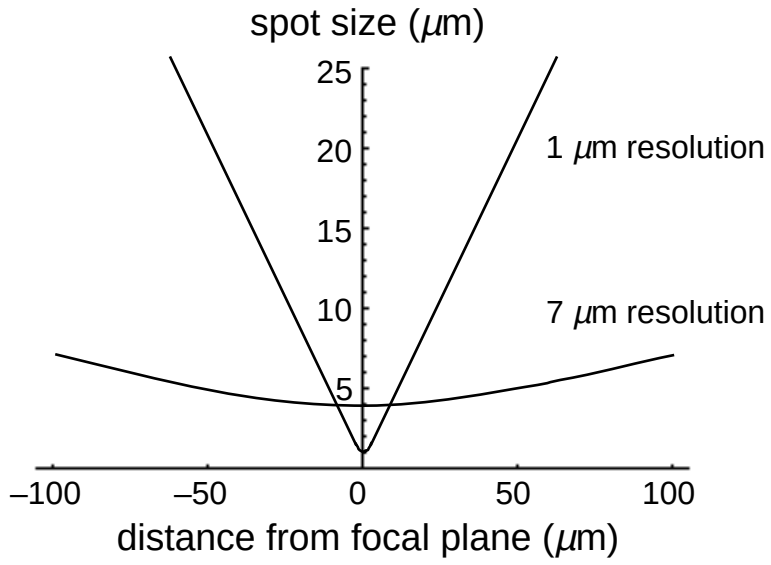

Figure 3.8. Comparison of defocusing for a microscope with two resolutions, 1 μm and 7 μm. While the microscope with 1-μm resolution forms a smaller spot at the focal plane, if the image is defocused by more than 8.5 μm the microscope with 7-μm resolution forms the smaller spot.

resolution yields a better resolution for a strip of width ≈ 17 μm centered on the image plane (*i.e.*, ±8.5 μm from the image plane, where the two curves in Fig. 3.8 intersect), for larger deviations from the image plane the resolution is actually better at 7-μm resolution. For example, if 10-μm resolution is sufficient for an experiment, a microscope with 1-μm resolution yields a resolution of 10 μm or better for a strip approximately 25 μm wide; the same strip is approximately 125 μm wide for a microscope with 7-μm resolution.

The experiments described in this thesis use this second approach. For example, the Brewster angle microscope used in the experiments described in Chapters 4 and 5 uses an Argon ion laser ($\lambda \approx 500$ nm) and a 25-mm diameter, 175-mm focal length lens, yielding a resolution of 4.3 μm, and a depth of focus of 80 μm.

3.3 Brewster angle microscopy — orientational order

In the previous section we discussed the use of Brewster angle microscopy for imaging the coexistence between monolayer phases with different density, and therefore different reflectivity. The model that we used to estimate the reflectivity of the monolayer (see Eq. 3.14) implicitly assumes that the monolayer is optically isotropic. For an isotropic monolayer, the reflected light has the same polarization as the incident light — it is *p*-polarized. However, as we mentioned in Chapter 2, some monolayer phases have quasi-long-range orientational order — the molecules are all tilted in the same direction over a macroscopically large distance (on the order of μm). Because the polarizability of amphiphilic molecules is anisotropic (it is greater along the long axis of the molecule than across the molecule) monolayer

phases with quasi-long-range tilt order are optically anisotropic. The result of this anisotropy is that the polarization of the light reflected by the monolayer can be rotated from *p*-polarized. The amount that the polarization is rotated depends on the orientation of the molecule.[13] In this section we discuss the quantitative effect of the optical anisotropy.

3.3.1 Theoretical model

For optically isotropic media, ignoring non-linear effects, the polarization **P** induced by an electric field is proportional to the strength of the applied field:

$$P_i = \varepsilon E_i \tag{3.19}$$

where ε is the frequency-dependent dielectric constant of the material. For anisotropic media, the magnitude and direction of **P** depend on both the direction and magnitude of **E**:

$$P_i = \varepsilon_{ij} E_j \tag{3.20}$$

where ε_{ij} is a 3×3 tensor of rank two. Note that the direction of **P** is not necessarily parallel to **E**. Therefore, if *p*-polarized light strikes an anisotropic medium, the polarization induced in the medium may have a component perpendicular to the plane of incidence, leading to *s*-polarized reflected light. For the case of a Langmuir monolayer we assume that the molecules have cylindrical symmetry, *i.e.*, that ε_{ij} is given by:

$$\varepsilon_{ij} = \begin{bmatrix} \varepsilon & 0 & 0 \\ 0 & \varepsilon & 0 \\ 0 & 0 & \varepsilon + \Delta \end{bmatrix} \tag{3.21}$$

where the $\hat{\mathbf{z}}$-axis is along the long axis of the molecule. If the monolayer has quasi-long-range orientational order, the molecules are tilted from the interface normal by an angle φ, and the projection of the molecule onto the surface makes an angle θ with the $\hat{\mathbf{x}}$-axis, where the plane of incidence is taken to be the xz-plane, and the light is propagating in the positive $\hat{\mathbf{x}}$ direction (see Fig. 3.9).

In this reference frame ε_{ij} is given by

$$\varepsilon_{ij} = \begin{bmatrix} \varepsilon + \Delta(\cos\theta\sin\varphi)^2 & -\Delta\cos\theta\sin\theta(\sin\varphi)^2 & \Delta\cos\theta\cos\varphi\sin\varphi \\ -\Delta\cos\theta\sin\theta(\sin\varphi)^2 & \varepsilon + \Delta(\sin\theta\sin\varphi)^2 & -\Delta\sin\theta\sin\varphi\cos\varphi \\ \Delta\cos\theta\cos\varphi\sin\varphi & -\Delta\sin\theta\sin\varphi\cos\varphi & \varepsilon + \Delta(\cos\varphi)^2 \end{bmatrix} \tag{3.22}$$

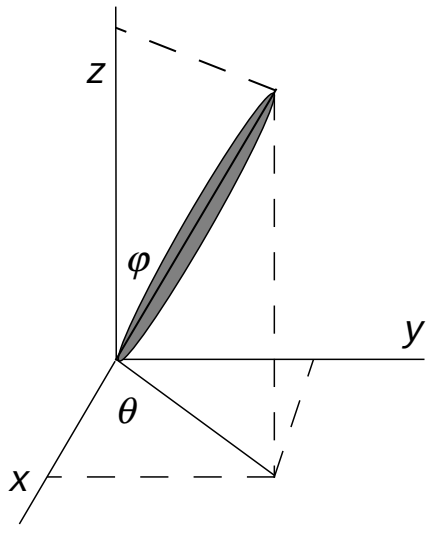

Figure 3.9. Definition of the molecular orientation angles φ and θ. The z-direction is normal to the surface. The xz-plane is the plane of incidence; the light travels in the positive x-direction. The molecule is tilted by an angle φ from the z-axis. the projection of the molecule onto the surface makes an angle θ with the x-axis.

A general method for calculating optical propagation in media with anisotropic optical properties using 4×4 matrices was developed by Berreman.[14] The light is assumed to be monochromatic, with time dependence $e^{-i\omega t}$; time derivatives can be replaced with multiplication by $-i\omega$. The plane of incidence is chosen to be the xz-plane, and we assume that the dielectric constant is a function of z only. Therefore, k_x is constant in all of the media, and $k_y = 0$. Partial derivatives with respect to x can be replaced with multiplication by ik_x. Taking the isotropic magnetic permeability to be $\mu = 1$ and assuming that the material is not optically active (*i.e.*, that the propagation of right- and left-circularly polarized light in the material is equivalent) Maxwell's equations reduce to

$$\frac{\partial}{\partial z}\psi_i = \frac{i\omega}{c} T_{ij}\psi_j \tag{3.23}$$

where

$$\mathbf{T} = \begin{bmatrix} -\dfrac{k_x\varepsilon_{xz}}{k\varepsilon_{xz}} & -\dfrac{k_x\varepsilon_{yz}}{k\varepsilon_{xz}} & 0 & 1-\left(\dfrac{k_x}{k}\right)^2\dfrac{1}{\varepsilon_{zz}} \\ 0 & 0 & -1 & 0 \\ \left[-\varepsilon_{xy}+\dfrac{\varepsilon_{xz}\varepsilon_{yz}}{\varepsilon_{zz}}\right] & \left(\dfrac{k_x}{k}\right)^2-\varepsilon_{yy}+\dfrac{\varepsilon_{yz}^2}{\varepsilon_{zz}} & 0 & \dfrac{k_x\varepsilon_{yz}}{k\varepsilon_{xz}} \\ \varepsilon_{xx}+\dfrac{\varepsilon_{xz}^2}{\varepsilon_{zz}} & \varepsilon_{xy}-\dfrac{\varepsilon_{xz}\varepsilon_{yz}}{\varepsilon_{zz}} & 0 & -\dfrac{k_x\varepsilon_{xz}}{k\varepsilon_{xz}} \end{bmatrix} \tag{3.24}$$

and the vector ψ is composed of the four independent components of the electric and magnetic field vectors,

$$\psi = \begin{bmatrix} E_x \\ E_y \\ H_x \\ H_y \end{bmatrix}, \tag{3.25}$$

If **T** is independent of z over some distance from z_0 to $z_0 + \Delta z$, a formal solution to Eq. 3.23 is given by

$$\psi(z_0 + \Delta z) = e^{(i\omega \mathbf{T}/c)\Delta z}\psi(z_0) \equiv \mathbf{L}(\Delta z)\,\psi(z_0) \tag{3.26}$$

Boundary conditions require that ψ be continuous across an interface. In the air there are two propagating beams, an incident beam ψ^i and a reflected beam ψ^r. In the water there is only a transmitted beam, ψ^t. The field at the top surface of the monolayer is given by $\psi^i(0) + \psi^r(0)$, and at the bottom surface it is $\psi^t(h)$, where the top and bottom boundaries of the monolayer are at $z = 0$ and $z = h$, respectively. From Eq. 3.26 we therefore have

$$\psi^t(h) = \mathbf{L}(h)\,(\psi^i(0) + \psi^r(0)) \tag{3.27}$$

For monolayer films $\frac{\omega h}{c} \ll 1$, and all of the elements of **T** are of order unity. **L** can then be approximated as

$$\mathbf{L}(h) \approx \left(\mathbf{I} + i\frac{\omega h}{c}\mathbf{T}\right). \tag{3.28}$$

In isotropic media ψ has only two independent components. Therefore, since the incident field ψ^i is known, Eq. 3.27 provides a set of four linear equations with four unknowns.

For Brewster angle microscopy one has only *p*-polarized incident light, but both *p*- and *s*-polarized reflected light:

$$\begin{aligned} \mathbf{E}_p^r &= r_{pp}\mathbf{E}_p^i \\ \mathbf{E}_s^r &= r_{ps}\mathbf{E}_p^i \end{aligned} \quad . \tag{3.29}$$

Relative to the intensity of the incident light, the intensity of the reflected light is

$$I = (r_{pp})^2 + (r_{ps})^2 \tag{3.30}$$

and the polarization of the light is rotated from the plane of incidence by an angle

$$\Theta = \text{atan}\left(\frac{r_{ps}}{r_{pp}}\right). \tag{3.31}$$

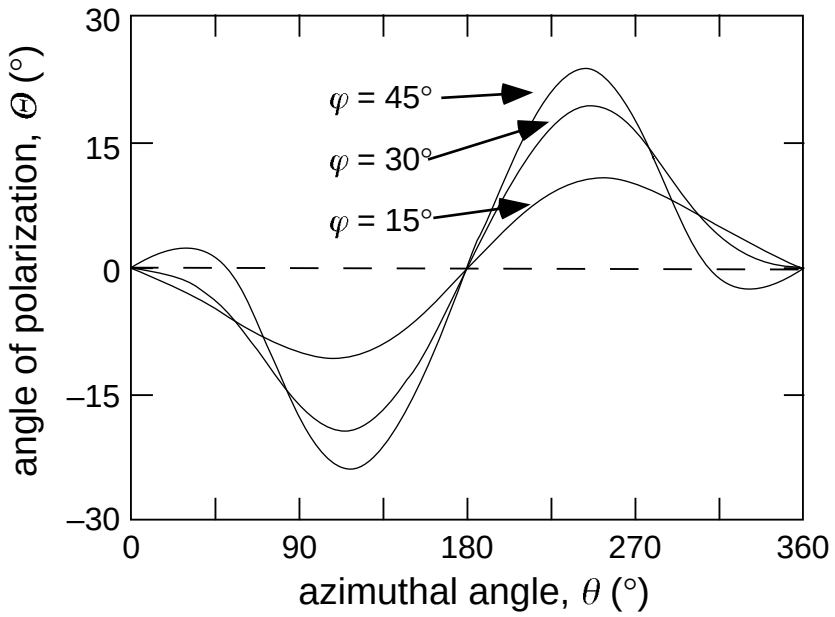

Figure 3.10. Dependence of the angle of polarization (*p*-polarized = 0°) as a function of azimuthal angle for three different tilt angles. The range of polarizations reflected depends on the tilt angle, φ. If φ is known, measurement of the angle of polarization determines the azimuthal angle to be one of either two or four values.

For any given ε and Δ we can calculate r_{pp} and r_{ps}. Figure 3.10 shows the dependence of the angle of polarization of the light on the azimuthal angle θ for three different tilt angles, φ = 15°, 30°, and 45°. To approximate the values for a long-chain fatty acid we have chosen ε = 2.09 and Δ = 0.11 (this is discussed in more detail in Chapter 5); changing these values leads to a quantitative, but not qualitative, change in the curves.

In general, when a monolayer is in a phase with quasi-long-range orientational order, the azimuthal angle is not uniform for the entire monolayer; rather, the monolayer consists of many domains, as in Fig. 3.11. The different domains have different azimuthal angles; therefore, the light reflected from the different domains has different polarization. Figure 3.10 shows that if the tilt angle φ is known, measurement of the angle of polarization Θ determines the azimuthal

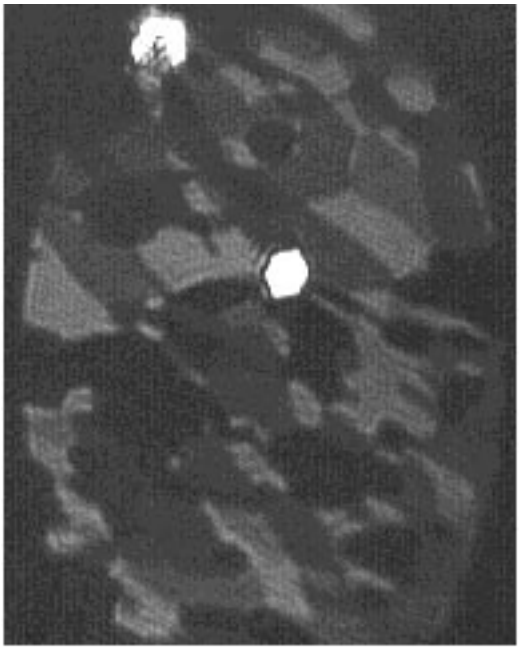

Figure 3.11. Brewster angle microscopy image of docosanoic acid ($C_{22}H_{44}O_2$), measuring only the *s*-polarized reflected light. Different intensities correspond to regions with different molecular orientation. The bright hexagon is a 3D crystallite.

angle θ to be one of either two or four values, depending on the tilt angle. More importantly, the range of values which Θ takes depends on the tilt angle, φ. Measuring the range of polarizations reflected by the monolayer yields an accurate determination of the tilt angle φ. In Chapter 5 we discuss the validity of this technique, and we use it to study the molecular tilt in monolayers of long-chain molecules.

References

1 D. K. Schwartz, M. L. Schlossman, E. H. Kawamoto, *et al.*, Phys. Rev. A **41**, 5687 (1990).

2 L. D. Landau and E. M. Lifshitz, *Fluid Mechanics* (Pergamon, Oxford, 1959).

3 D. S. Chung, K. Y. Lee, and E. Mazur, Appl. Phys. B **64**, 1 (1997).

4 C. M. Knobler, Science **249**, 870 (1990).

5 H. M. McConnell, Annu. Rev. Phys. Chem. **42**, 171 (1991).

6 J. R. Reitz, F. J. Milford, and R. W. Christy, *Foundations of Electromagnetic Theory* (Addison-Wesley, Reading, 1979).

7 S. Henon and J. Meunier, Rev. Sci. Instrum. **62**, 936 (1991).

8 D. Honig and D. Mobius, J. Phys. Chem. **95**, 4590 (1991).

9 M. W. Kim and D. Cannell, Phys. Rev. A **13**, 411 (1976).

10 G. A. Hawkins and G. B. Benedek, Phys. Rev. Lett. **32**, 524 (1974).

11 E. Hecht, *Optics* (Addison-Wesley, Reading, 1987).

12 A. E. Siegman, *Lasers* (University Science Books, Mill Valley, 1986).

13 Y. Tabe and H. Yokoyama, Langmuir **11**, 699 (1995).

14 D. W. Berreman, J. Opt. Soc. Am. **62**, 502 (1972).

Chapter 4

Capillary Wave Damping in Heterogeneous Monolayers

The following chapter appeared as an article in the Journal of Physical Chemistry, Volume 98, No. 48, (1994) 12720

4.1 Abstract

We studied capillary wave damping in heterogeneous monolayers of triglyceride at the air/water interface over a range of surface wavelengths (70-300 μm) using a light scattering technique. In addition, we studied the monolayer morphology using a Brewster angle microscope. We found that the morphology has a strong effect on the capillary wave damping. In the gas-liquid expanded (G/LE) coexistence region the monolayer forms a two-dimensional foam structure, where 'bubbles' of gas phase are separated by regions of liquid expanded phase. If the width of the LE regions is smaller than the wavelength of the capillary wave, the monolayer has no measurable effect on the damping of the capillary wave. When the width of the LE regions is larger than the wavelength, the capillary wave damping constant increases from its value for a clean water surface. We attribute this increase to a rise in the dynamic dilational elasticity of the heterogeneous monolayer.

4.2 Introduction

Molecular monolayers on liquid surfaces have been studied extensively using a variety of techniques including x-ray scattering,[1, 2] non-linear optical techniques,[3] and optical microscopy.[4, 5] In addition, light scattering has been used to measure the viscoelastic properties of monolayers at the liquid-vapor interface through the monolayers' effects on capillary wave propagation.[6-8] Spatial damping measurements use externally generated low frequency (f < 3 kHz) capillary waves,[9, 10] while temporal damping measurements rely on higher-frequency thermally-generated capillary waves.[6, 7] For a clean liquid surface, capillary waves are governed by the restoring force of surface tension and are damped by viscous dissipation within the bulk liquid. When the surface is covered by a molecular monolayer, other surface viscoelastic properties, such as the dilational elastic modulus of the monolayer, affect the capillary wave frequency and damping constant. A hydrodynamic theory has been developed to describe the capillary wave propagation on liquid surfaces covered by a homogeneous monolayer.[11] However, in phase coexistence regions the monolayer is heterogeneous. This heterogeneity can be imaged using fluorescence microscopy[12] or Brewster angle microscopy.[13, 14] For example, in the gas/liquid-expanded (G/LE) coexistence region, the surface is only partially covered by the monolayer in the liquid-expanded (LE) phase while the rest of the area is in the gaseous (G) phase. When the monolayer is heterogeneous, the damping of the capillary waves is affected by the presence of LE regions, and the wave propagation shows quite a different behavior from that of a homogeneous monolayer.[7, 9, 10, 15] Until now, most light

scattering studies have focused on homogeneous monolayers[6, 16-18] and little attention has been paid to heterogeneous monolayers. Recently, a theoretical description of capillary wave damping has been developed for systems where the spacing between domains is much larger than the capillary wavelength, and the domain size is much smaller than the wavelength.[19]

When Earnshaw *et al.*[7] investigated glycerol mono-oleate monolayers on water, they noted that the temporal damping of the capillary waves sometimes, but not always, increases dramatically at large molecular areas (area/molecule $A \approx 7$ nm^2) from its value for a clean water surface. The authors attribute this irreproducibility to the inhomogeneity of the monolayer. Lee *et al.*[9] measured the spatial damping of low-frequency capillary waves at the air/water interface covered by a monolayer of pentadecanoic acid. The damping constant increases by a factor of five near the high-density end of the G/LE coexistence region. Since existing theories[11] do not explain such an increase as a function of surface concentration, the increase was attributed to inhomogeneities. Miyano and Tamada[15] also studied the spatial damping of capillary waves on water surfaces covered by inhomogeneous monolayers. They found that a liquid monolayer does not affect the capillary waves significantly until it covers more than 90% of the water surface, and concluded that the dynamic elasticity of the monolayer is extremely low.[15] Their work on porphyrin films in a gas/multilayer coexistence region shows that the capillary wave characteristics depend on the macroscopic structure of the films.[10]

In this paper we focus on the damping of capillary waves by a monolayer of triglyceride in the G/LE coexistence region over a range of capillary wavelengths (λ = 70-300 μm or f = 4-35 kHz). In addition, we present data on the morphology of the monolayer obtained through Brewster angle microscopy. Using this combination of techniques we find that the damping behavior is strongly affected by the morphology of the monolayer. The presence of the monolayer only affects the capillary wave damping when the width of the LE regions becomes larger than the capillary wavelength.

4.3 Theory

A capillary wave is a transverse surface wave whose restoring force is the surface tension. For a capillary wave of frequency ω, the vertical displacement ζ of the surface from its equilibrium position can be written as

$$\zeta = \zeta_0 e^{i(qx + \omega t)} \tag{4.1}$$

where ζ_0 is the amplitude of the wave, q is the wave vector, and x is the direction of wave propagation. The frequency is a complex quantity, $\omega = \omega_0 + i\Gamma$, where the imaginary component represents the temporal damping constant. The dispersion relation for the capillary waves has been discussed by Lucassen for the case of a homogeneous monolayer, and is given by:[11]

$$[\varepsilon q^2 + i\omega\eta(q+m)][\sigma q^2 + i\omega\eta(q+m) - \omega^2\rho/q] + [\omega\eta(q-m)]^2 = 0 \tag{4.2}$$

where σ is the surface tension, η is the shear viscosity of the liquid, ρ is the density of the liquid, and

$$m = \sqrt{q^2 + i\omega\rho / \eta} \tag{4.3}$$

For monolayers in the liquid expanded phase, where the surface viscosity is very small,[7] ε corresponds to the surface dilational modulus.

The temporal damping constant Γ is a function of the surface dilational modulus.[11] Figure 4.1 shows this damping constant Γ versus ε/σ for a wavelength λ = 162 μm (q = 389 cm^{-1}) obtained from the above theory.[11] In the calculation, the surface tension σ is kept constant at 71.97 mN/m and the surface dilational modulus ε is varied. As ε increases, the damping constant Γ passes through a maximum and then decreases. The peak in the damping constant corresponds to ε/σ = 0.16, independent of the capillary wavelength. For $\varepsilon \geq \sigma$, Γ varies slowly with ε. ε = 0 corresponds to the case of a clean water surface.

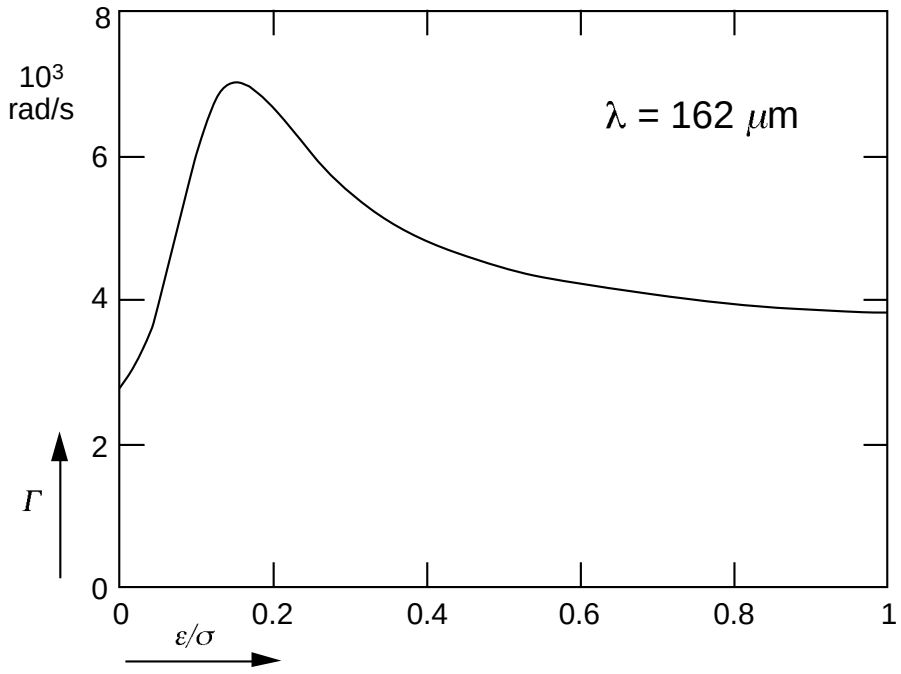

Figure 4.1. Calculated temporal damping constant for a capillary wave of wavelength λ = 162 μm (q = 389 cm^{-1}) at a liquid surface with a surface tension of 71.97 mN/m.

4.4 Experimental

We used a heterodyne light scattering technique[20] to measure the damping of capillary waves generated by thermal fluctuations. The amplitude of these capillary waves is about 0.3 nm.[21] For the experiments described here, the capillary wavelength is in the range 70-300 μm. Figure 4.2 shows a schematic diagram of the experimental setup. Light from an Ar+ laser (488 nm) is split into two beams, a main beam and a much weaker local oscillator (LO) beam. A pair of acousto-optic modulators shift the frequency of the LO beam by a fixed frequency between 5 and 100 kHz depending on the frequency of the capillary wave. The frequency shift between the main and the LO beams keeps their beating signal away from zero

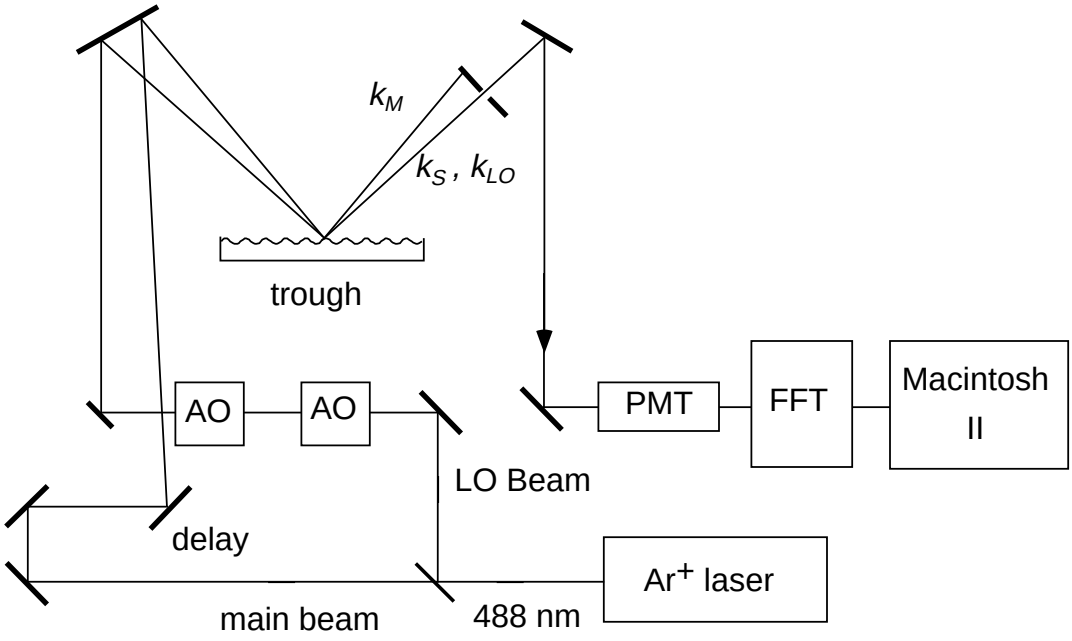

Figure 4.2. Schematic diagram of the experimental setup. AO: acousto-optic modulator; PMT: photo multiplier tube; FFT: fast Fourier transformer; LO: local oscillator. The pinhole separates the main beam from the scattered beam and the LO beam (k_{LO})

frequency, where self-beating from the LO beam and $1/f$ noise produce a large background.

The main beam and the LO beam overlap on the liquid surface. Because of conservation of momentum, the angle at which light is scattered by a capillary wave is determined by the wavevector of that capillary wave. To select a capillary wave of a given wavevector, the angle $\Delta\theta$ between the main beam and the LO beam is adjusted so that only light scattered by that capillary wave is colinear with the LO beam. The beating of the scattered light with the LO beam is then detected with a PMT, and the signal from the PMT is amplified and Fourier transformed to obtain the power spectrum of the scattered light.[20]

The spectrum of the scattered light is broadened by instrumental effects. Because of the divergence of the laser beam, the detector measures the light scattered by waves having a range of wavevectors (~40 cm^{-1}) about the selected value. Were it not for instrumental broadening, the spectrum of the scattered light would be approximately Lorentzian in shape.[7] When combined with instrumental effects, however, the observed spectrum is the convolution of this Lorentzian with an instrumental function. For a laser beam with a Gaussian profile this instrumental function is a Gaussian; the observed spectrum is therefore a convolution between a Lorentzian and a Gaussian, which is a Voigt function.[22]

To separate the instrumental broadening from the unbroadened spectrum, we fitted our measured spectra with a Voigt function. Figure 4.3 shows a sample power spectrum for q = 365 cm^{-1}. The data points are fit with a Voigt function (solid curve); also shown is the unbroadened (Lorentzian) spectrum which is

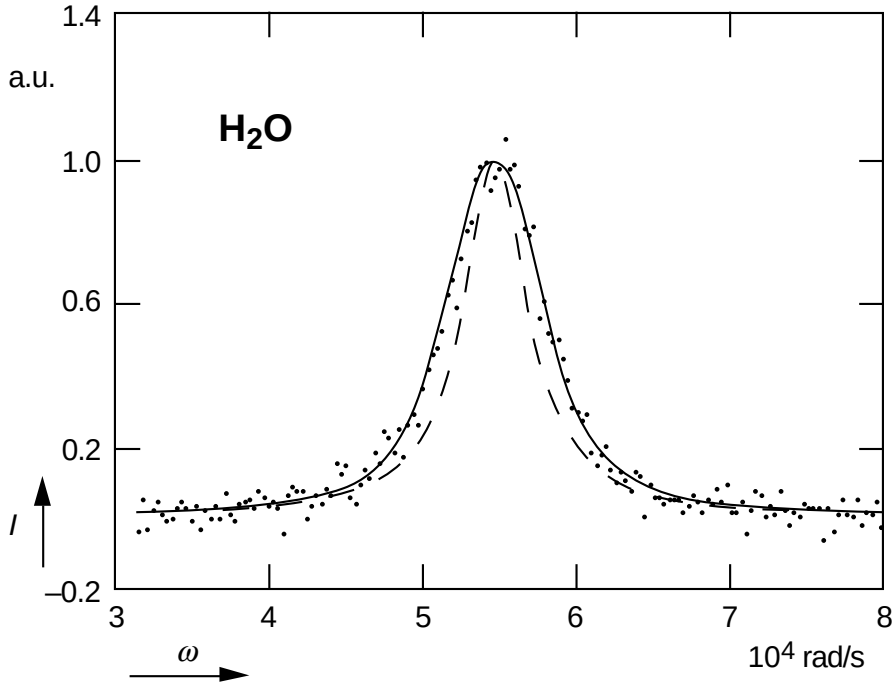

Figure 4.3. Light scattering spectrum for q = 365 cm^{-1}. The raw data is fit with a Voigt function (solid line). The dotted line represents the Lorentzian contribution to the Voigt profile.

obtained with the fitting procedure (dashed curve). The effect of instrumental broadening is apparent. We tested this method of correcting for the instrumental broadening by measuring the capillary wave damping for a clean water surface. Figure 4.4 shows the experimental damping constants, with a solid line corresponding to the damping constant obtained from hydrodynamic theory, $\Gamma = 2(\eta / \rho)q^2$, where η and ρ are the viscosity and the density of water respectively, and q is the wavevector of the capillary wave.[9] The agreement is very good except at small wavevectors. We calculated the instrumental broadening which is due to the divergence of the laser; this value sets a lower bound on the actual instrumental broadening. For q = 500 cm^{-1} the measured damping constant is approximately 4400 rad/s while the instrumental broadening is at least 5400 rad/

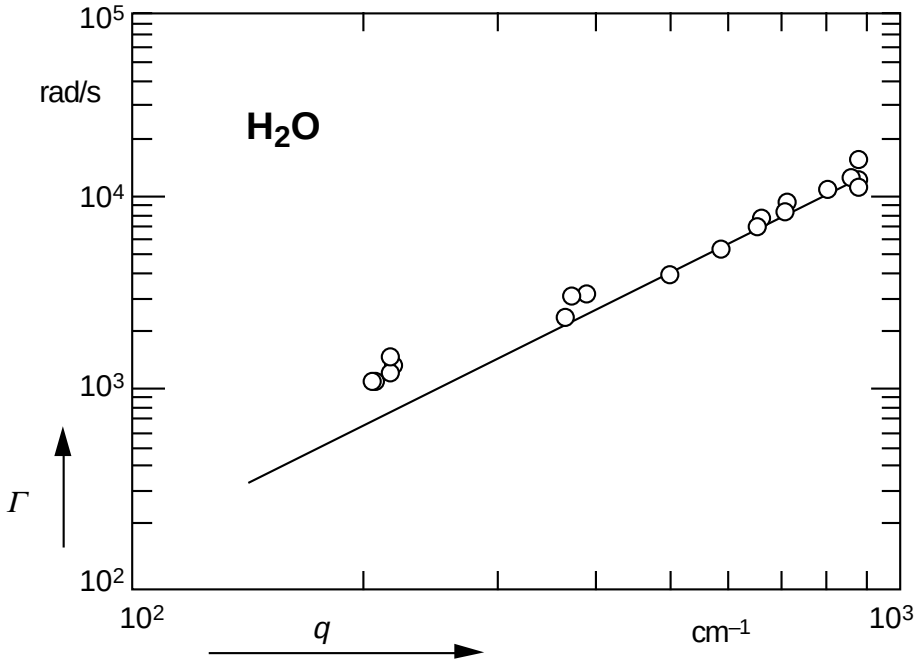

Figure 4.4. Temporal damping constant Γ for capillary waves on a clean water surface at T = 25.0 °C. The open circles represent the results obtained by fitting the measured spectra with a Voigt function as in Fig. 4.3. The line represents the theoretical expression $\Gamma = 2(\eta/\rho)q^2$

s. For larger values of q, the instrumental broadening becomes narrower than the unbroadened spectrum. For smaller values of q the instrumental broadening becomes much wider than the unbroadened spectrum, and the fitting technique is no longer an effective way to extract the width of the unbroadened spectrum. As Fig. 4.4 shows, however, the Voigt function fitting technique works very well, even when the instrumental broadening is as wide as the unbroadened spectrum.

In addition to using light scattering to measure the capillary wave damping, we used a Brewster angle microscope (BAM) to study the morphology of the monolayer. The details of this technique can be found elsewhere.[13, 14] Our Brewster angle microscope is similar to the one described by Honig and Mobius.[13] Briefly, when *p*-polarized light is incident at the air/water interface the reflectivity vanishes

at the Brewster angle. If the water surface is covered by a monolayer, the reflectivity will be non-zero since the monolayer has a different refractive index than the water subphase. By imaging this reflected light onto a CCD camera, one can distinguish those regions of the surface which are covered by the monolayer from those regions which are clean water subphase. Furthermore, since the reflectivity depends on the monolayer density, one can distinguish monolayer phases which have different density.

Using both techniques, we studied monolayers of triglyceride (C_{14}-C_{14}-C_{12}) at T = 25.0 °C. The two techniques were carried out on separate experimental apparatuses. However, every effort was made to ensure that all the conditions were the same for the two experiments. The triglyceride is comprised of three fatty acids esterified to glycerol.[23, 24] Triglyceride was purchased from Aldrich (99% pure) with no further purification, and was dissolved in HPLC-grade heptane. The subphase is pure water from a Millipore Milli-Q UV system (resistivity ≥ 18.2 MΩ/cm). The pH of the water is not adjusted and changes from 7.0 to about 5.7 over several hours. The triglyceride monolayer and water subphase are contained in a temperature-controlled Langmuir trough with a temperature stability of 0.1 °C. To prevent the contamination of the surface, the trough is placed inside a sealed chamber filled with ultra pure nitrogen gas (99.999%). Surface tension is measured with a filter-paper Wilhelmy plate.[25] The isotherm is measured using the successive compression technique, in which the monolayer is allowed to relax for 15 minutes after each compression.

4.5 Results

Figure 4.5 shows a measured isotherm for triglyceride at 25 °C. At low densities the monolayer undergoes a first order phase transition from the gas phase to the liquid expanded (LE) phase. This phase transition region extends from very low densities up to a molecular number density N of approximately 0.8 nm^{-2}. In this region the monolayer is inhomogeneous. Instead of having uniform density, the monolayer displays a coexistence of the very low density gas phase and the higher density LE phase. The Brewster angle microscope allows the examination of the morphology of the LE phase in this coexistence region. The pictures at the bottom of Fig. 4.5 illustrate the appearance of the monolayer in the G/LE coexistence region; the dark regions in the pictures are the low density gas phase, while the brighter regions are the higher density liquid expanded phase. The LE phase forms an interconnected two dimensional foam structure with bubbles of gas phase separated by regions of LE phase. The fraction of the surface which is covered by the LE phase (the 'coverage') increases linearly with density until the end of the coexistence region at a molecular number density of 0.8 nm^{-2}, where the entire film is in the LE phase. The surface pressure remains constant for the entire G/LE coexistence region. Upon further increase in density the surface pressure starts to rise, until the monolayer undergoes a transition to the liquid condensed (LC) phase, starting at a molecular number density of 1.15 nm^{-2}.

We analyzed the pictures from the G/LE coexistence region to evaluate how the width of the LE regions changes with increasing coverage. Each picture was thresholded so that the gaseous regions were black and the liquid expanded

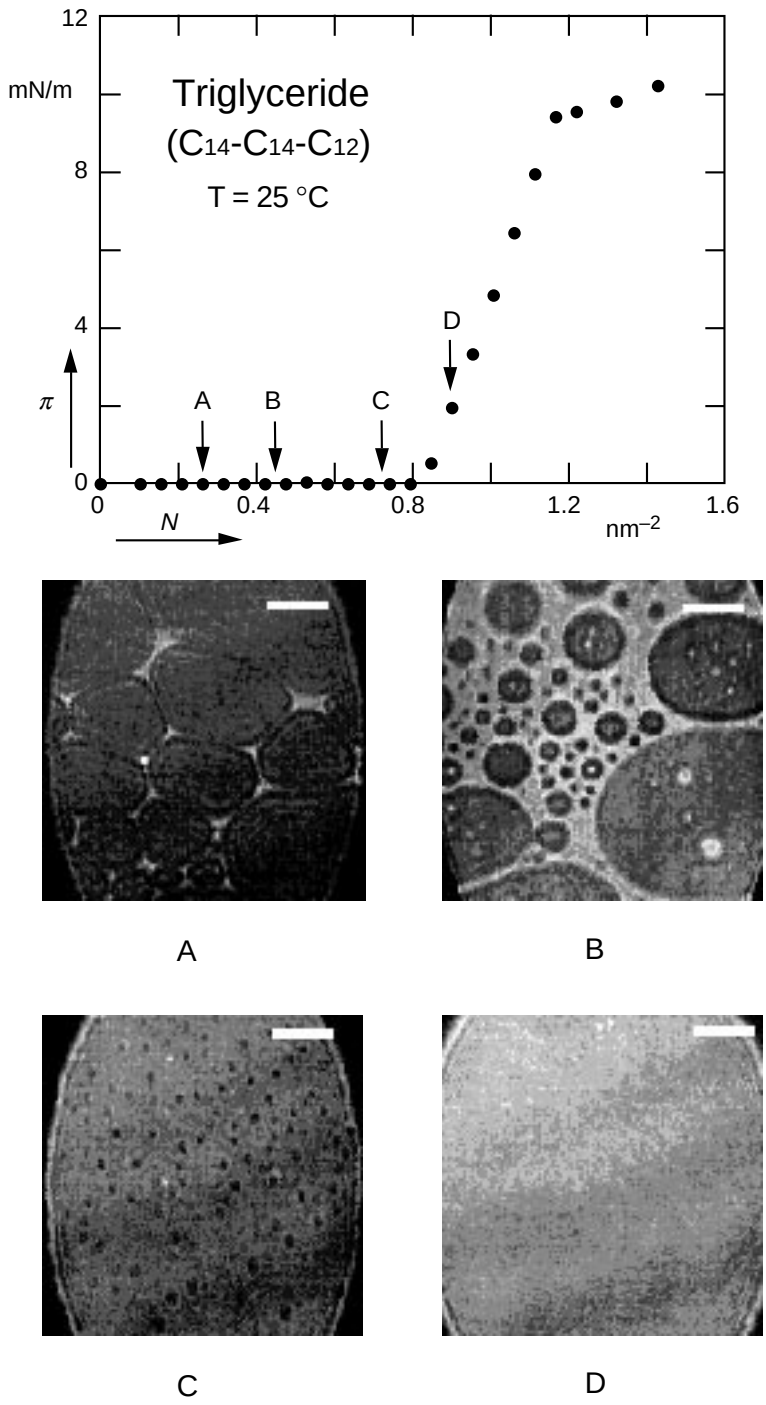

Figure 4.5. Isotherm and morphology of a triglyceride monolayer at 25.0 °C. In the images, taken with a Brewster angle microscope, the light regions correspond to the LE phase and dark regions to the gas phase. The length of the white bars is 200 μm. Images A, B and C are in the G/LE coexistence region, image D in the LE phase.

regions were white. We define the total coverage for an image, *C*, as the fraction of the area which is in the LE phase, and the partial coverage *C'* as the coverage due to LE regions which are larger than a given width *d*. In other words, *C'* is the total area that is contained in LE regions whose widths are greater than the width *d*, divided by the total area of the picture. The method which we use to determine the partial coverage due to LE regions of width *d* is as follows. Starting in horizontal rows from the upper right hand corner of the picture, we count how many consecutive white pixels there are before encountering a black pixel. If the length of this white region is longer than the length *d*, then these pixels are counted as contributing to the partial coverage; if the region is shorter than the length *d* then the pixels are counted as if they were black. This process continues until the end of the line, and then continues to the next line. To check for systematic errors, we analyzed each picture by counting both horizontally and vertically.

For a series of images taken at various molecular densities we measured the total coverage, as well as the partial coverage due to regions wider than 70, 160 and 300 μm. Figure 4.6 shows a plot of how the partial coverage due to regions of these widths varies as a function of the total coverage in the picture. Open circles correspond to the results obtained by counting horizontally, and closed circles by counting vertically. Within experimental error, the two directions give equivalent results. Pictures with total coverage below 0.3 have a partial coverage of less than 0.1 from regions larger than 70 μm. Pictures with coverage up to 0.6 have regions which are wider than 70 μm, but they still have a partial coverage of less than 0.1 from regions larger than 160 μm. At still greater coverage more regions larger than

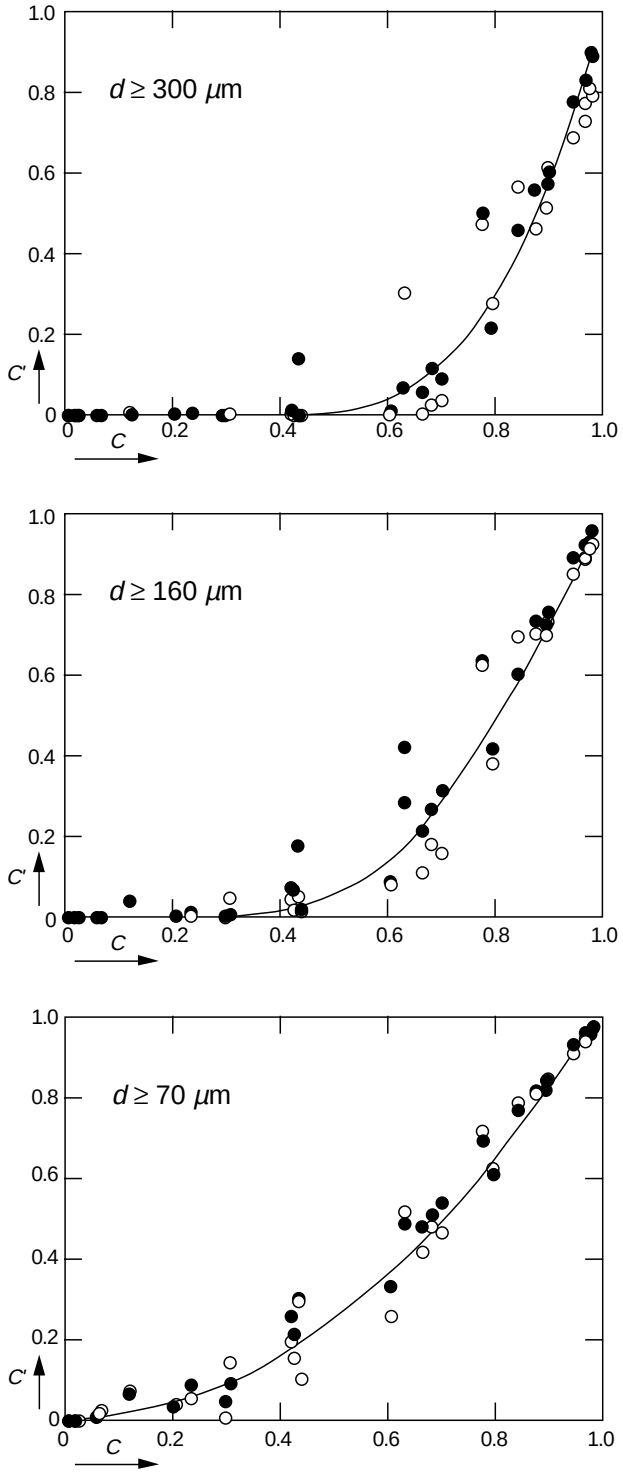

Figure 4.6. Partial coverage C' (i.e. the fraction of an image covered by LE regions larger than a certain size d) for d = 70, 160 and 300 μm as a function of total coverage C. Open and closed circles correspond to row-by-row and column-by-column analysis of the Brewster angle microscope images, respectively. The curves are guides to the eye.

160 μm start to appear, but only at very high coverages (>0.75) does the partial coverage from regions larger than 300 μm exceed 0.1.

Monolayers in the G/LE coexistence region show large scale inhomogeneity; the total coverage measured in a single microscope picture may be very different from the average coverage in the entire monolayer. For any monolayer density in the coexistence region there may be pictures for which almost the entire monolayer in the field of view is in the gas phase or in the liquid expanded phase. This is because the BAM samples only a small area relative to the size of the trough. However, when the monolayer has a low density, only a very small fraction of the surface can have locally high coverage, and near the end of the coexistence region only a small fraction of the surface can display low coverage. On the whole, a monolayer with a given density can be characterized by its average coverage. Therefore, at low densities, where the coverage is low, we expect that there will be few LE regions larger than 70μm, and that regions greater than 70, 160 and 300 μm will not appear until the average coverage exceeds 0.3, 0.6 and 0.75 respectively, which correspond to molecular number densities of 0.25, 0.5 and 0.6 nm^{-2}.

The light scattering measurements were carried out at capillary wave wavelengths of λ = 73, 162 and 304 μm. For all measurements the temperature was kept at 25.0 °C. Figure 4.7 shows the damping constants of the capillary waves as a function of molecular density. At 25 °C, the monolayer is in the G/LE coexistence region when the molecular number density is below 0.8 nm^{-2}. When the molecular number density is above 0.8 nm^{-2}, the monolayer is in the pure LE phase, where the monolayer is homogeneous. For each wavevector, the damping constant at zero

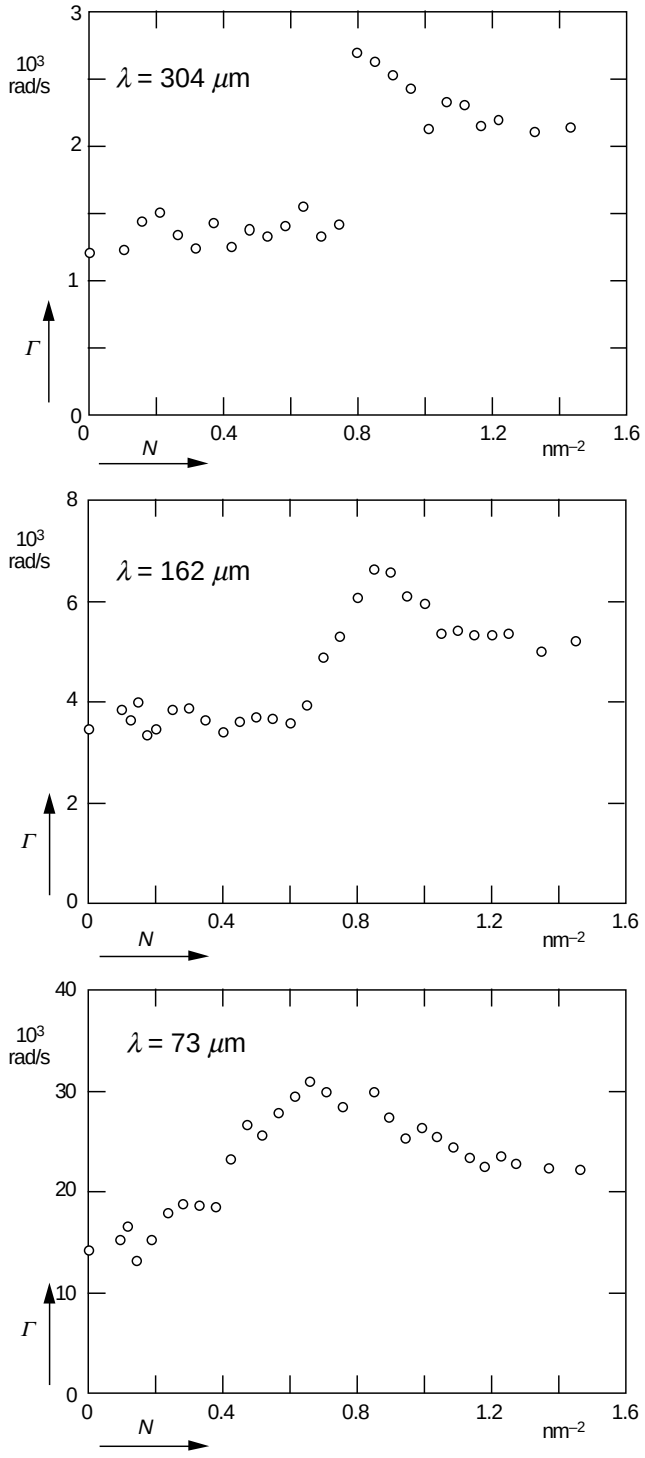

Figure 4.7. Temporal capillary wave damping constant as a function of monolayer density for three capillary wavelengths. Below 0.8 nm^{-2} the monolayer is in the G/LE coexistence region; at higher densities the monolayer is in the pure LE phase.

density corresponds to the value for a clean water surface. For λ = 304 μm, the damping constant stays the same as the damping constant for a clean water surface in the entire G/LE coexistence region, and then jumps by a factor of two at the end of the coexistence region. When the wavelength is reduced to 162 μm, the damping constant shows a different behavior. It starts to increase at a molecular number density of approximately 0.6 nm^{-2} and then increases linearly. Again, the damping constant reaches its maximum value at the end of the coexistence region. Further reducing the wavelength to 73 μm shifts the point at which the damping constant begins to rise to lower molecular density (0.4 nm^{-2}). The damping constant for this wavelength, too, increases linearly with the molecular density and peaks near the end of the coexistence region. For all three wavelengths the damping constant decreases after reaching its maximum value.

4.6 Discussion

The effect of a monolayer on capillary wave propagation has been described by Lucassen for the case of a homogeneous monolayer in terms of the trajectories of the fluid elements at the water surface (see Fig. 4.8).[11] For a clean water surface, the horizontal and vertical motion of the fluid elements have equal amplitudes and a phase difference of 90°. The fluid elements therefore move in circular orbits. If the surface is covered by a monolayer, the motion of the top liquid layer is affected by surface stresses. Both the dilational and shear elasticity of the monolayer contribute to stress at the surface. The dilational elasticity is related to the stress caused by the compression and expansion of the monolayer, while the shear elasticity is related to the stress caused by changing the monolayer shape. The in-

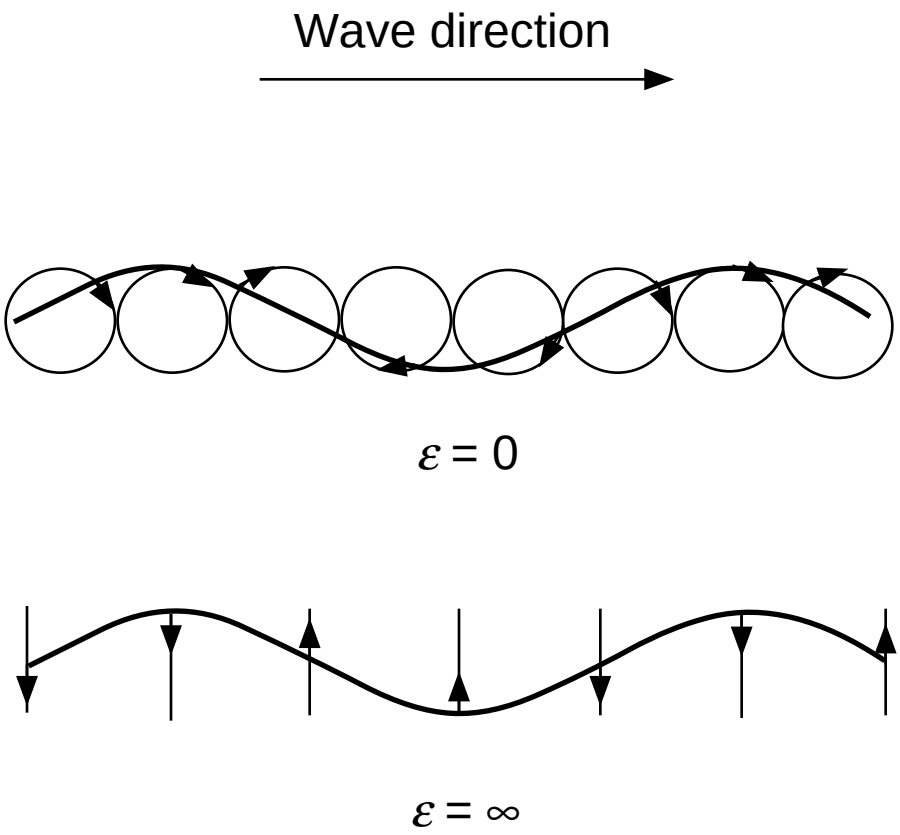

Figure 4.8. Trajectories of surface particles in capillary wave motion. For a clean water surface the surface dilational modulus ε is zero, and trajectory is circular. When $\varepsilon = \infty$, the monolayer is solid and there is no horizontal motion of the surface particles.

plane shear elasticity is very small for liquid expanded monolayers, and can be ignored.[7] Increasing the dilational elasticity of the surface leads to a change in the phase difference between the horizontal and vertical surface displacements. For very high dilational elasticity there is no horizontal motion, and the fluid elements move straight up and down. These changes in the particle motion increase the velocity gradients at the surface as compared to the gradients for a clean water surface. Because of the shear viscosity of water, these large velocity gradients result in a higher damping of the capillary waves.

The static dilational elasticity of the monolayer (i.e. the monolayer's response to an infinitely slow change in area) can be obtained from the isotherm according to the relation[7]

$$\varepsilon = -d\pi / d(\ln A) \tag{4.4}$$

where ρ is the surface pressure of the monolayer and A is the area per molecule ($A \equiv 1/N$). In the G/LE coexistence region, the surface pressure of the monolayer is constant (see Fig. 4.5). According to Eq. 4.4, the static dilational elasticity of the monolayer is therefore zero. With zero dilational elasticity, the monolayer should have no effect on capillary wave propagation, and therefore the damping of the capillary wave should be the same as that for a clean water surface. However, the results for λ = 73 and 162 μm in Fig. 4.7 show a clear increase in damping in the G/LE coexistence region where the static dilational elasticity is zero. We attribute this observed increase in damping to an increase in the dynamic dilational elasticity (*i.e.*, the dilational elasticity at the capillary wave frequency).

The physical origin of the dynamic dilational elasticity can be understood in terms of an interplay between the width d of the LE regions and the capillary wavelength. Figure 4.9 shows the horizontal displacements of the surface particles in a single LE region during wave motion. If the width of the LE region is much smaller than the capillary wavelength, all of the particles in the region move in the same direction. The entire region moves with the wave and oscillates back and forth at the wave frequency. Since all the particles in the region move together, the strain in the region is zero and no stress is applied to the surface particles. Therefore, the surface particles move in the same way as for a clean water surface

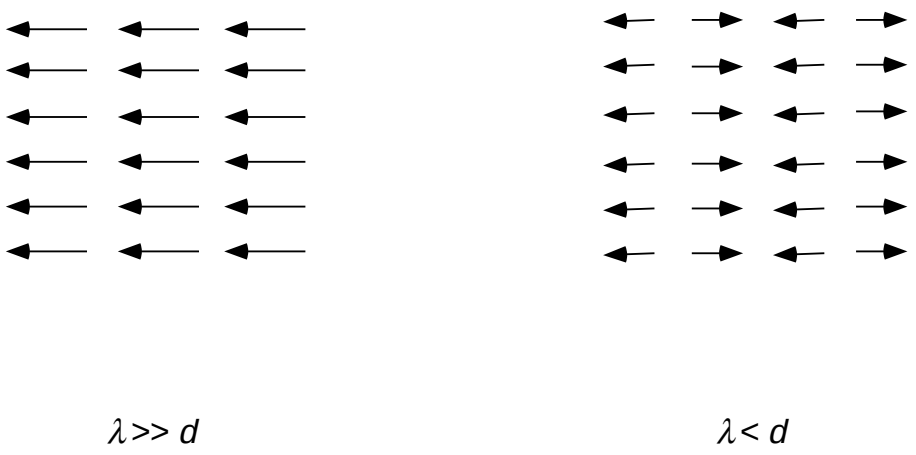

Figure 4.9. Horizontal displacements of the surface particles in a single LE region. When the wavelength is greater than the width of the LE region, all surface particles are displaced in the same direction. When the wavelength is smaller than the width of the LE region, some of the surface particles move in one direction and some in the opposite direction.

and the LE region has no effect on the wave damping. If the width of the LE region is greater than the wavelength, however, some of the particles within the region move along the wave direction and some move in the opposite direction. Because of the displacement of the surface particles in opposite direction, a strain is generated which applies a dilational stress to the surface particles. This stress reduces the horizontal motion of the surface particles and increases the wave damping.

The combination of the light scattering and the Brewster angle microscopy illustrates the effect of the width of the LE regions on the capillary wave damping. As can be seen in Fig. 4.7, the damping constant at the wavelength λ = 162 μm does not change until the molecular number density is 0.6 nm^{-2}. If the LE regions do not affect the capillary wave damping until the regions are larger than the capillary wavelength then this implies that at this density and above there are an

appreciable number of LE regions larger than or equal to 162 μm. For λ = 73 μm, the damping constant starts to increase at about 0.2 nm^{-2}, indicating that at this density regions larger than or equal to 73 μm begin to appear in noticeable quantity. The BAM measurements show how the coverage due to regions of a certain width changes as a function of the total coverage, and therefore density (Fig. 4.6). As we can see, the results from the damping measurements match well with the BAM measurements for these two wavelengths. Only for λ = 304 μm does the damping constant not show a rise until the end of the coexistence region, even though the BAM data imply that it should begin to rise just before the end of the coexistence region. This is most likely due to variations in the monolayer morphology. Figure 4.7 shows that for the two shorter wavelengths, after the damping constant begins to rise it increases linearly with the monolayer density until it reaches a maximum value at 0.8 nm^{-2}. We believe that this linear increase is due to an approximately linear increase in the amount of coverage from regions that are larger than or equal to the wavelength.

4.7 Conclusions

We studied the effects of an inhomogeneous monolayer at the air/water interface on the damping of capillary waves. We found that in the G/LE coexistence region, the monolayer morphology has a strong effect on the capillary wave damping. Light scattering measurements, combined with the analysis of pictures taken with a Brewster angle microscope, show that the damping constant of the capillary wave increases from its value for a clean water surface only when the capillary wavelength is smaller than the width of the LE regions. If the capillary

wavelength is greater than the width of the LE regions, the monolayer has no measurable effect on the capillary wave damping. The results also indicate that while the static dilational elasticity of the monolayer is still zero in the G/LE coexistence region, the dynamic dilational elasticity of the monolayer is not zero.

References

[1] P. Dutta, J. B. Peng, B. Lin, *et al.*, Phys. Rev. Lett. **58**, 2228 (1987).

[2] K. Kjaer, J. Als-Nielsen, C. A. Helm, *et al.*, J. Phys. Chem. **93**, 3200 (1989).

[3] T. Rasing, Y. R. Shen, M. W. Kim, *et al.*, Phys. Rev. Lett. **55**, 2903 (1985).

[4] C. M. Knobler, Adv. Chem. Phys. **72**, 397 (1990).

[5] H. M. McConnell, Annu. Rev. Phys. Chem. **42**, 171 (1991).

[6] D. Langevin, J. Coll. Inter. Sci. **80**, 412 (1981).

[7] J. C. Earnshaw, R. C. McGivern, and P. J. Winch, J. Phys. France **49**, 1271 (1988).

[8] Q. Jiang, Y. C. Chiew, and J. E. Valentini, Langmuir **8**, 2747 (1992).

[9] K. Y. Lee, T. Chou, D. S. Chung, *et al.*, J. Phys. Chem. **97**, 12876 (1993).

[10] K. Miyano and K. Tamada, Langmuir **9**, 508 (1993).

[11] E. H. Lucassen-Reynders and J. Lucassen, Adv. Colloid Interface Sci. **2**, 347 (1969).

[12] M. Lösche and H. Möhwald, Rev. Sci. Instrum. **55**, 1968 (1984).

[13] D. Honig and D. Mobius, J. Phys. Chem. **95**, 4590 (1991).

[14] S. Henon and J. Meunier, Rev. Sci. Instrum. **62**, 936 (1991).

[15] K. Miyano and K. Tamada, Langmuir **8**, 160 (1992).

[16] D. Langevin, J. Meunier, and D. Chatenay, in *Surfactants in Solution*, edited by K. L. Mittal and B. Lindman (Plenum Press, New York, 1984), Vol. 3, p. 1991.

[17] R. C. McGivern and J. C. Earnshaw, Langmuir **5**, 545 (1989).

[18] Q. Jiang and Y. C. Chiew, Langmuir **9**, 273 (1993).

[19] T. Chou and D. R. Nelson, J. Chem. Phys. **101**, 9022 (1994).

[20] E. Mazur and D. S. Chung, Physica **147A**, 387 (1987).

[21] A. Braslau, P. S. Pershan, G. Swislow, *et al.*, Phys. Rev. A **38**, 2457 (1988).

[22] J. Puerta and P. Martin, Appl. Opt. **20**, 3923 (1981).

[23] D. Fahey and D. M. Small, Langmuir **4**, 589 (1987).

[24] D. R. Merker and B. F. Daubert, J. Phys. Chem. **86**, 1009 (1964).

[25] G. L. Gaines Jr., *Insoluble monolayers at liquid-gas interfaces* (John Wiley & Sons, Inc., 1966).

Chapter 5

Quantitative Measurement of Molecular Tilt Using Brewster Angle Microscopy

In Chapter 3 we discussed the use of depolarized Brewster angle microscopy for imaging the quasi-long-range order in molecular tilt displayed in some monolayer phases. In this chapter we expand on that technique, using a series of Brewster angle microscope images to find the tilt angle of the molecules from the surface normal. The validity of this technique is demonstrated through the investigation of a system that has been well characterized using x-ray scattering measurements. In addition, we measure the transition from a tilted to an untilted phase in a monolayer of a long-chain alcohol.

5.1 Introduction

Monolayers of amphiphilic molecules at the air/water interface — Langmuir monolayers — have been extensively studied as model two-dimensional systems.[1-3] One class of molecules that has been the subject of particular attention are long-chain fatty acids and alcohols.[4-11] As a function of temperature and surface pressure monolayers of these long-chain molecules undergo a variety of phase transitions. These systems have been studied with many experimental techniques;[4, 12-14] the most complete information about the microscopic structure of the monolayer comes from grazing-incidence x-ray diffraction measurements.[5-11] Recently Brewster

angle microscopy has been used to study the macroscopic morphology of Langmuir monolayers.[15-20] In this chapter we present a new method for measuring the tilt angle of the monolayer using Brewster angle microscopy.

X-ray diffraction measurements have revealed the microscopic structure of a number of monolayer phases. For example, Fig. 5.1 shows the phase diagram for an equilibrium monolayer of docosanoic (also called behenic) acid ($C_{22}H_{44}O_2$).[11] At high surface pressure and low temperature the monolayer is in an untilted phase (*U*), with the molecules oriented normal to the interface. The remaining phases all have long-range order in the orientation of the molecules and the molecules are tilted from the surface normal by an angle φ. The phase of the monolayer is determined by the tilt angle φ and the direction of the tilt — toward the nearest-neighbor (*I* or *I'*), or the next-nearest-neighbor (*F*). The *I* and *I'* phases differ from each other in their lattice spacing and tilt angle.

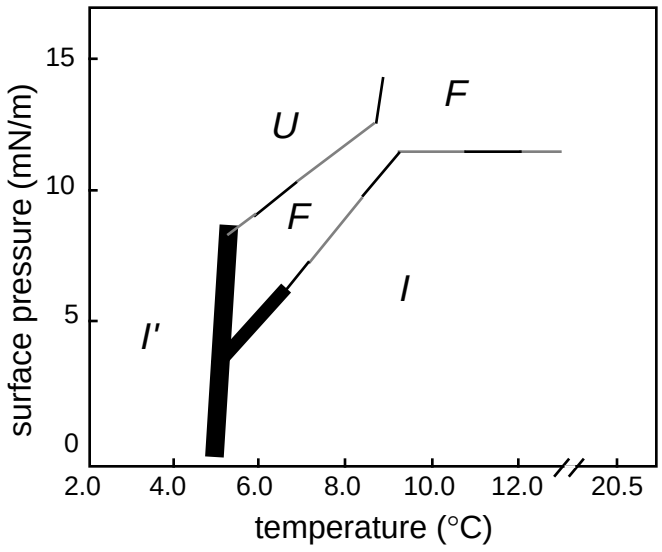

Figure 5.1. Equilibrium phase diagram for behenic acid monolayers, from M. Bommarito, *et al.*[11] The thick lines represent the uncertainty in the phase boundary. The dark thin lines are regions where isotherm measurements were followed across the phase boundary.

Brewster angle microscopy allows the imaging of monolayer inhomogeneities, either in density or in the direction of molecular tilt.[15, 16] The principle of Brewster angle microscopy is illustrated in Fig. 5.2. A *p*-polarized laser beam is incident on a monolayer covered air/water interface at the Brewster angle of water. If no monolayer is present on the interface, no light is reflected. Light that is reflected by the monolayer is imaged onto a CCD camera; an analyzer selects the polarization of the reflected light which is detected. If the monolayer is optically isotropic, the reflected light is *p*-polarized. However, if there is long-range order (on the order of μm) in the orientation of the molecules, the monolayer is optically anisotropic, because the molecules themselves are anisotropic. Because of the anisotropy of the monolayer, the polarization of the reflected light is rotated from *p*-polarized; the exact polarization and intensity of the light depends on the tilt angle

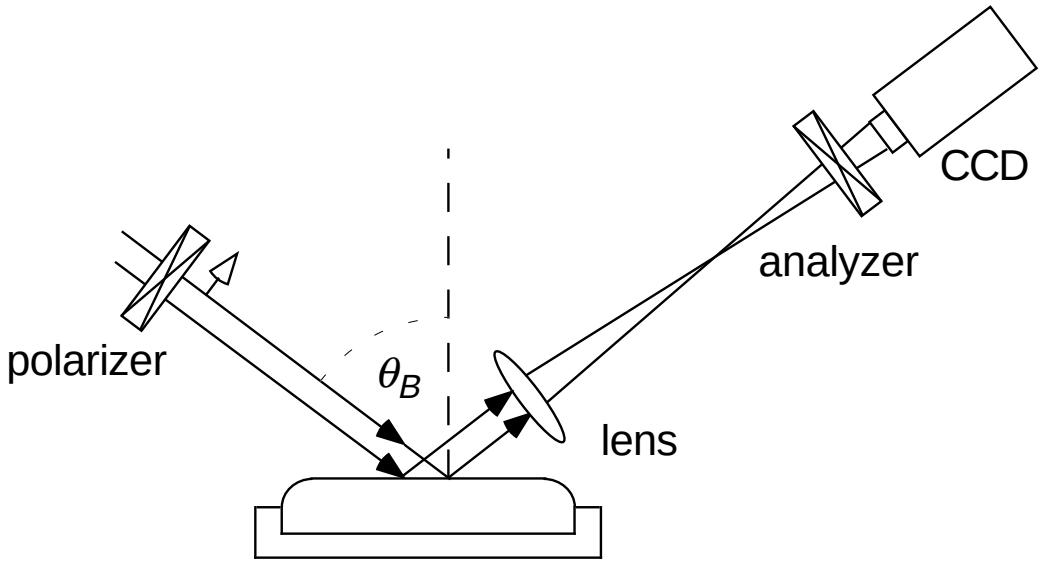

Figure 5.2. Experimental setup for Brewster angle microscopy. A *p*-polarized laser beam is incident on the monolayer covered air/water interface at the Brewster angle θ_B of water. The light reflected by the monolayer is imaged onto a CCD camera. If the monolayer has quasi-long-range order in the molecular tilt, the polarization of the reflected light is rotated from *p*-polarized. The analyzer is used to measure the polarization of the reflected light.

φ, as well as on the orientation of the molecules relative to the incident direction of the light. A Brewster angle microscope image illustrating this principle is shown in Fig. 5.3, which shows the *s*-polarized light reflected from a behenic acid monolayer in the *I* phase. Different intensities in the image correspond to regions with different azimuthal angle (the angle θ that the projection of the molecule onto the interface makes with the direction of the incident light). The bright hexagonal regions in the image are three-dimensional crystallites. These crystallites are discussed in more detail later in this chapter.

The purpose of this chapter is to illustrate how images such as Fig. 5.3 can be used to measure the molecular tilt from the surface normal, φ. The idea behind the technique is that, while the polarization of the light reflected from a single point on the monolayer depends on both the tilt angle and the azimuthal angle of the

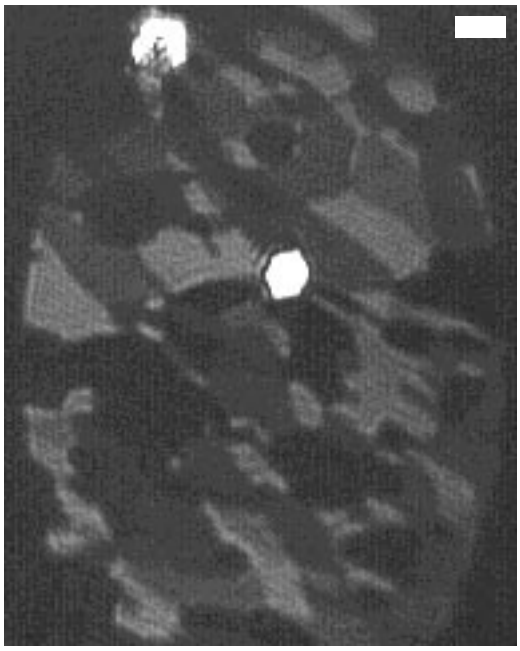

Figure 5.3. Brewster angle microscope image of *s*-polarized light reflected by behenic acid in the *I* phase. The bright hexagonal regions are three-dimensional crystallites. The white bar represents 100 μm.

molecules at that point, the range of polarizations reflected by the entire monolayer, which includes regions with all azimuthal angles, depends only on the tilt angle φ and the optical anisotropy of the molecules. The validity of this technique is demonstrated by comparing measurements of the tilt angle of behenic acid and heneicosanol ($C_{21}H_{43}OH$) with known values of the molecular tilt from x-ray scattering measurements.[10, 11]

5.2 Experimental details

5.2.1 Langmuir trough

The experiments described in this chapter were performed in a Langmuir trough enclosed in a double walled aluminum box to provide temperature stability and protection from contaminants. The trough is milled from a single piece of black teflon and is attached to a gold-coated copper plate that serves as a temperature-control plate. The black teflon minimizes the scattering of light from the bottom of the trough. A teflon barrier is used to vary the density of the monolayer.

The temperature of the cooling plate and of the aluminum enclosure are controlled with two Neslab closed-cycle systems. To minimize the evaporation of the water subphase, the enclosure is kept approximately 5 °C warmer than the cooling plate. The temperature of the sample is measured with a teflon-coated thermistor inserted directly in the water subphase; the sample temperature is intermediate between those of the temperature-control plate and the enclosure and is stable to within 0.2 °C. The enclosure is encased in foam insulation and is thermally isolated from the table it is mounted on.

To insure the cleanliness of the system, the stepper motor used to move the teflon barrier is housed outside the enclosure, and is coupled to the barrier using a rotational feedthrough designed for vacuum systems. The surface pressure of the sample is measured using the Wilhelmy plate method.[21] The Wilhelmy plate used is made of filter paper, and its displacement is measured with a linear variable differential transformer. The pressure measurement system has a resolution of approximately 0.2 mN/m.

5.2.2 Brewster angle microscope

The Brewster angle microscope used for the experiments described in this chapter is of the type described by Honig and Mobius,[16] *i.e.*, the imaging lens is not scanned to form a focused image for the entire picture. The illumination is provided by an Argon ion laser (incident power ≈ 60 mW), polarized with a Glan-Thompson polarizer. The analyzer is a dichroic sheet polarizer in a manual rotation mount. The reflected light is imaged onto a CCD camera with a 25-mm diameter, 175-mm focal-length lens positioned outside of the aluminum enclosure discussed above. The images are captured on a computer. All of the images in this chapter have their contrast digitally enhanced.

5.2.3 Materials and procedures

The samples (purity > 99%) were used without further purification with chloroform as the solvent. Strict procedures are followed to ensure the cleanliness of the system. The trough is first wiped with acetone and chloroform. It is then soaked in a 50/50 mixture of ultrapure water (Millipore Milli-Q system, R > 18 MΩ/

cm) and sulfuric acid with No-Chromix glass cleaner for a half hour, and then rinsed with ultrapure water.

After the cleaning is completed, the trough is placed in the enclosure and is flushed many times with water. The pH of the ultrapure water used in the experiments is adjusted to 2.0 with hydrochloric acid to minimize the dissociation of the behenic acid head group.The enclosure is filled with 99.999% pure nitrogen gas. Whenever the enclosure is opened (*e.g.*, for the deposition of the sample) pure nitrogen gas is made to flow through the system to keep out contaminants. After the enclosure is sealed, a 1 psi overpressure is maintained inside.

Before the monolayer is deposited, the water surface cleanliness is checked by moving the barrier over the maximum compression ratio of the trough (4/1). If the pressure changes by less than 0.08 mN/m the surface is considered clean enough to deposit the sample. The sample is deposited from a syringe with a teflon tipped piston. The drops at the tip of the syringe are carefully touched to the surface of the water, with special care being taken to insure that the syringe tip does not touch the water surface. After the sample is deposited, the system is allowed to reach equilibrium for approximately 30 minutes.

5.3 Experimental results

5.3.1 Qualitative Brewster angle microscope results

The Brewster angle microscope was used to monitor the morphology of the monolayer after it is spread. The texture of the film after spreading in the *I* phase at zero surface pressure (area/molecule = 0.3 nm^2) is shown in Fig. 5.4. Differences in

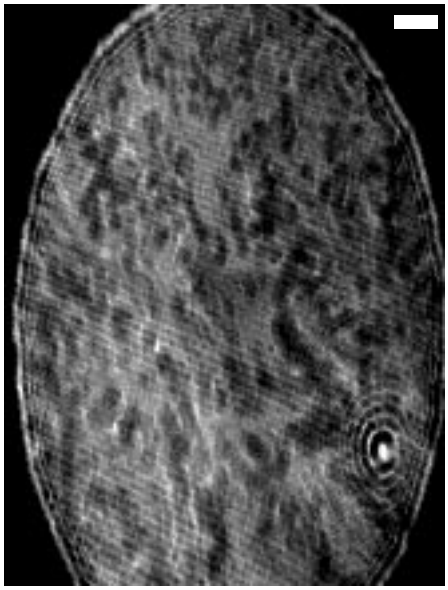

Figure 5.4. Texture of the *I* phase of behenic acid soon after it is spread from solution. The image was taken without an analyzer. Different intensities correspond to regions with different molecular azimuthal angle. The white bar represents 100 μm.

intensity in the image correspond to regions of different molecular azimuthal orientation — the tilt domains are small, but resolvable. The bright spot is a three dimensional crystallite, which is discussed further bellow. Due to temperature gradients in the enclosure, the film drifts slowly in one direction, until at some point a boundary comes into view, separating the film whose texture is shown in Fig. 5.4 from what appears to be a clean water surface — *i.e.*, the monolayer is in a coexistence region between a condensed phase (which exists in very large domains, on the order of centimeters) and a very low density gas phase. The boundary between the two phases is not smooth; rather, there are often visible kinks in the boundary, implying the existence of quasi-long-range positional or bond orientational order in the *I* phase.

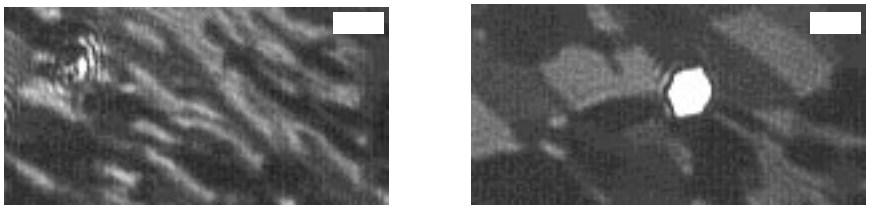

a *b*

Figure 5.5. Texture of the *I* phase of behenic acid at 2 mN/m; the analyzer is set to transmit only *s*-polarized light. Image *a* shows the monolayer soon after compression. Image *b* shows the relaxed monolayer after several hours. The white bars represent 100 μm.

Upon compression, the condensed phase comes back into view while the surface pressure remains at 0 mN/m. The surface pressure begins to rise when the film is compressed to 0.22 nm^2/molecule. If the film is allowed to relax in this region, there is appreciable coarsening of the film texture, as shown in Fig. 5.5. In this region of the isotherm the surface pressure relaxes over a period of tens of minutes after compression.[11] This relaxation may be related to the coarsening phenomenon illustrated in Fig. 5.5.

When the behenic acid monolayer is spread in the *I'* phase at 0.3 nm^2 per molecule, the domain structure of the film, shown in Fig. 5.6, is finer than that of the *I* phase. Just as in the *I* phase the film drifts as a function of time, until the boundary between the film and a clean water interface (or a very dilute gas phase) comes into view. When the film is compressed to finite surface pressure, however, the coarsening of the domains is markedly less than that seen in the *I* phase (compare Fig. 5.6 and Fig. 5.5).

When the monolayer is spread in either the *I* or the *I'* phase there are often small bright spots visible in the picture (see Fig. 5.4). These bright spots, which are

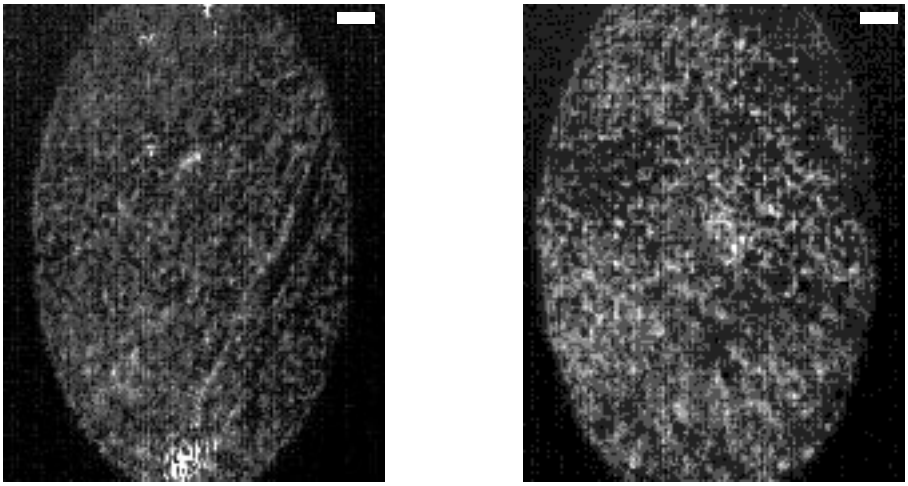

a *b*

Figure 5.6. Texture of the *I′* phase of behenic acid shortly after being spread from solution *a* and after relaxing for several hours *b*. The analyzer is set to transmit *s*-polarized light. The domain structure never coarsens to the same extent as that of the *I* phase. The white bars represent 100 μm.

smaller than the resolution limit of our microscope, are three-dimensional crystallites in the film. In the *I* phase the density of these crystallites increases with time as the film remains uncompressed. If the film is compressed slowly (1.4×10^{-3} nm^2/molecule-hour) these crystallites grow in size; they become clearly resolvable by the microscope as hexagonal crystallites 50-200 μm in width (see Fig. 5.5*b*). If the film is compressed more rapidly (3.0×10^{-3} nm^2/molecule-hour) the crystallites do not grow appreciably either in number or in size. When the monolayer is spread in the *I′* phase, the crystallites do not increase in either number or in size, even for very slow compression rates (3.0×10^{-3} nm^2/molecule-hour).

No crystallites were ever visible for the long chain alcohols which we studied. The appearance of the crystallites appears to be correlated with the behavior of the material when spread from a bulk crystal, rather than from solution. When a bulk crystal of heneicosanol is placed on a clean water surface, a

monolayer with measurable surface pressure (the equilibrium spreading pressure) spreads and exists in equilibrium with the bulk crystal. For the behenic acid, in contrast, there is no measurable equilibrium spreading pressure. It therefore seems that for pressures below the equilibrium spreading pressure, monolayers exist as true equilibrium phases. If there is no equilibrium spreading pressure, however, a monolayer spread from solution is in a metastable state, and will spontaneously nucleate three dimensional crystallites, the true equilibrium phase.

5.3.2 Quantitative Brewster angle microscopy - technique

In a Brewster angle microscope the light incident on the monolayer covered air/water interface is *p*-polarized. If the monolayer is optically isotropic — *e.g.*, if there is no quasi-long-range order in molecular tilt, or if the molecules are untilted — then the reflected light will also be *p*-polarized. However, since the optical polarizability of long chain molecules is anisotropic (it is greater along the chain than across the chain), if there is long-range order (over μm length scales) in the molecular tilt direction the monolayer is optically anisotropic. In that case the polarization of the light reflected from the monolayer is rotated from *p*-polarized; the exact polarization and intensity of the reflected light depends on the optical anisotropy of the monolayer, as well as on the molecular tilt angle from the surface normal and the azimuthal tilt direction.[22]

The dependence of the polarization and intensity of the reflected light on the optical properties of the film can be calculated using a 4×4 matrix method developed by Berreman.[23] We assume that the molecules are cylindrically

symmetric; *i.e.*, that the dielectric tensor, ε_{ij}, in the frame of the molecules is given by

$$\varepsilon_{ij} = \begin{bmatrix} \varepsilon & 0 & 0 \\ 0 & \varepsilon & 0 \\ 0 & 0 & \varepsilon + \Delta \end{bmatrix} \tag{5.1}$$

where the z-axis is parallel to the hydrocarbon chain. In any given domain, the molecules are tilted by an angle φ from the surface normal and the projection of the molecules on the plane of the interface makes an angle θ with the x-axis, where the x-axis is defined by the projection of the direction of propagation of the light on the plane of the interface (see Fig. 5.7). The tilt angle φ is uniform for the entire monolayer; the azimuthal angle θ is uniform over regions on the order of microns.

Using the method of Berreman,[23] we calculate the polarization and intensity of the reflected light for given values of ε, Δ, φ, and θ. Figure 5.8 shows the

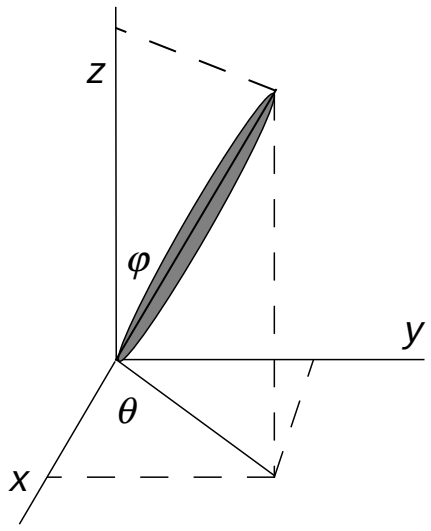

Figure 5.7. Definition of the orientational angles φ and θ. The z-direction is normal to the surface. The xz-plane is the plane of incidence; the light travels in the positive x-direction. The molecule is tilted by an angle φ from the z-axis. the projection of the molecule onto the surface makes an angle θ with the x-axis.

dependence of the polarization of the reflected light on the azimuthal angle θ for three different tilt angles φ, where we have chosen $\varepsilon = 2.09$ and $\Delta = 0.11$. If φ, ε, and Δ are known, measuring the polarization of the reflected light limits the azimuthal angle θ to be one of either two or four values, depending on the tilt angle φ. More importantly for the purpose of this chapter, the maximum rotation of the polarization of the reflected light depends on the tilt angle φ. If ε and Δ are known, measuring the range of polarizations reflected by monolayer domains with different orientations allows one to deduce the tilt angle φ. Conversely, if the tilt angle φ is known from a complementary technique such as x-ray scattering or optical second harmonic generation, measuring the range of polarizations reflected by the monolayer yields some information about ε and Δ.

As was evident in the images shown earlier (see Fig. 5.4 and Fig. 5.5) each image contains many domains; the azimuthal angle θ changes from domain to

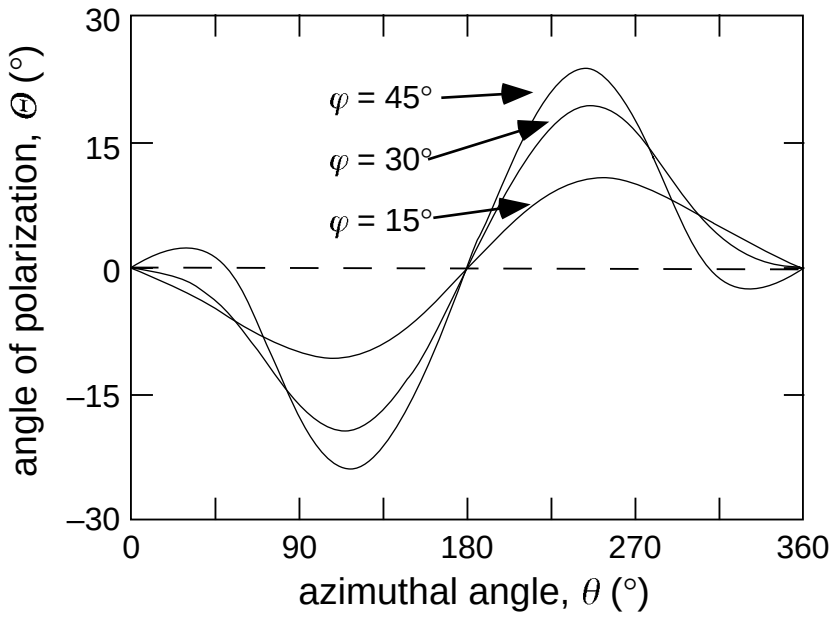

Figure 5.8. Dependence of the angle of polarization of the reflected light (*p*-polarized = 0°) as a function of azimuthal angle for three different tilt angles.

domain. Therefore, measuring the range of polarizations in a single image gives a good estimate of the range of polarizations reflected by the monolayer. We measure the range of polarizations in an image as follows. For each image we take a series of 19 pictures. Between successive pictures we manually rotate the analyzer by 10°. Several adjacent points in each image are averaged together to reduce the effect of video and digitization noise. The intensity I at each point as a function of the analyzer angle α is then fit with a function of the form

$$I = a\,[\cos(b - \alpha)]^2 + c \tag{5.2}$$

where a is the intensity of the reflected light, b is the angle of polarization (0° = *p*-polarized), and c accounts for any constant background. The range of measured polarizations can be used to estimate the tilt angle φ of the monolayer. In this chapter when we refer to the "range of polarizations measured", we use the range which includes 95% of the polarizations in an image.

Just as the range of polarizations reflected from the film depends on the tilt angle φ, so too the range of intensities reflected by the film depends on φ. It is therefore possible in theory to determine the tilt angle φ simply by measuring the range of intensities reflected by the monolayer, which does not require either the use of an analyzer, or the polarization analysis described above. A similar technique, the measurement of the range of intensities of the reflected light transmitted through an analyzed oriented at 45° to *p*-polarized is described by Hosoi, *et al.*[17] However, in addition to being more sensitive to video noise, the use of a coherent light source for the sample illumination (*i.e.*, a laser) results in an interference pattern being superimposed over the measured image. Therefore, even

if there is no range of intensities in the light reflected from the monolayer (*e.g.*, if the molecules are untilted), there is still a range of intensities due to this interference pattern. In addition, measuring the range of intensities in the image requires careful correction for the intensity profile of the illuminating laser. For these reasons we have chosen to measure the range of reflected polarizations rather than the range of reflected intensities to calculate the tilt angle of the monolayer.

The method described above, measuring the range of reflected polarizations by fitting the intensity at each point in the image with a function of the form of Eq. 5.2, is very robust with respect to noise. We have run simulations to gauge the effect that video or digitization noise has on the range of the polarizations measured. From the mean square error in our fits, we estimate that the noise in our data corresponds to approximately 20% of the signal level. However, this 20% noise level results in only a slight broadening of the measured range of polarizations. Fig. 5.9 shows the results of the simulations, where we have assumed a 20% noise level, and a 0.2° error in setting the polarizer each time it is rotated. The noise has the largest effect when the intrinsic width of polarizations reflected from the surface is 0° (*i.e.*, when the monolayer is in an untilted phase). The effect of the noise is to broaden the signal to an apparent width of $y_0 = 4.4°$. For tilted monolayer phases, where the monolayer reflects some range of polarizations, the instrumental broadening (*i.e.*, the additional width due to the introduction of noise) becomes relatively unimportant. The dashed line in Fig. 5.9 is the curve $y = \sqrt{x^2 + y_0^2}$; this curve gives a good estimate of the instrumental broadening. Therefore, given a

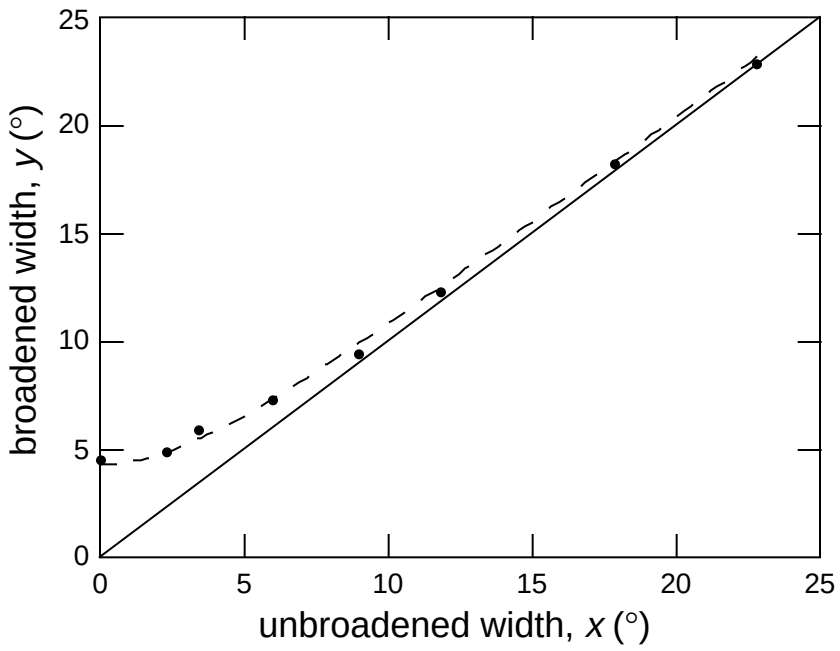

Figure 5.9. Computer simulation of the effect of a 20% noise level on the measured range of polarizations. The solid line represents the ideal case of no instrumental broadening. The meaning of the dashed line is discussed in the text.

measured range of polarizations y, we can estimate that the true range of polarizations reflected from the monolayer is $x = \sqrt{y^2 - y_0^2}$.

5.3.3 Quantitative Brewster angle microscopy - results

If the tilt angle of the molecules from the surface normal is known from another technique, such as x-ray diffraction, the range of polarizations reflected by the monolayer can be used to estimate the optical anisotropy of the molecules. We measured the range of polarizations reflected from a monolayer of behenic acid spread in the *I* phase at 14.4 °C and zero surface pressure to be 40±5°. From x-ray measurements it is known that the tilt angle of the molecules under these conditions is 33°.[11] Obviously, this one piece of information is not sufficient to determine the values of both ε and Δ; however, it does define a curve of values for

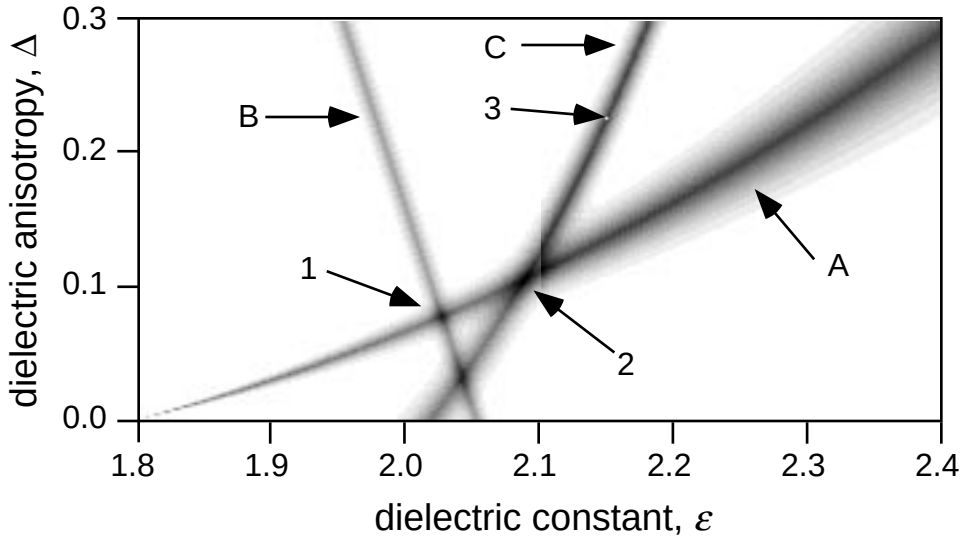

Figure 5.10. Deduction of the values of ε and Δ from the measurement of the range of polarizations reflected by a behenic acid monolayer in the *I* phase. Curve *a* shows the values consistent with the measured range of polarizations — the gray area represents the range of values consistent with the data within the experimental error. Curve *b* shows the values consistent with a monolayer whose average dielectric constant equals that of bulk behenic acid. Curve *c* represents the values consistent with the ellipsometric data of Paudler, *et al.*[14]

ε and Δ which are consistent with the measurement. This curve is shown as curve *a* in Fig. 5.10, where the length of the behenic acid molecule is taken to be 2.75 nm. Because of experimental error, a range of values for ε and Δ are consistent with the measured range of intensities; this range is represented by the width of curve *a*.

Another piece of information is necessary to deduce a single value of ε and Δ. One possible choice is to require that the average dielectric constant of the monolayer, $\bar{\varepsilon} = \frac{3\varepsilon + \Delta}{3}$, be equal to the dielectric constant of bulk behenic acid. Curve *b* in Fig. 5.10 represents this condition; point 1 ($\varepsilon = 2.03$, $\Delta = 0.08$), the intersection of curves *a* and *b*, yields one estimate for the values of ε and Δ. However, this is not a reliable condition to place on the dielectric constant of the

monolayer, since the density of a monolayer of behenic acid in the *I* phase is approximately 20% greater than that of bulk behenic acid.

Paudler, *et al.*[14] studied the optical anisotropy of Langmuir monolayers of behenic acid using multiple angle ellipsometry. The ellipsometric data alone can not determine both ε and Δ; rather, it defines a curve of allowed ε and Δ, which is shown in Fig. 5.10 as curve *c*. Point 2 ($\varepsilon = 2.09$, $\Delta = 0.11$), the intersection of curves *a* and *c*, is a good estimate of the optical anisotropy. Paudler, *et al.*[14] tried to determine the value of the optical anisotropy by measuring the change in the ellipsometric data as the monolayer undergoes a phase transition between two untilted phases, which (using the Stenhagen notation) they refer to as S and CS. The values which they derive for the anisotropy of the S phase, $\varepsilon = 2.16$, $\Delta = 0.21$, are indicated as point 3 in Fig. 5.10. As is evident from the distance of point 3 from curve (A), this estimate is not consistent with our experimental data.

We have carried out measurements using the technique described above on behenic acid, docosanol ($C_{22}H_{45}OH$), and heneicosanol. The results of some of these measurements, together with the values of the molecular tilt as measured with x-ray diffraction, are shown in Table 5.1. There are several important features of the table. The first is that the tilt angle calculated using the method described in this chapter is in good agreement with the values measured using x-ray diffraction. The one case with a significant difference, the *I′* phase of behenic acid, illustrates a limitation of our technique; as shown in Fig. 5.6, the domains in the *I′* phase of Behenic acid are very small — comparable to the resolution limit of the microscope. Therefore, the light at each point in the image is actually a mixture of

Material and Phase	Tilt angle (°) from x-ray studies	Range of reflected polarizations (°)	Calculated tilt using $\varepsilon = 2.09$ $\Delta = 0.11$	Calculated tilt using $\varepsilon = 2.03$ $\Delta = 0.08$
Behenic acid *I* phase (14.4 °C) 0 mN/m	33[a]	40±5	32±5	33±6
Behenic acid *I′* phase (2.1 °C) 0 mN/m	25[a]	20±5	14±4	15±4
Heneicosanol *F* phase (25 °C) 15 mN/m	8[b]	10±1	7±1	7±1
Heneicosanol *U* phase (25 °C) 18 mN/m	0[b]	4	0	0
Docosanol *F* phase (15.8 °C) 20 mN/m		15±5	11±4	11±4
Docosanol *U* phase (15.8 °C) 23 mN/m		4±1	0	0

Table 5.1. Measurements of the tilt angle of monolayers of several long-chain molecules using the range of polarizations reflected by the monolayer. The calculations assume a monolayer thickness of 2.75 nm for behenic acid and docosanol and 2.6 nm for heneicosanol. We have assumed that the dielectric anisotropy is the same for all of the substances. Calculated tilts of 0° have a potential error of 3°.

a. From Bommarito, *et al.*[11]
b. From Shih, *et al.*[10]

the light from several adjacent domains. The net result is to “dilute” the domains whose polarizations are near the edge of the range reflected by the monolayer, thereby narrowing the measured range of polarizations from its true value. As long as the domains are large enough to be resolved by the microscope, however, our technique yields a reliable estimate of the molecular tilt.

A second important result highlighted in the table is the near equivalence of the last two columns. Finding the exact value for ε and Δ is not crucial, as long as the values that are used for the calculation of the molecular tilt fall on the line defined by curve *a* in Fig. 5.10. Therefore, the technique developed in this chapter can be used whenever the tilt domains are large enough to be clearly resolved by the Brewster angle microscope and the molecular tilt is known for a single reference point.

5.3.4 Application — a detailed study of molecular tilt in heneicosanol monolayers

The technique detailed in this chapter has been used to study the behavior of heneicosanol in detail. In contrast to behenic acid (see Fig. 5.1), heneicosanol has only one tilted phase, an *F* phase; there may be two untilted phases *U* and *U'*

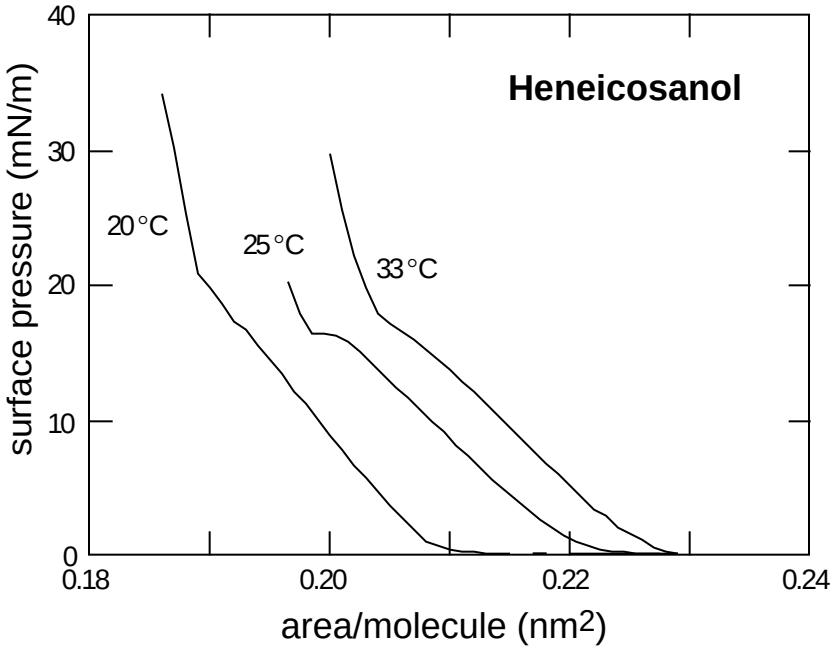

Figure 5.11. Isotherms of heneicosanol. The process of monolayer deposition introduces a 10% uncertainty in the area per molecule. The 25 °C isotherm is shifted right by 7.5×10^{-3} nm^2.

(corresponding to S and CS, respectively in the Stenhagen notation).[10] Figure 5.11 shows the measured isotherms; at 20 °C there is a second-order phase transition from the *F* phase to an untilted phase. When the temperature is raised to 25 °C the transition becomes first-order, as is evidenced by the plateau in the isotherm at a surface pressure of approximately 16 mN/m. At higher temperatures the transition becomes second-order once again, as is evident in the 33 °C isotherm.

The results of our measurements of the molecular tilt of heneicosanol are shown in Fig. 5.12. X-ray measurements[10] show that the zero-pressure tilt for all of these temperatures is 18±1°. While this is consistent with our measurement at 33 °C, our measurements at other temperatures deviate somewhat from this value.

One striking feature of Figure 5.12 is that the tilt angle is approximately independent of the temperature over a wide range of surface pressures. In contrast,

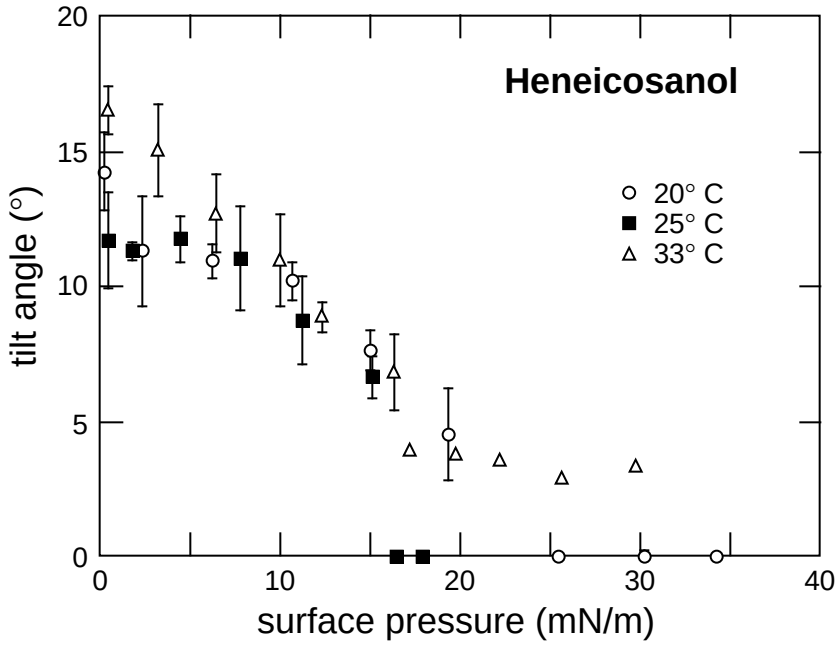

Figure 5.12. Measured molecular tilt for heneicosanol monolayers. The measurements of 0° have a potential error of 3°.

x-ray measurements of behenic acic show some temperature dependence.[11] Two further features of Fig. 5.12 bear mention. The first is that, as expected, the tilt angle is a continuous function of surface pressure at the two temperatures where the transition is second-order. At 25 °C the tilt angle drops abruptly to zero at the first-order transition pressure. The second feature is that while the tilt angle goes to zero at 20 °C and 25 °C, there appears to be a small residual tilt in the “untilted” phase at 33 °C. This small tilt (approximately 4°) is not inconsistent with the x-ray data.[7] This distinction between the high pressure behavior at low temperatures and at high temperatures is consistent with the existence of two distinct untilted phases in heneicosanol.

5.4 Conclusion

We have demonstrated a new technique using Brewster angle microscopy to measure the molecular tilt in Langmuir monolayers. By comparing our results to those from x-ray diffraction measurements, we validated this technique for monolayers whose domains can be resolved by the microscope. If the dielectric anisotropy of the monolayer molecules is known, or if the measurement can be calibrated with a single known value of the tilt, the tilt can be easily measured over a wide range of surface pressures and temperatures. We have demonstrated this by measuring the tilt behavior of heneicosanol over a range of surface pressures for three temperatures. We find that the technique is quite sensitive to even small residual tilt (of order 4°) in the untilted phase of long-chain molecules.

References

[1] G. L. Gaines Jr., *Insoluble monolayers at liquid-gas interfaces* (John Wiley & Sons, Inc., 1966).

[2] W. D. Harkins and E. Boyd, J. Phys. Chem. **45**, 20 (1941).

[3] I. Langmuir, J. Am. Chem. Soc. **39**, 1848 (1917).

[4] J. T. Buontempo and S. A. Rice, J. Chem. Phys. **98**, 5835 (1993).

[5] P. Tippmann-Krayer and H. Möhwald, Langmuir **7**, 2303 (1991).

[6] K. Kjaer, J. Als-Nielsen, C. A. Helm, *et al.*, J. Phys. Chem. **93**, 3200 (1989).

[7] T. M. Bohanon, B. Lin, M. C. Shih, *et al.*, Phys. Rev. B **41**, 4846 (1990).

[8] R. M. Kenn, C. Böhm, A. M. Bibo, *et al.*, J. Phys. Chem. **95**, 2092 (1991).

[9] B. Lin, J. B. Peng, J. B. Ketterson, *et al.*, J. Chem. Phys. **90**, 2393 (1989).

[10] M. C. Shih, T. M. Bohanon, and J. M. Mikrut, J. Chem. Phys. **97**, 4485 (1992).

[11] G. M. Bommarito, W. J. Foster, P. S. Pershan, *et al.*, J. Chem. Phys. **105**, 5265 (1996).

[12] G. A. Overbeck and D. Möbius, J. Phys. Chem. **97**, 7999 (1993).

[13] C. M. Knobler, Adv. Chem. Phys. **72**, 397 (1990).

[14] M. Paudler, J. Ruths, and H. Riegler, Langmuir **8**, 184 (1992).

[15] S. Henon and J. Meunier, Rev. Sci. Instrum. **62**, 936 (1991).

[16] D. Honig and D. Mobius, J. Phys. Chem. **95**, 4590 (1991).

[17] K. Hosoi, T. Ishikawa, A. Tomioka, *et al.*, Jpn. J. Appl. Phys. Pt. 2 **32**, L135 (1993).

[18] G. Overbeck, D. Hönig, and D. Möbius, Langmuir **9**, 7999 (1993).

[19] Y. Tabe and H. Yokoyama, Journal of the Physical Society of Japan **63**, 2472 (1994).

[20] Q. Wang, A. Feder, and E. Mazur, J. Phys. Chem. **98**, 12720 (1994).

[21] G. L. Gaines, J. Coll. Int. Sci. **62**, 191 (1977).

[22] Y. Tabe and H. Yokoyama, Langmuir **11**, 699 (1995).

[23] D. W. Berreman, J. Opt. Soc. Am. **62**, 502 (1972).

Chapter 6

Orientational Fluctuations in a Two-Dimensional Smectic-*C* Liquid Crystal with Variable Density

One of the prime motivations for studying Langmuir monolayers is their usefulness as an experimentally accessible realization of a two-dimensional system. This chapter describes an experiment that was designed to test a specific theoretical prediction for two-dimensional systems, namely the functional form of temporal correlations in the orientational fluctuations of a two-dimensional liquid crystal. In addition, the experiment determines the dependence of the monolayer's orientational viscosity and elasticity on density — the first measurement of these properties as a function of density in a liquid crystal system.

6.1 Introduction

Thermodynamic phases can be characterized by their symmetry;[1] for example, the liquid and gas phases are both isotropic, and therefore have the highest possible symmetry, *i.e.*, continuous rotational and translational symmetry. Crystalline solid phases have low symmetry — the continuous translational and rotational symmetry are lost, replaced by discrete translational and rotational symmetry.

Liquid crystals are materials whose symmetry is intermediate between that of a liquid and that of a solid.[1] For example, consider the substance composed of

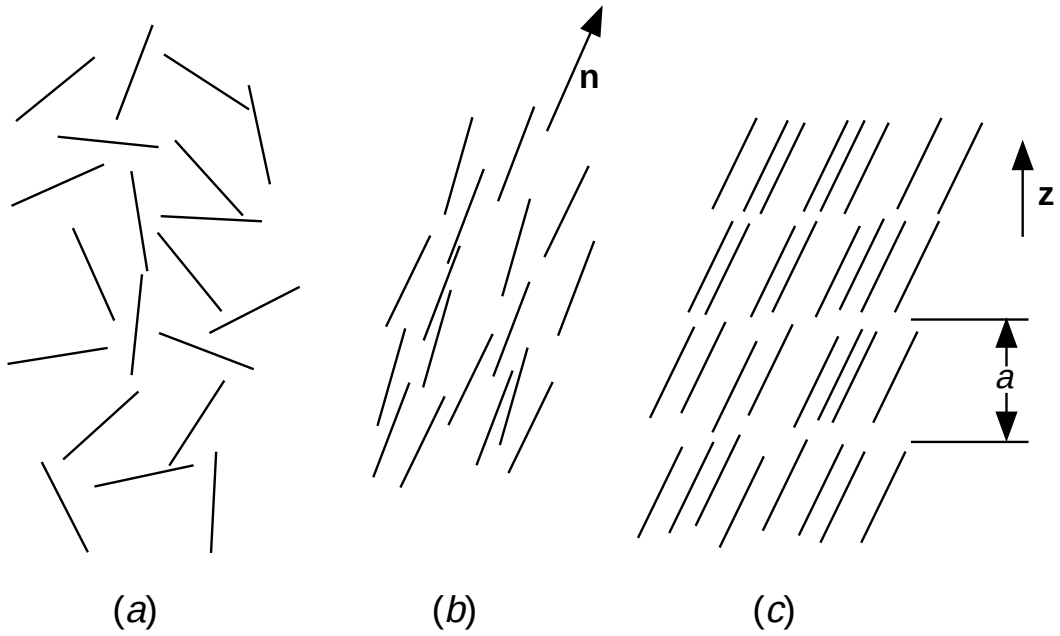

Figure 6.1. Three phases of matter with progressively decreasing symmetry: (*a*) isotropic, (*b*) nematic, (*c*) smectic

long, rod-shaped molecules shown in Fig. 6.1. The system can undergo a series of phase transitions as a function of temperature. At high temperature the substance is an isotropic liquid — there is no long-range translational or orientational order. As the temperature is lowered, the substance can undergo a phase transition to a nematic liquid crystal phase, with the molecules aligned along a single direction $\hat{\mathbf{n}}$, as shown in Fig. 6.1*b*. In the nematic phase there is still no long-range translational order — the translational symmetry of the system is preserved. However, the rotational symmetry is broken; while the system is still symmetric under any rotation around $\hat{\mathbf{n}}$, it is only symmetric under rotations by π around any axis perpendicular to $\hat{\mathbf{n}}$. At still lower temperatures the system may undergo a phase transition to a smectic phase. In a smectic phase, such as the one shown in Fig. 6.1*c*, the translational symmetry is broken in one direction — the system is only

symmetric under translations in the $\hat{\mathbf{z}}$-direction by a layer spacing, a. Smectic liquid crystals can be thought of as a weakly coupled stack of two-dimensional layers. There are a number of smectic liquid crystal phases, each with a different positional, bond-orientational, and molecular tilt order within the layers. For example, the so called smectic-*C* phase shown in Fig. 6.1*c* has no long-range positional order within a layer, but it does have long-range tilt order: all of the molecules are tilted in the same direction, at least over some macroscopic distance.

Because of the coupling between the layers, bulk smectic liquid crystals are not true two-dimensional systems. However, freely-suspended liquid crystal films with thicknesses as small as two layers can be formed; these films have been used as model two-dimensional systems, as well as to study the transition from three-dimensional to two-dimensional behavior.[2-6] As compared to freely-suspended liquid crystal films, Langmuir monolayers have the advantage that their density can be varied.

Recently an amphiphilic substance was identified that exhibits a 2D smectic-*C* phase, characterized by quasi-long-range orientational order and short-range positional order.[7] The molecules in this phase are tilted from the surface normal; their projection onto the interface defines a 2D director field

$$\hat{\mathbf{n}}(\mathbf{r}) = (\sin\theta(\mathbf{r}), \cos\theta(\mathbf{r})) \tag{6.1}$$

where θ is the angle that the projection makes with an arbitrarily defined x-axis. Because of the liquid-like positional order, it requires very little energy to induce a gradual change in $\hat{\mathbf{n}}(\mathbf{r})$. Therefore, long wavelength oscillations in the orientation require much less than the k_BT of thermal energy available at room temperature.

The consequence of these long wavelength oscillations being excited is that there are strong orientational fluctuations in $\hat{\mathbf{n}}(\mathbf{r})$.[3]

6.2 Theory

6.2.1 Two-dimensional nematic theory

The orientational fluctuations in a 2D nematic phase were studied theoretically by de Gennes[8] and by Van Winkle and Clark.[3] In particular, Van Winkle and Clark obtained an expression for the mean-square difference $\sigma(\mathbf{r}, t)$ in orientation angle θ, where

$$\sigma(\mathbf{r}, t) = \langle |\theta(\mathbf{r}, t) - \theta(0, 0)|^2 \rangle \tag{6.2}$$

In the absence of disclinations, the change in the free energy of a 2D nematic due to nonuniformities in $\hat{\mathbf{n}}(\mathbf{r})$ is given by[3]

$$F - F_0 = \int \{ \frac{1}{2} K_B [\hat{\mathbf{z}} \cdot (\nabla \times \hat{\mathbf{n}})]^2 + \frac{1}{2} K_s (\nabla \cdot \hat{\mathbf{n}})^2 \} \, d^2 r \tag{6.3}$$

where K_B and K_S are the bend and splay elastic constants, respectively, and $\hat{\mathbf{z}}$ is the direction normal to the interface. If one assumes $K = K_B = K_S$, Eq. 6.3 reduces to

$$F - F_0 = \frac{K}{2} \int \left[\left(\frac{\partial \theta}{\partial x} \right)^2 + \left(\frac{\partial \theta}{\partial y} \right)^2 \right] d^2 r \tag{6.4}$$

The director field can be written in terms of Fourier modes,

$$\theta(\mathbf{r}, t) = \sum_{\mathbf{q}} \theta_{\mathbf{q}}(t) \, e^{i(\mathbf{q} \cdot \mathbf{r})} . \tag{6.5}$$

Because $\varphi(\mathbf{r},t)$ is real, the Fourier modes must obey the condition

$$\theta_{\mathbf{q}}(t) = \theta_{-\mathbf{q}}^{*}(t) \tag{6.6}$$

In terms of these modes, the thermal average of the free energy is

$$\langle F - F_0 \rangle = \langle \frac{K}{2} \int \left[\left(\sum_{\mathbf{q}} i q_x \theta_{\mathbf{q}} e^{i(\mathbf{q}\cdot\mathbf{r})} \right)^2 + \left(\sum_{\mathbf{q}} i q_y \theta_{\mathbf{q}} e^{i(\mathbf{q}\cdot\mathbf{r})} \right)^2 \right] d^2 r \rangle \tag{6.7}$$

Because $\int (e^{i(\mathbf{q}\cdot\mathbf{r})} e^{i(\mathbf{q}'\cdot\mathbf{r})})\, d^2 r = \delta(\mathbf{q} + \mathbf{q}')$, Eq. 6.7 reduces to

$$\langle F - F_0 \rangle = \frac{K}{2} \sum_{\mathbf{q}} q^2 \langle |\theta_{\mathbf{q}}|^2 \rangle \tag{6.8}$$

From the equipartition theorem and Eq. 6.8 it then follows that

$$\langle |\theta_{\mathbf{q}}|^2 \rangle = k_B T / K q^2 \tag{6.9}$$

The temporal autocorrelation function of the Fourier modes is given by[8]

$$\langle \theta_{\mathbf{q}}(0)\, \theta_{\mathbf{q}'}(t) \rangle = \langle |\theta_{\mathbf{q}}|^2 \rangle \exp\left(-\frac{K q^2}{\nu} \right) \delta(\mathbf{q} + \mathbf{q}') \tag{6.10}$$

where ν is the orientational viscosity of the monolayer, and the delta function is due to the fact that the modes are uncorrelated. We now note that $\sigma(\mathbf{r}, t)$ is related to the standard correlation function for φ:

$$\sigma(\mathbf{r}, t) = \langle |\theta(\mathbf{r}, t) - \theta(0, 0)|^2 \rangle = 2 \langle (\theta(0, 0))^2 - \theta(0, 0)\, \theta(\mathbf{r}, t) \rangle \tag{6.11}$$

In terms of the Fourier modes Eq. 6.11 this becomes

$$\sigma(\mathbf{r}, t) = 2 \sum_{\mathbf{q}, \mathbf{q}'} [\langle \theta_{\mathbf{q}}(0)\, \theta_{\mathbf{q}'}(0) \rangle + \langle \theta_{\mathbf{q}}(0)\, \theta_{\mathbf{q}'}(t) \rangle e^{i(\mathbf{q}'\cdot\mathbf{r})}] \tag{6.12}$$

Using Eq. 6.9 and Eq. 6.10, and switching from a sum over **q** to an integration, we find the mean-square orientation difference

$$\sigma(\mathbf{r}, t) = \frac{k_B T}{2\pi^2 K}\int \frac{1 - e^{i(\mathbf{q}\cdot\mathbf{r})}\exp\left(-\frac{Kq^2}{\nu}\right)}{q^2} d^2q \qquad (6.13)$$

The experiments described in this chapter involve measurement of the mean-square orientation difference as a function of time in one region. Because the orientation can never be measured at a single point, but rather is averaged over a region of area α, where α is on the order of μm^2, we weight the integral in Eq. 6.13 with a factor of $\exp(-\alpha q^2)$. The predicted form of the mean-square orientation difference in a single region of area α as a function of time is therefore

$$f(t) = \frac{k_B T}{\pi K}\int \frac{1 - \exp\left(-\frac{Kq^2 t}{\nu}\right)}{q}\exp(-\alpha q^2)\, dq = \frac{k_B T}{2\pi K}\ln\left(1 + \frac{Kt}{\nu\alpha}\right) \qquad (6.14)$$

The function $f(t)$ has two limiting forms; for $(Kt)/(\nu\alpha) \gg 1$ $f(t)$ diverges logarithmically with time, $f(t) \approx \frac{k_B T}{2\pi K}\left(\ln t + \ln\frac{K}{\nu\alpha}\right)$. For $(Kt)/(\nu\alpha) \ll 1$, $f(t)$ is linear with time, $f(t) \approx \frac{k_B T}{2\pi\nu\alpha} t$. Since T and α are both known, measuring the slope of $f(t)$ in the linear regime yields a measure of the orientational viscosity ν. These limiting cases, with their simple mathematical form, are not sufficient to experimentally test the theoretical prediction. A more sensitive test of the theory is to see if the experimental data agrees with the predicted functional form in the crossover regime from linear to logarithmic behavior.

6.2.2 Caveats

The theory described above describes the behavior of orientational fluctuations in a two-dimensional nematic liquid crystal. Nematic liquid crystals have inversion symmetry, which a smectic-*C* monolayer lacks.[1] Therefore, the free energy for a smectic-*C* liquid crystal can have terms that a nematic lacks; specifically, it can have terms that are not invariant under the inversion operation. This has two main consequences. One consequence involves disclinations in the film; a disclination of strength *s* is a defect around which the director $\hat{\mathbf{n}}$ rotates by $s\pi$. Figure 6.2 shows an $s = 1/2$ and an $s = 1$ disclination. While a two-dimensional nematic liquid crystal, for which the directions $\hat{\mathbf{n}}$ and $-\hat{\mathbf{n}}$ are equivalent, can have either integral or half-integral disclinations, in a two-dimensional smectic-*C* liquid crystal only integral strength disclinations are allowed.

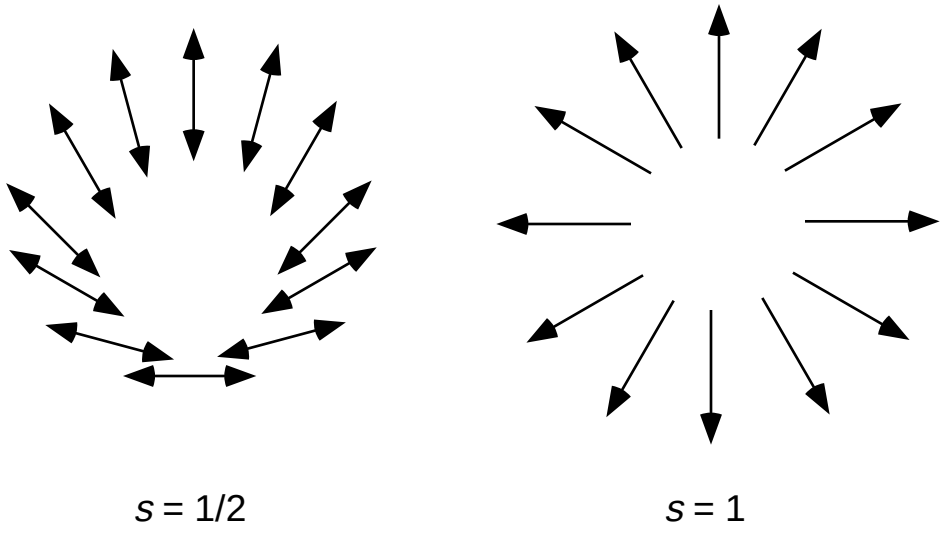

Figure 6.2. Top view of an $s = 1/2$ disclination in a two-dimensional nematic and an $s = 1$ disclination in a two-dimensional smectic-*C*. The half-integral disclination is not allowed in a smectic-*C*, which lacks inversion symmetry.

A second consequence of the lack of inversion symmetry was pointed out by Selinger, *et al.*[9] who show that the lack of inversion symmetry in a two-dimensional smectic-*C* monolayer can lead to the formation of a stripe phase in which the orientation angle θ changes linearly with position. The monolayer described in this chapter forms a stripe phase;[7] however, if measured away from any disclinations or stripe boundaries, we expect that the mean-square difference in orientation for a two-dimensional smectic-*C* liquid crystal displays the functional form of Eq. 6.14.

6.3 Experiment

6.3.1 Sample characterization

The experiments described below were performed on Langmuir monolayers of 4-octyl-4'-(3-carboxytrimethyloxy) azobenzene (8AZ3), an azobenzene derivative that has been modified to make it amphiphilic. A 0.002-molar solution of 8AZ3 (>99% purity) in chloroform is spread on a subphase of deionized water (ρ > 18 MΩ/cm) from a Millipore Milli-Q system. We found that the behavior of the monolayer is sensitive to the chemistry of the water. Specifically, the results of the experiment were not reproducible within the first couple of days after water had been obtained from the Milli-Q system. Reproducible results were obtained using water that was allowed to equilibrate with atmospheric CO_2. The experiments were performed in the light scattering trough described in Chapter 2.

Figure 6.3 shows isotherms for 8AZ3 monolayers taken with continuous compression at a rate of 4.1×10^{-4} nm^2/s. At low molecular density N (N < 3.0 nm^{-2})

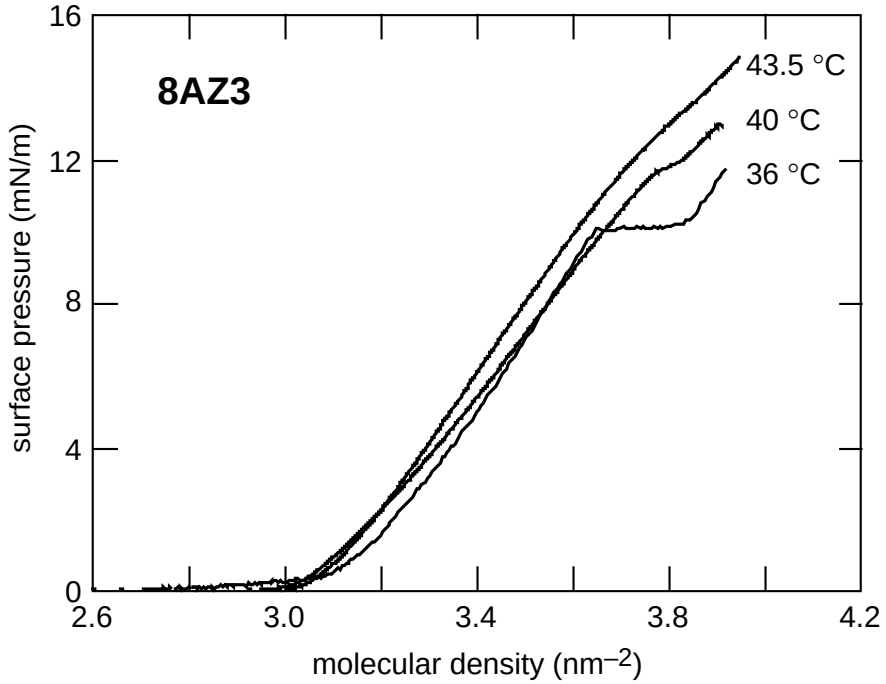

Figure 6.3. Three isotherms of 8AZ3. At low surface pressures the monolayer is in the smectic-C phase. At 36 °C the monolayer undergoes a first order transition to a more condensed phase at a surface pressure of 10.4 mN/m. At higher temperatures the pressure of the phase transition rises, and the transition becomes continuous.

the monolayer is in a coexistence region of a 2D gas phase and a 2D smectic-*C* phase. The pressure in this region is immeasurably small. The pressure begins to rise at $N \approx 3.0$ nm^{-2}, when the monolayer is in the pure smectic-*C* phase. At 36 °C, the monolayer undergoes a first-order phase transition from the smectic-*C* phase to a more condensed phase at a surface pressure $\pi = 10.4$ mN/m. At higher temperature this phase transition becomes continuous and the pressure at which it occurs increases.

6.3.2 Experimental setup

We studied the orientational fluctuations in 8AZ3 using depolarized Brewster angle microscopy.[7] The purpose of the experiment is to measure $f(t)$, *i.e.*, to

measure the orientation of the molecules as a function of time in a region of area α. The experimental setup is illustrated in Fig. 6.4. The air-water interface is illuminated with *p*-polarized light from a 10 mW HeNe laser. The light is incident at the Brewster angle of water to eliminate the background signal from the water subphase. The analyzer transmits only the *s*-polarized light reflected from the monolayer. Two lenses image this light onto a CCD camera as follows. Lens 2 focuses the image of a pinhole in the center of the mirror onto the CCD camera. Lens 1 is then adjusted so that the image of the monolayer on the CCD camera is in focus. This insures that the pinhole lies on the image plane of lens 1.

If the monolayer were isotropic (*i.e.*, if there were no quasi-long-range orientational order), then the reflected light would be *p*-polarized. However, since

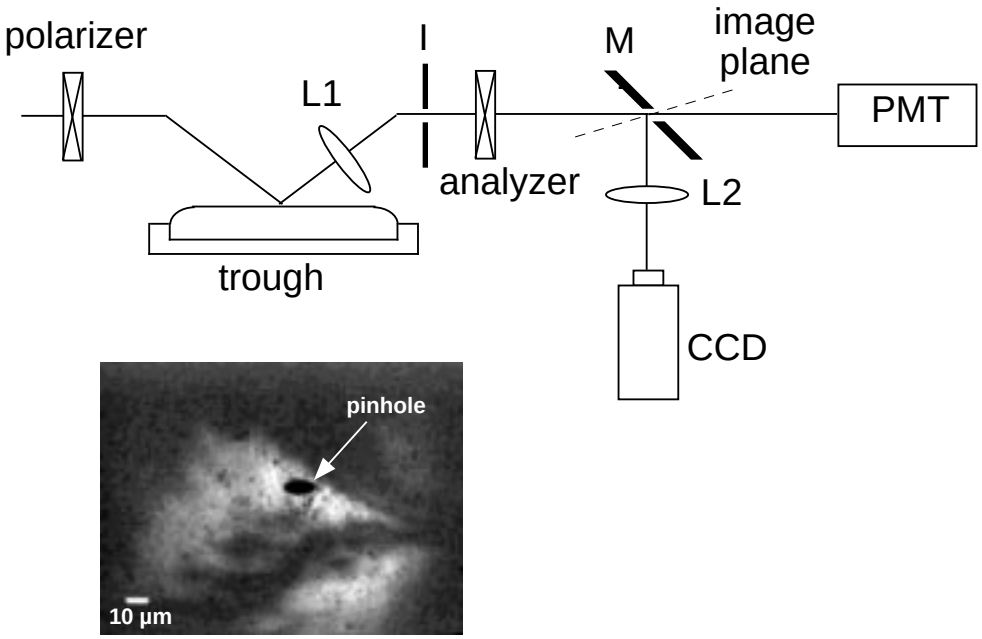

Figure 6.4. Schematic diagram of the experimental setup. Depolarized light reflected from the monolayer is imaged by lenses (L) onto a CCD camera. The light from one region of the monolayer is transmitted through a pinhole in mirror (M) and measured with a photomultiplier tube (PMT). The iris (I) is used to vary the resolution of the microscope.

the smectic-*C* phase has quasi-long-range orientational order and the molecules are optically anisotropic, the polarization and intensity of the reflected light depend on the local orientation of the molecules, as discussed in Chapter 3. Tabe and Yokoyama[10] have shown that the intensity of the *s*-polarized component of the reflected light is given by

$$I(\theta) \propto [\sin(\theta)\,(\cos(\theta) - c)]^2, \tag{6.15}$$

where c is a constant that depends on the dielectric constant of the sample and the angle that the molecules make with the surface normal. Assuming that c is uniform for the entire film, which is plausible for Langmuir monolayers, the intensity at the detector is determined by the orientational angle θ.

The pinhole in the mirror transmits the light reflected from a small region of the interface. The size of this region, which determines the parameter α, the area over which the azimuthal angle is averaged, is determined by either the size of the pinhole ($\approx 30\ \mu m^2$) or the square of the resolution of the microscope, whichever is larger. Because the resolution of the microscope degrades rapidly outside of the depth of focus, it is important for the image of the monolayer to be focused on the pinhole. The imaging lens for this microscope has a theoretical resolution of approximately 1 μm, which would yield a very short depth of focus. We therefore use an iris between the lens and the mirror to reduce the resolution of the microscope, and therefore increase its depth of focus. Since the microscope's resolution is proportional to the diameter of the iris, the iris allows us to vary the parameter α.

The light transmitted through the pinhole is detected with a photomultiplier tube (PMT). For each photon that is detected, the PMT gives off approximately 10^6 photoelectrons in a pulse of several nanoseconds. A resistor and capacitor connected in parallel to ground are used to spread each pulse to 100 μs. Because the detected signal level in these experiments is approximately 10^6 photons per second, the pulses from many detected photons overlap with each other; the result is a voltage which is proportional to the reflected intensity. The signal is amplified with a high input impedance amplifier (R_{in} = 100 MΩ) and detected with a digital oscilloscope.

The image of the monolayer on the CCD camera is monitored during the experiment; when the area imaged onto the pinhole is far from any disclinations or stripe boundaries, we record the intensity of the photomultiplier signal for 0.2 s at a 1-kHz sampling rate.

Figure 6.5 shows the relationship between reflected intensity, normalized to the maximum reflected intensity, and the azimuthal angle θ of the molecules in the monolayer. The curve is calculated from Eq. 6.15 with c = 0.5; this value is an estimate of c based on analysis of the stripe texture of the monolayer. Data is only collected when the normalized intensity is 0.5 ± 0.25, indicated by the gray region in Fig. 6.5. In this region the relation between intensity and azimuthal angle is approximately linear. The digitized data is converted from intensity to azimuthal angle, assuming that c = 0.5. For any given measured intensity, it cannot be determined if the azimuthal angle of the molecules corresponds to a point on slope

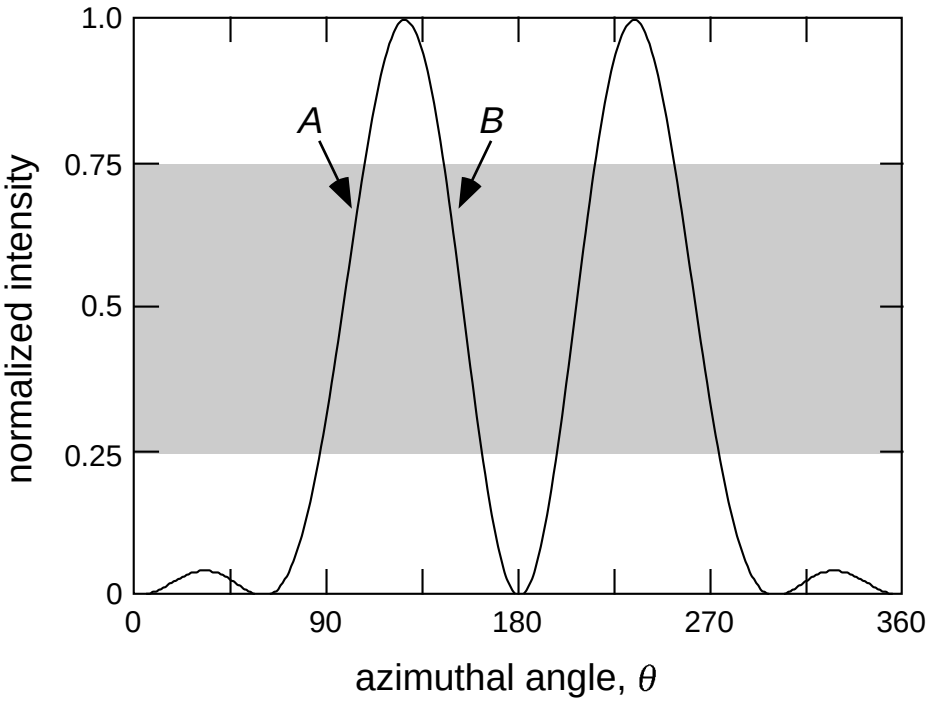

Figure 6.5. Dependence of reflected intensity on molecular orientation. Data is collected in the gray region, where the normalized intensity is approximately linear.

A or slope *B*. When converting the intensity to azimuthal angle, we use the values given by slope *A*.

An error is introduced into the measurement because slope *B* is not identical to slope *A*; calculations show this error to be approximately 10%. Another source of error is introduced by the assumption that $c = 0.5$; c is unknown, and may change as a function of temperature and molecular density. However, changes of c in the range of 0.5 to 1.0 result in less than 10% error in the calculations of the orientational elasticity and viscosity. Finally, an error would be introduced if the intensity changed from slope *A* to slope *B* during a single 0.2 s measurement. This would require the intensity to start on one slope, go through the maximum or the

minimum intensity, and end on the other slope. This effect is never seen in our data.

After the data have been transformed from intensity to angle, they are processed to calculate $(\theta(0) - \theta(t))^2$ for $0 < t < 0.1$ s. The $(\theta(0) - \theta(t))^2$ data from 100 samples is averaged together to form one data set of $f(t) = \langle |\theta(\mathbf{r}, t) - \theta(0, 0)|^2 \rangle$ (the term "data set" in this chapter refers to one of these sets of 100 samples averaged to calculate $f(t)$).

6.3.3 Results

Figure 6.6 shows measurements of $f(t)$ for 8AZ3 at $T = 40$ °C for various surface pressures π. Each curve represents the average of about one thousand 0.2-s samplings. We fit to the data a function of the form

$$f(t) = A \ln(1 + Bt) + C \tag{6.16}$$

where $A = \frac{k_B T}{2\pi K}$, and $B = \frac{K}{\nu\alpha}$ (see Eq. 6.14); the offset C accounts for detector noise. Because T and α are both known, fit parameters A and B allow us to determine K and ν. For the $\pi = 7.1$ mN/m data, $\frac{Kt}{\nu\alpha} \ll 1$ for the whole range of t measured; therefore, the $f(t)$ curve is approximately linear. For the 0 and 1.4 mN/m data, on the other hand, $f(t)$ is in the crossover from $\frac{Kt}{\nu\alpha} \ll 1$ to $\frac{Kt}{\nu\alpha} \gg 1$. As the fits in Fig. 6.6 show, the data are in excellent agreement with the predicted functional form throughout the transition from linear to logarithmic behavior.

As a further test of the theory, we measured $f(t)$ at various microscope resolutions while keeping temperature and surface pressure constant. The microscope resolution was varied by changing the diameter of the iris between the

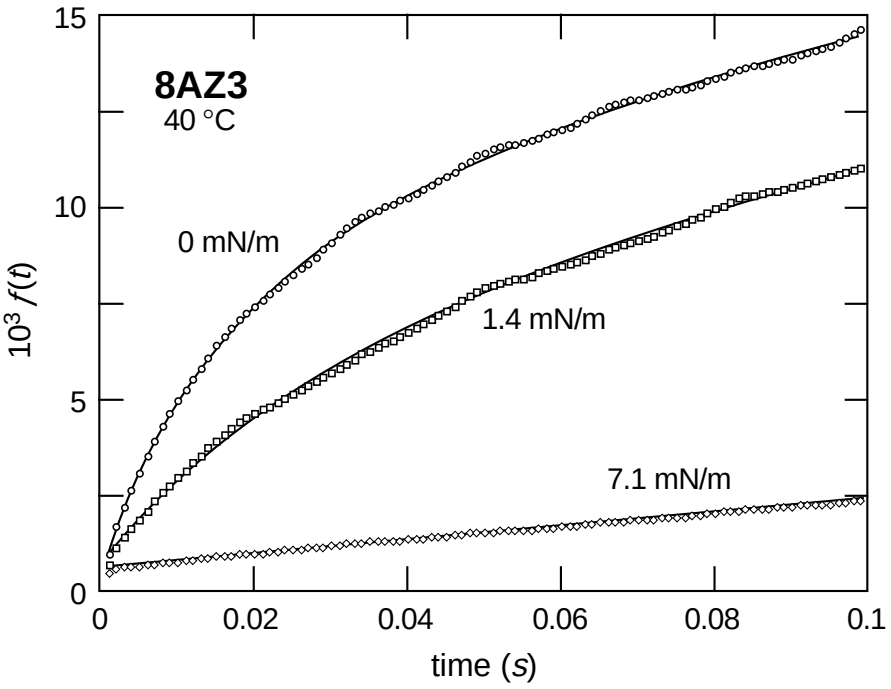

Figure 6.6. Mean square difference in molecular orientation, $f(t)$, for several surface pressures at T = 40 °C. The solid lines are fits to the predicted form $f(t) = A \ln(1 + Bt) + C$.

imaging lens and the mirror with a pinhole (see Fig. 6.4); making the iris smaller effectively reduces the numerical aperture of the imaging lens, and thereby decreases its resolution (*i.e.*, it increases the size of the smallest feature that can be resolved). The area α is equal to the square of the smallest feature the microscope can resolve. As α is changed at constant temperature and surface pressure, A should remain constant, while B, and therefore the product AB, should vary as α^{-1}.

Figure 6.7 shows the measured dependence of A and AB on α at 40 °C and zero surface pressure. For each value of α we collected n data sets ($n \approx 10$) and fit each data set to the function given by Eq. 6.16. The points in Fig. 6.7 correspond to the average of the fitting parameters from the n data sets. The error bars represent the standard deviations of the values from the n data sets, divided by $\sqrt{n}$. We have

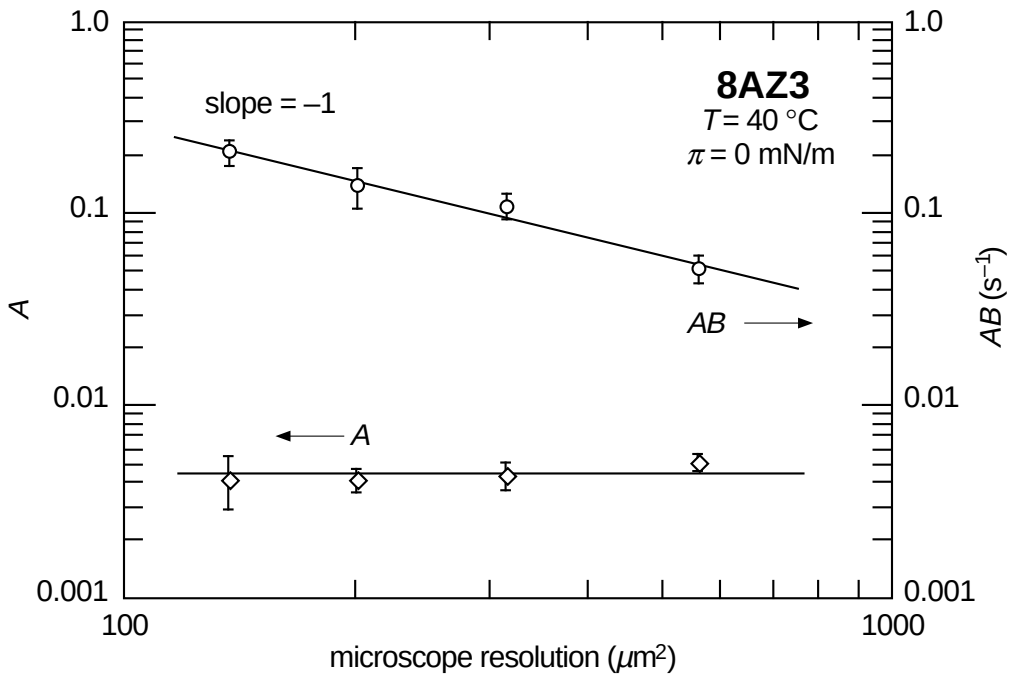

Figure 6.7. Fitting parameters *A* and *AB* as a function of the area over which the detector averages. Theoretical predictions require that *A* be independent of α, and *AB* be inversely proportional to α.

plotted *AB* instead of *B* because the error bars for *AB*, which is the slope for small *t*, are significantly smaller than the error bars for *B*. The graph shows that, within experimental error, *A* is independent of α, and that *AB* is inversely proportional to α. We conclude that the data strongly supports the applicability of two-dimensional nematic theory to a smectic-*C* Langmuir monolayer.

From the fitting parameters *A* and *B* we can obtain values for the orientational elasticity, $K = \frac{k_B T}{2\pi A}$, and orientational viscosity, $\nu = \frac{k_B T}{2\pi\alpha AB}$, see Eq. 6.16. When the measured $f(t)$ displays a crossover from linear to logarithmic behavior, as in the zero surface pressure data in Fig. 6.6, the fitting procedure accurately measures both *A* and *B*, and we can therefore determine both *K* and ν. However, when $f(t)$ is approximately linear, as in the 7.1 mN/m data in Fig. 6.6, the

fitting procedure only accurately measures the slope of the data, *i.e.*, the product *AB*, and so we are not able to determine *A* and *B* independently. In those cases we can accurately determine the orientational viscosity ν, but not the orientational elasticity *K*.

Figure 6.8 shows ν for a range of temperatures and surface pressures (and therefore density). Comparison with the isotherms in Fig. 6.3 shows that the range of surface pressures studied corresponds to approximately a 20% change in the density. As in Fig. 6.7, the error bars correspond to the standard deviation of the orientational viscosity measured in *n* data sets divided by $\sqrt{n}$. The orientational viscosity ν is strongly dependent on both surface pressure and temperature; it increases by more than an order of magnitude as the monolayer approaches the

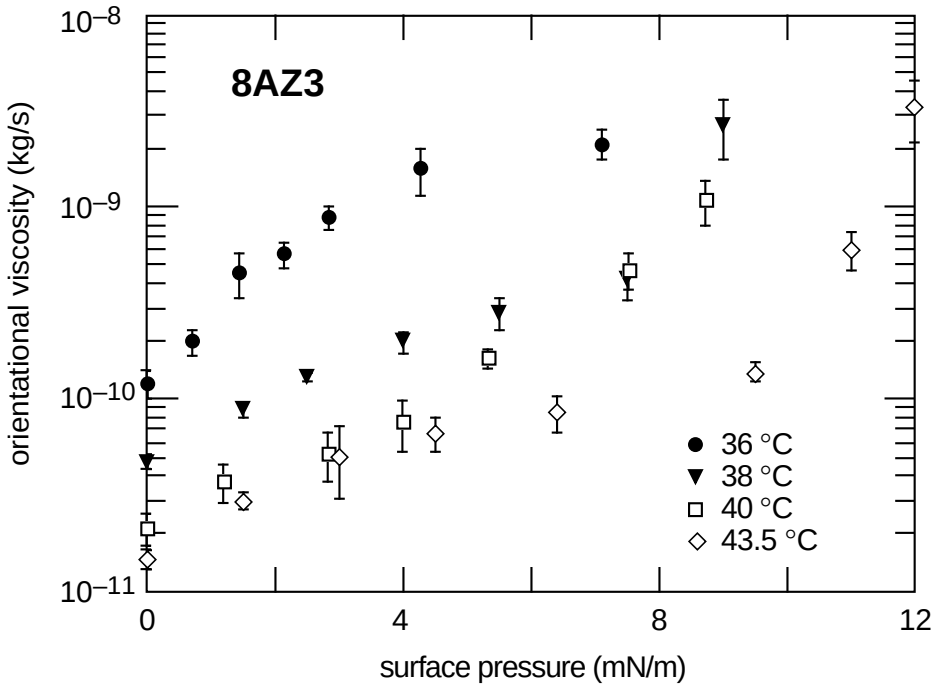

Figure 6.8. Measured orientational viscosity, ν, as a function of surface pressure. The range of surface pressures in this plot represent approximately a 20 percent change in density (see Fig. 6.3).

transition from smectic-*C* to a more condensed phase, and decreases by an order of magnitude with an increase in temperature of 7.5 °C. Within experimental error, on the other hand, the orientational elasticity *K* depends only weakly on temperature and surface pressure. There is no clear trend of *K* with increasing density; all of our measurements of *K* yield values in the range $K/k_BT = 385 \pm 245$.

We can compare our measured orientational elasticities and viscosities with previous measurements on freely-suspended liquid crystal films. The smallest viscosities we obtain ($\approx 10^{-11}$ kg/sec) are approximately an order of magnitude larger than the viscosities measured in freely-suspended smectic-*C* films,[2, 5] while the largest viscosities ($\approx 10^{-9}$ kg/sec) are consistent with viscosities measured in a hexatic-*I* freely-suspended liquid crystal film.[2] The orientational elasticities reported here are intermediate between the values measured in smectic-*C* and hexatic-*I* freely suspended liquid crystal films.[2] Due to the coupling of the monolayer to the water subphase, it is not surprising that the orientational viscosity is larger in a smectic-*C* monolayer than in a freely-suspended smectic-*C* liquid crystal. In any case, since it has been shown theoretically[11] and experimentally[12] that the smectic-*C* and hexatic-*I* phases are not thermodynamically distinct, our measurements are consistent with those on freely-suspended liquid crystal films. Additional theoretical work is necessary to explain the dependence of *v* and *K* on density.

6.4 Conclusion

In summary, we studied orientational fluctuations in a smectic-*C* Langmuir monolayer using depolarized Brewster angle microscopy. Our results are in excellent agreement with theoretical predictions of the orientational correlations in

a two-dimensional nematic liquid crystal. In addition, we find that the orientational viscosity is strongly dependent on temperature and density, changing by more than an order of magnitude with a 2.5 percent change in temperature or a 20 percent change in density. The orientational elasticity, on the other hand, depends only weakly on temperature and density. These are the first measurements of orientational elasticity and viscosity in a two-dimensional system with variable density.

References

[1] P. M. Chaikin and T. C. Lubensky, *Principles of Condensed Matter Physics* (Cambridge University Press, Cambridge, 1995).

[2] S. B. Dierker and R. Pindak, Phys. Rev. Lett. **59**, 1002 (1987).

[3] D. H. Van Winkle and N. A. Clark, Phys. Rev. A **38**, 1573 (1988).

[4] C. Y. Young, R. Pindak, N. A. Clark, *et al.*, Phys. Rev. Lett. **40**, 773 (1978).

[5] C. Rosenblatt, R. Pindak, N. A. Clark, *et al.*, Phys. Rev. Lett. **42**, 1220 (1979).

[6] S. M. Amador and P. S. Pershan, Phys. Rev. A **41**, 4326 (1990).

[7] Y. Tabe and H. Yokoyama, Journal of the Physical Society of Japan **63**, 2472 (1994).

[8] P. G. de Gennes, Symp. Farad. Soc. **5** (1971).

[9] J. V. Selinger, Z. Wang, R. F. Bruinsma, *et al.*, Phys. Rev. Lett. **70**, 1139 (1993).

[10] Y. Tabe and H. Yokoyama, Langmuir **11**, 699 (1995).

[11] D. R. Nelson and B. I. Halperin, Phys. Rev. B **21**, 5312 (1980).

[12] J. D. Brock, A. Aharony, R. J. Birgeneau, *et al.*, Phys. Rev. Lett. **57**, 98 (1986).